IMAGE GUIDED ROBOTS FOR UROLOGY

by

Chunwoo Kim

Urology Robotics Laboratory

A dissertation submitted to Johns Hopkins University in conformity with the requirements for the degree of Doctor of Philosophy

Baltimore, Maryland

March, 2014

Abstract

This dissertation addresses the development of medical image-guided robots and their applications in urology. Image-guided robots integrate medical image information with robotic precision to assist the planning and execution of the image-guided interventions. Robots guided by two different image modalities, ultrasound and MR image, were developed. Ultrasound image-guided robots manipulate an ultrasound probe and a needle-guide that are calibrated with respect to the robot for image-guided targeting. A method for calibration was developed and verified through the image-guided targeting experiments. Robotic manipulation of the calibrated probe allows acquisition of image slices at precise location, which can be combined to generate a 3D ultrasound image. Software for 3D ultrasound image acquisition, processing, and segmentation was developed as a part of the image-guided robot system.

The feasibility of several image-guided intervention procedures using the ultrasound image-guided robot system was tested. The robot was used in a clinical trial of intraoperative transrectal ultrasound (TRUS) guided prostatectomy. The accuracy of TRUS-guided prostate biopsy using the robot was evaluated in a comparative study versus the classic human operation of the probe. Robot controlled palpation and image processing methods were developed for ultrasound elastography imaging of the prostate. An ultrasound to CT image-fusion method using the robot as a common reference was developed for percutaneous access of the kidney.

MRI-guided robots were developed for transrectal and transperineal prostate biopsy. Extensive in-vitro tests were performed to ensure MRI compatibility and image-guided accuracy of the robots. The transrectal robot was evaluated in an animal study and the transperineal robot is undergoing a clinical trial. The collection of methods and algorithms presented in this dissertation can contribute to the development of image-guided robots that may provide less invasive and more precise interventions in urology, interventional radiology, and other fields.

Advisor: Professor Dan Stoianovici

Readers: Professor Russel. H. Taylor and Professor Gregory. S. Chirikjian

Acknowledgments

My 6 years of Ph.D. study at Johns Hopkins Urology Robotics Lab was a wonderful experience that trained me as an independent researcher. This would not have been possible without so many awesome people I have met during past 6 years.

First of all, I would like thank my advisor Professor Dan Stoianovici for his advising throughout my study. He provided me with the academic freedom to study as well as timely and intuitive advices. He was the best advisor that any graduate student can expect, both academically and personally as well. I would also like to thank Dr. Misop Han at Hopkins and Dr. Govindarajan Srimathveeravalli at Memorial Sloan Kettering Cancer Center for their support with the clinical studies.

Second, I would also like to thank my dissertation readers, Professor Gregory Chirikjian and Professor Russel Taylor for their thorough review of my dissertation and constructive comments. It was my honor to have them as my dissertation reader.

Life and work at the lab would have been very dull without the wonderful colleagues. Special thanks goes to Doru Petrisor who was like a 'mom' of the lab. Thanks to my fellow students Bogdan Vigaru, Felix Schaefer, Doohyun Lee, Yihe Zuo, Doyoung Chang, Changhan Jun and Ryan Decker, and also to clinical fellows of the lab, Drs. Shadi Badaan, Jeremy Huang, Hyungjoo Kim, Haixin Chen and Chong Xue.

Thanks to my families in Korea and Jane Yoo for their love and support, and last but not least, to the God who led me through all these days.

This work was supported by

- Fulbright Scholarship, Institute of International Education
- Department of Defense Prostate Cancer Training Award grant No. W81XWH-11-1-0662

Table of Contents

List of Tables

List of Figures

1 Introduction

This dissertation addresses the development of medical image-guided robots and their applications in urology. Image-guided robots are part of the larger ‘Computer Integrated Surgery’ (CIS) system that is designed to assist a surgeon in carrying out a surgical procedure (Taylor and Stoianovici, 2003). As a part of the CIS system, medical robots not only augment physician’s manipulation capabilities but also establish a digital platform for integrating medical imaging data (Taylor and Stoianovici, 2003). Image-guided robots can combine the rich information from the medical images with the computer controlled precision of the robot, enabling more precise planning and execution of the interventional procedure.

Urology was one of the first specialties in the medicine that saw the widespread use of medical robots. Robot assisted laparoscopic radical prostatectomy (RALP) using the daVinci surgical robot system (Intuitive Surgical Inc. Sunnyvale, CA) was first performed in 2001(Pasticier et al., 2001), and it is estimated that by 2013, approximately 80% of all surgeries for prostate cancer are RALP (Skarecky, 2013). Although the daVinci system is not an image-guided robot but surgical assistant system, the wide acceptance of the daVinci system in the urology has also opened the scene for the introduction of image-guided robots.

In urology, like other medical specialties, medical images are used not only for diagnosis but also for planning and guiding the interventional procedures. There are many interventional procedures in urology with potential for improvement by using robots, for example prostate biopsy.

Prostate cancer (PCa) has the highest number of diagnosed yearly cases (238,590) in men excluding the skin cancer, and second in the number of cancer deaths (29,720) (Siegel et al., 2013). One of the biggest challenges in prostate cancer treatment is diagnosis. The most common way of diagnosing PCa is the transrectal ultrasound (TRUS)-guided prostate biopsy. But standard grayscale ultrasound provides minimal PCa specific information, being unreliable in differentiating PCa from normal gland tissues. The biopsy procedures are cancer “blind”, aiming to sample the gland systematically in search of possible tumors. Since PCa is a heterogeneous multifocal disease, untargeted biopsies often lead to the detection of small, clinically insignificant tumors and/or miss significant cancers (Kelloff et al., 2009). This leads to repeated biopsy and overtreatment. A study has shown that it is necessary to treat 48 men to prevent one death from

PCa (Barry, 2009). Therefore, image-guided robots that integrate the novel imaging modalities with the robotic precision can improve the diagnosis of prostate cancer by targeted biopsy and/or more accurate systematic sampling of the prostate.

This document presents the development of several image-guided robotic systems guided by ultrasound and Magnetic Resonance Imaging (MRI) images and their applications in urology. The system development process including the design of the robot hardware, development of control and image guidance software, and verification of the system accuracy are described. The robots are applied to several image-guided interventions in urology including radical prostatectomy, prostate and kidney biopsy and focal therapies. Tests include in-vitro, animal, and clinical trials.

1.1 Literature Review

A massive amount of research has been dedicated to the development of medical robots, and several have already had a significant clinical impact. Selected literatures on medical robots related to the topics of ultrasound and MRI guidance with applications in urology are reviewed herein.

1.1.1 Ultrasound Image-Guided Robots

In addition to improved accuracy and precision that is expected from the introduction of a robot, integrating the robots to Ultrasound Sonography (ultrasound) presents additional advantages. By manipulating the ultrasound probe with a robot, the position and orientation of the 2D ultrasound images can be tracked and used for 3D image reconstruction. Several robotic ultrasound systems integrating the ultrasound imaging with the robots have been developed and a comprehensive review on the systems developed over last two decades can be found in (Priester et al., 2013, Kaye et al., 2014).

One of the earliest robotic ultrasound systems were developed for diagnosis imaging (Degoulange et al., 1998, Abolmaesumi et al., 2002). In (Degoulange et al., 1998), an industrial robot (Mitsubishi PA-10) was used to manipulate an ultrasound probe to scan along the arteries. An external force control method was used to maintain a constant force between the skin and the probe and also augment safety. In (Abolmaesumi et al., 2002), a 6 degree of freedom (DoF) robot was used to manipulate an ultrasound probe.

It had numerous advanced features, including a novel algorithm for segmentation of vessel boundary and image-based servoing.

In addition to diagnostic imaging, many robotic ultrasound systems were developed for guiding needles during the intervention process. In urology, guiding needle insertion for prostate biopsy (Ho et al., 2009) and brachytherapy (Yu et al., 2007, Fichtinger et al., 2008, Bassan et al., 2009, Bax et al., 2011, Hungr et al., 2012) has been the main application of robotic ultrasound systems.

In (Ho et al., 2009), a system is developed for transperineal access to the prostate. The system consists of robotic positioning system and an ultrasound probe holder. The robotic positioning system controls the position and the insertion depth of the needle, such that the entire prostate is accessible through two pivot points which the authors refer as 'dual cone'. The ultrasound probe holder can translate the probe to collect transverse images of the prostate at fixed intervals and create the 3D images of the prostate. The probe is covered by a plastic sheath which supports the rectal wall to maintain a constant deformation as the probe is translated. The system was tested in mockup experiments demonstrating sub mm accuracy.

In (Yu et al., 2007), the authors report a robotic system for prostate brachytherapy. The probe driver part is capable of rotating and translating the TRUS probe to acquire 3D images. The needle driver part orients the needle by adjusting XY translation and pitch and is equipped with force sensors that allow force control insertion of the needle while rotating the needle. The system was tested in mockup.

In (Fichtinger et al., 2008), robotically assisted prostate brachytherapy is developed and was tested in mockup and a Phase-I clinical trial. The system consists of a commercial TRUS probe positioner for rotating and translating the probe (a brachytherapy “stepper”) and a small parallel needle guidance robot that consists of two 2D Cartesian stages used to orient the direction of the needle. The system was integrated with an FDA-approved commercial treatment planning system.

In (Bassan et al., 2009), 5-DoF cable driven manipulator for brachytherapy is reported. It has 2-DoF for a parallelogram-based Remote Center of Motion (RCM) module to orient the needle and 3-DoF for needle translation, rotation and seed insertion. A side-fire TRUS probe is rotated to generate the 3D ultrasound image. Reported accuracy was 1.45 mm in mockup tests.

In (Bax et al., 2011), authors report a mechanically assisted system where insertion is performed manually. Their needle positioning device consists of a 4-DoF using two spherical link, 2-DoF to adjust the position of the RCM point and 2-DoF to pivot the needle about the RCM. The TRUS probe is rotated to acquire the 3D image of the prostate.

In (Hungr et al., 2012), a system consisting of a 3D end-fire ultrasound probe and a needle insertion robot was reported. The system was designed with emphasis of reducing and tracking prostate deformations during the brachytherapy procedure. The probe is fixed on position throughout the procedure, eliminating prostate deformations that are normally induced by probe motion. 3D ultrasound images are acquired before and after each needle insertion. By using a novel image-to-image registration algorithm developed by the authors in (Baumann et al., 2012), the system can track deformation of the prostate caused by needle insertion and adjust the plan. The needle insertion robot consists of a 3-DoF module for XYZ translation and a 2-DoF module for needle rotation and insertion. The system was tested on a special mockup designed to simulate prostate deformations. The authors report 3.86 mm accuracy at the prostate base by compensating for 6.94 mm deformations.

Recently, the possibility of using robotic ultrasound systems for intraoperative guidance of prostatectomy is being explored by several research groups. A TRUS robot from our lab, which is presented in this dissertation, was the first robotic ultrasound system to be applied for intraoperative guidance during robot assisted radical prostatectomy (RALP) using daVinci robot (Han et al., 2011), proving the feasibility of intraoperative guidance. Subsequent applications have been reported by other groups. Commercial endoscope manipulator (ViKY System, EndoControl Medical, Grenoble, France) was used to manipulate the TRUS in (Hung et al., 2012). A method to register the daVinci to the ultrasound manipulator by localizing the tooltip of the daVinci in the TRUS image is reported in (Adebar et al., 2012, Mohareri et al., 2013). Once registered, the TRUS probe can automatically track the tool tip of the daVinci robot.

Finally, two non-robotic commercial systems, the Artemis (Bax et al., 2008, Cool et al., 2008) and the UroStation (Mozer et al., 2009) demonstrate novel applications integrating ultrasound and computer technology. The Artemis system (Eigen Inc., Grass Valley, CA) consist of a 4-DoF mechanically encoded arm described in (Bax et al., 2008) that supports the end-fire TRUS probe. The probe is rotated to acquire series of 2D ultrasound images and reconstructs the 3D image. Then the 3D image is segmented using a special semi-automatic algorithm described in (Wang et al., 2003). Biopsy is planned and executed based on the segmented image and each biopsy location is recorded. The UroStation (Koelis, La Tronche, France) is a software system augmenting freehand prostate biopsy with a 3D TRUS probe. At the beginning of the biopsy and after each needle insertion, urologists acquire 3D images of the prostate and the images are registered to the reference volume using the deformable registration algorithm described in (Baumann et al., 2012). This allows biopsy locations to be recorded for quality control purposes.

Both systems are designed to involve minimal modifications of the typical clinical workflow of prostate biopsy, yet providing the additional benefits of 3D ultrasound imaging. The systems have been applied clinically. Also, these systems suggest the future direction for the development of ultrasound image-guided robots for needle access to the prostate – deformation control.

While mechanical arms like the Artemis system allow targeted needle access, a robotic arm can additionally enable automated targeting and may provide better control of the prostate deformations as the probe is moved. While a system like the UroStation can possibly track deformations, this computation is not made in real-time. Moreover, the size and the resolution of the image volume that can be acquired with 3D probes are limited.

1.1.2 MRI-Guided Robots

Magnetic Resonance Imaging (MRI) has been widely used in medicine as it provides good soft tissue contrast and avoids ionizing radiation. But image-guided robots must be compatible with the image modality to be used. This may include criteria such as compactness, image “translucency”, the ability to operate with the imaging device, and mutual non-interference (Taylor and Stoianovici, 2003). The MRI scanner is probably the most challenging imaging device to ensure compatibility with. It is a unique environment due to the high magnetic field and very limited scanner bore size. This presents multiple engineering challenges in terms of material for the construction of the robot, actuation and sensing methods, and safety. Many MRI compatible robotic systems have been designed to overcome these challenges and comprehensive reviews of the developed systems are given in (Cleary et al., 2006, Gassert et al., 2008a, Elhawary et al., 2008, Macura and Stoianovici, 2008). Selected systems are reviewed herein.

One of the first MRI robot systems was (Chinzei et al., 2000). This ultrasonic motor actuated robot was operated in an open MRI scanner (“double donut”). To minimize image interference from the piezo motors, the robot was mounted above the scanner and extended a long arm to the scanner isocenter.

One of the first commercial MRI-guided robotic systems was INNOMOTION (Hempel et al., 2003, Melzer et al., 2008) from the German company Innomedic, originating from the Karlsruhe Institute of Technology. The system consists of a 5-DoF robot attached with a bridge-like structure over the MRI table, an orbit ring. The robot can be positioned around the ring. The robot itself has 5-DoF: 3 for positioning the insertion point and 2 for orienting the needle about the insertion point. The system is actuated by special pneumatic pistons engineered for the robot. By ingenious selection of the materials, the piston is designed to move very slowly (< 0.1 mm/s) with high dynamic friction and static friction lower than the dynamic. High dynamic friction ensures that the piston immediately stops when pressure is lost, preventing unsafe motion by the robot in the event of power loss. Low static friction eliminates the slip-stick effect enabling smooth acceleration ad deceleration of the piston. The system is registered to the MRI scanner by using images of four spheres attached to the robot. The system has been used in percutaneous needle access in animal and clinical trials.

In (Bricault et al., 2008, Zemiti et al., 2008), a CT and MR image-guided percutaneous intervention system named Light Puncture Robot is presented. An interesting aspect of the robot’s design is that instead of mounting the robot on the scanner table, the robot is designed to be supported on the patient's body. As a result, any physiological or unexpected movement of patient is compensated intrinsically, and allows the robot to naturally follow the respiratory motion or any other motion of the patient's body. The robot has a 3-DoF needle holder that translates and orients the needle and a 2-DoF support frame that adjusts the position of the holder. It uses a pneumatic actuator based on a clock making mechanism.

Applications in functional MRI (fMRI) research have also contributed to the development of MRI compatible robots. This has been pioneered by a research group at École polytechnique fédérale de Lausanne (EPFL). They have developed a robot remotely actuated by a hydraulic connection (Gassert et al., 2006) and also developed several different types of MRI compatible force and position sensors (Gassert et al., 2008b).

MRI compatible robots were also developed for Neurosurgery as intraoperative MRI imaging is a valuable tool for imaging the brain during surgery. The Neuroarm system (Sutherland et al., 2003, Sutherland et al., 2008, Motkoski et al., 2013) consists of two 7-DoF arms that are actuated by piezo motors. During neurosurgery, the patient is imaged with a fiducial, and the arms are brought next to the patient alongside the scanner. The arms are then registered to the MR image by digitizing the location of the fiducial with its tool tips. Then, the surgeon can access the patient's brain with the arms based on the intraoperative images. MRI compatibility requirements for these arms are less demanding then the other systems since the arms are not designed to go inside the scanner but stay alongside the scanner.

In urology, imaging prostate cancer with MRI and targeting the biopsy based on the image has been researched as a possible solution to overcome the limitation of current TRUS-guided biopsy, which is cancer "blind". As a result, most MRI-guided robots have been developed for prostate interventions.

Krieger et al. (Krieger et al., 2005, Krieger et al., 2011, Krieger et al., 2013) have developed a series of APT (Access to Prostate Tissue under MRI Guidance) robots for MRI-guided transrectal prostate biopsy. The first version (Krieger et al., 2005) presented an original 2-DoF mechanism that orients a needle-guide for transrectal access of the prostate. It was operated manually and the needle was tracked using a special imaging sequence for tracking active coils attached to it. The mechanism was maintained in the subsequent versions while registration and tracking was improved (Krieger et al., 2011) and a piezo motor was added for actuation (Krieger et al., 2013).

An actuated device was reported from the Nijmegen Medical Centre in the Netherlands (Schouten et al., 2010a). This was the first actuated MRI-guided transrectal biopsy device to be tested clinically (Yakar et al., 2011). Early results from their study provide positive evidence of the feasibility and safety of using the transrectal approach for needle placement and biopsies in the prostate. This device is remotely operated and, as reported in the literature, did not feature image-to-robot registration which would have allowed automatic re-positioning of the robot based on selected targets in the prostate.

Our lab has developed an MRI compatible pneumatic stepper motor, PneuStep (Stoianovici et al., 2007). The motor is made of MRI compatible material, actuated by air and encoded using fiber optic sensors. An MRI compatible robot for automated prostate brachytherapy (Patriciu et al., 2007) was developed using this motor. The further development of the MRI-guided robots using the PneuStep motor is reported in Chapter 4.

The interest in MRI-guided robots continues to grow due to the superior soft tissue contrast and diverse imaging capability of the MRI. One of the major challenges from an engineering perspective has been the development of MRI compatible actuation and sensing technologies. From clinical perspective, due to the high operation cost of the MRI scanner, interventions using MRI-guided robots should be designed to integrate well with existing clinical procedures, while providing enough benefit to offset the additional time of the scanner use.

1.2 Contribution of this Dissertation

This dissertation presents contributions in the area of image-guided medical robotics and image-guided interventions in urology. This section enumerates the main contributions.

1.2.1 Ultrasound Image-Guided Robot: Methods

1. TRUS Robot, a new ultrasound image-guided robot manipulating the ultrasound probe.
2. Measurement of the mechanical performance of the robot, including the stability of the Remote Center of Motion (RCM) mechanism.
3. A new method for calibrating the ultrasound probe and the needle-guide, verified through in-vitro image-guided targeting experiment. The constraints of the planar calibration rig is formulated and optimized in a novel way that separately optimizes the each component of calibration parameters and linearizes the constraints using matrix exponentials.
4. A new algorithm for filling the 3D volume from the set of image slices acquired from the calibrated probe. The algorithm speeds up the filling process by partitioning the volume in octree and sorting the slices.
5. A new algorithm for segmenting the acquired 3D volume image by combining the previous art of using non-orthogonal reslicing and probabilistic edge tracking method.

1.2.2 Ultrasound Image-Guided Robot: Applications

1. TRUS image-guided Robot Assisted Laparoscopic Prostatectomy. This was the first clinical trial of such approach using a robotic ultrasound, verifying the feasibility.
2. Robot assisted TRUS-guided systematic biopsy. Improved accuracy and repeatability over the unassisted case was demonstrated in in-vitro experiment.

3. Ultrasound elastography imaging of the prostate. Controlled palpation of the prostate through the robot manipulated probe and other external palpation devices was tested for improving the quality of the elastography image.
4. Algorithm for generating elastography image from the series of B-mode images acquired during the controlled probe motion. The algorithm allows the acquisition of an elastography image without access to the RF signal data.
5. A new method of ultrasound to CT image-fusion facilitated by using the TRUS robot as a common reference. his methods circumvents the use of an image similarity measures, which is difficult to define in cross modality fusion.

1.2.3 MRI-Guided Robot Methods and Applications

1. MRI-Safe robot for transrectal prostate biopsy and animal experiments.
2. MRI-Safe robot for transperineal prostate biopsy and clinical trial.

1.3 Dissertation Organization

This dissertation reports the development of ultrasound-guided and MRI-guided robots, and the results of substantial in-vitro, animal, and clinical experiments.

Development of the ultrasound-guided robot, the TRUS robot, is reported in Chapter 2. The structure of this ultrasound probe manipulating robot, its kinematics and the performance evaluation results are described in Section 2.1. The calibration procedure of the ultrasound probe and the subsequent image-guided needle targeting experiment results are described in Section 2.2. The software components of the system for robot control and image-guidance are described in Section 2.3. The algorithm for segmenting 3D ultrasound image of the prostate acquired by the TRUS robot is described in Section 2.4.

Application of the TRUS robot in several image-guided intervention procedures in urology is explored in several experiments. These results are reported in Chapter 3. Section 3.1 reports clinical trial results of using the TRUS robot for intraoperative guidance during robot assisted prostatectomy. Section 3.2 reports in-vitro accuracy measurement result of transrectal prostate biopsy using the TRUS robot. Section 3.3

reports the TRUS robot for acquiring ultrasound elastography images of prostate. Section 3.4 reports ultrasound and CT image-fusion facilitated by utilizing the TRUS robot as a common reference.

The development of the MRI-guided robots and results from its application in prostate biopsy are reported in Chapter 4. Two different types of MRI-guided robots were developed. The robot developed for transrectal prostate biopsy is presented in Section 4.1, along with the animal experiment result. The other, developed for transperineal biopsy and its initial clinical trial results are presented in Section 4.2.

2 Ultrasound Image-Guided Robot

Ultrasound Sonography (ultrasound) is an imaging modality that generates image of the internal anatomy by insonifying tissues with ultrasound wave and sensing the resulting echoes coming back from the tissues. At its beginning, ultrasound images were a single line showing the boundary of tissues (A mode imaging) and have evolved into 2 dimensional (2D) cross section (B-mode imaging), and more recently into 3D volume image (3D ultrasound). Furthermore, advanced imaging modes that can image different tissue properties such as the blood flow (Doppler imaging), and stiffness (elastography), have been developed.

Among the medical imaging modalities used for guiding the intervention process, ultrasound imaging has distinct advantages. It is inexpensive and widely available in clinics, provides real-time images, and does not use ionizing radiation. These advantages make ultrasound a useful modality for guiding and monitoring the intervention in real-time.

Integrating the robots with ultrasound-guided interventions has the potential to improve precision and accuracy. In addition, robots allow 2D image slices acquired to be tracked and combined into 3D volume images. While 3D ultrasound images can be also acquired by using special 3D ultrasound probes or by tracking the probe with other means such as optical trackers, robotic 3D ultrasound image acquisition has several potential advantages. The 3D ultrasound probes are not widely available in the clinic and their typical field of view (FOV) and resolution are limited by the transducer array size. On the other hand, robotic manipulation allows 3D ultrasound image acquisition using any 2D probes and the field of view is not limited to the size of the transducer array. Compared to other probe tracking methods, because robots are capable of precisely tracking and manipulating an ultrasound probe, they can generate evenly spaced slices and enable superior 3D volume reconstruction (Priester et al., 2013).

In urology, ultrasound-guidance is routinely used in many image-guided interventions such as prostate biopsy, brachytherapy and cryoablation of prostate or kidney. The ultrasound image-guided robots developed at our Urology Robotics lab were built with these applications in mind and resulted in two ultrasound-guided robots that manipulate different types of ultrasound probes. The following chapter describes the development of the complete ultrasound-guided robot system for image-guided intervention of prostate and kidney, including the design of the robot hardware, calibration of the robot, the development of image-guidance software for 3D ultrasound imaging, and the segmentation of the prostate.

2.1 The TRUS-Robots

The TRUS-Robot (Figure 2.1) is an ultrasound probe manipulator developed at our laboratory. Two different versions of the robot, TRUS1 and TRUS2 were developed. The TRUS1-Robot manipulates the convex abdominal probe for the examination of the kidney. The robot is an updated version of a previous ultrasound probe manipulator (Goldberg et al., 2001). The TRUS2-Robot was specifically developed for manipulating the transrectal ultrasound (TRUS) probe for the image-guided interventions of the prostate.

The development of the robots has been reported in a journal article (Stoianovici et al., 2013a). Among the authors, Doru Petrisor and Felix Schaefer contributed to the manufacturing of the robots and my personal contribution to this project was:

- Kinematic analysis and mechanical performance evaluation of the robots.

2.1.1 Robot Structure and Kinematics

Figure 2.2 and Figure 2.3 show the kinematic structure of the two robots. Both consist of a Remote Center of Motion (RCM) module and different probe drivers. The TRUS1-Robot has 3-DoF implemented by 2-DoF on the RCM module and 1-DoF on a rotary (R) type probe driver. The TRUS2-Robot presents 4-

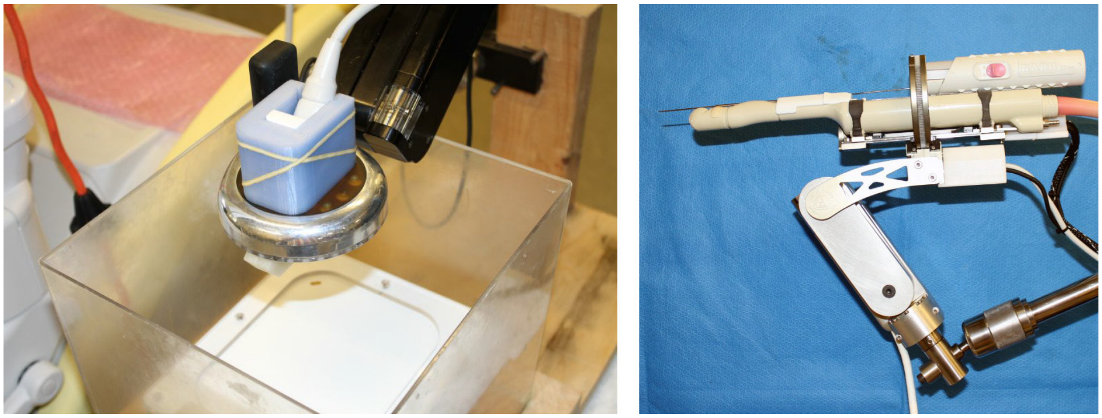

Figure 2.1: TRUS1 (left) and TRUS2 (right) robots

DoF implemented by 2-DoF on the RCM module and 2-DoF on a rotary and translation (RT) type probe driver.

The RCM mechanism (Funda et al., 1995) is a mechanism that generates a rotating motion about a fixed point (RCM point) distal from the mechanism, typically in 2-DoF without physical revolute joint attached at the fixed point. This mechanism is commonly found in minimally invasive surgical robots (Funda et al., 1995, Eldridge et al., 1996, Taylor and Stoianovici, 2003, Piccigallo et al., 2010, Kuo et al., 2012) where medical instruments are required to pivot about a minimally invasive entry port or natural orifice. Both TRUS1 and TRUS2 robots use the same RCM module that provides 2 rotational DoF with axes intersecting at the RCM point. The module uses a parallelogram mechanism implemented with two belts (Stoianovici et al., 2006) . This represents one of the smallest RCM implementations and provides a novel adjustment to relocate the RCM point.

Probe drivers attached to the RCM module implement additional DoF. The R type probe driver of the TRUS1-Robot rotates the probe about an additional axis passing through the RCM point. The RT type probe driver of the TRUS2-Robot also implements a translation along this axis.

The combination of the RCM module and probe drivers, along with the design of the probe adapter that sets the position of the RCM point with respect to the probe, implements the necessary and safe motion for manipulating the probe. In the TRUS1-Robot, the RCM point is set to coincide with the tip of the

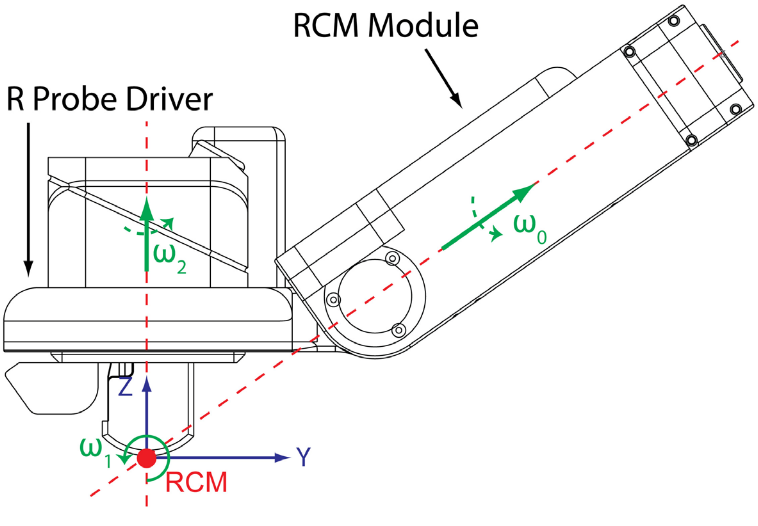

Figure 2.2: Kinematic diagram of the TRUS1-Robot

mounted abdominal probe as shown in Figure 2.2. As a result, the 3 rotational DoF of the robot makes the probe roll on the patient's skin. In the TRUS2-Robot, the probes are mounted along the rotary axis of the driver as shown in Figure 2.3. The robot is then placed such that the RCM point is located at the anus. This allows the probe to be oriented about the fulcrum point and inserted with motion that is similar to the manual operation of the TRUS.

Our previous ultrasound probe manipulator (Goldberg et al., 2001), and the TRUS1-Robot have 3-DoF and both are based on the RCM module. But the original ultrasound robot was designed for linear array abdominal probes and uses a translational DoF to maintain coupling of the probe with the skin. For this type of probe 2 rotational DoF are sufficient, as the rotation about the normal to the image plane is not required due to the shape of the probe. On the other hand, for convex array abdominal probes, having a curved surface that rolls on the skin, the 3rd rotational DoF is required to rotate the probe about the normal of the image plane.

Both TRUS robots are mounted on a passive support arm that can be attached to a fixed base, for example, an operation table. The passive support arm presents 7 degree of adjustment (DoA) with two spherical joints (3R) and one cylindrical joint (R) which can be locked in place to support the device as needed.

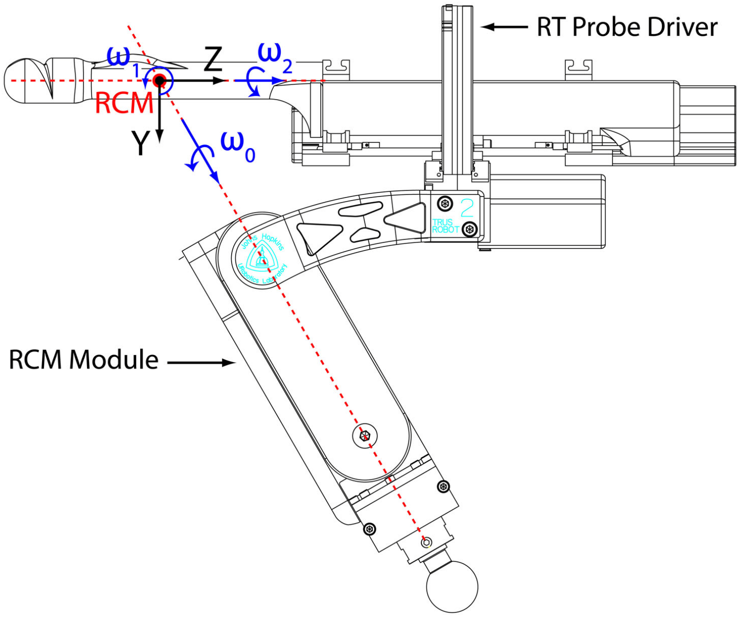

Figure 2.3: Kinematic diagram of the TRUS2-Robot

Forward Kinematics

The robot base coordinate system B is placed at the RCM point and the probe coordinate system P is defined such that it coincides with the robot base coordinate system at zero configuration of the robot. For both TRUS robots, the rotation in 2 axes of the RCM module by $\theta_0$and $\theta_1$causes the probe and driver to rotate about the RCM point about two axes $\vec{\boldsymbol{\omega}}_0$ and $\vec{\boldsymbol{\omega}}_1$ by θ_0 and θ_1. This is followed by a rotation θ_2 about $\vec{\boldsymbol{\omega}}_2$ by probe driver and for TRUS2-Robot, an additional translation θ_3 along the $\vec{\boldsymbol{\omega}}_2$.

Using matrix exponentials, a rotation matrix $\mathrm{e}^{\widehat{\omega}\theta}$ corresponding to the rotation about a given unit axis $\vec{\boldsymbol{\omega}} = \left[\omega_x, \omega_y, \omega_z\right]^T$ by rotation angle θ can be calculated by Rodriguez formula

$$\mathrm{e}^{\widehat{\omega}\theta} = \mathrm{I} + \sin\theta\, \widehat{\omega} + (1 - \cos\theta)\widehat{\omega}^2 \tag{2.1}$$

where $\widehat{\omega} = \begin{bmatrix} 0 & -\omega_z & \omega_y \\ \omega_z & 0 & -\omega_x \\ -\omega_y & \omega_x & 0 \end{bmatrix}$ is a skew symmetric matrix generated from vector $\vec{\omega}$, representing cross product such that $\widehat{\omega}\vec{x} = \vec{\omega} \times \vec{x}$.

Then, by using product of exponential (Murray et al., 1994), forward kinematics of the robot that describes the configuration of the probe coordinate system ${}^B_P G$ as a function of joint angle $\vec{\theta} = [\theta_0, \theta_1, \theta_2, \theta_3]^T$ is given as

$${}^B_P G(\vec{\boldsymbol{\theta}}) = \begin{bmatrix} e^{\widehat{\omega_0}\theta_0} e^{\widehat{\omega_1}\theta_1} e^{\widehat{\omega_2}\theta_2} & \vec{\mathbf{0}} \\ \vec{\mathbf{0}}^{\boldsymbol{T}} & 1 \end{bmatrix} \tag{2.2}$$

for TRUS1-Robot and

$${}^B_P G(\vec{\boldsymbol{\theta}}) = \begin{bmatrix} e^{\widehat{\omega_0}\theta_0} e^{\widehat{\omega_1}\theta_1} e^{\widehat{\omega_2}\theta_2} & \theta_3 \cdot e^{\widehat{\omega_0}\theta_0} e^{\widehat{\omega_1}\theta_1} e^{\widehat{\omega_2}\theta_2} \vec{\omega}_2 \\ \vec{\mathbf{0}}^{\boldsymbol{T}} & 1 \end{bmatrix} \tag{2.3}$$

for TRUS2-Robot. The kinematic parameters, $\vec{\boldsymbol{\omega}}_0$, $\vec{\boldsymbol{\omega}}_1$, $\vec{\boldsymbol{\omega}}_2$ and $\vec{\boldsymbol{\omega}}_3$, which are the direction of the rotation axes in robot base coordinate system are as below.

TRUS1 : $\vec{\boldsymbol{\omega}}_0 = [0, \cos 35°, \sin 35°]^T$ $\vec{\boldsymbol{\omega}}_1 = [1,0,0]^T$ $\vec{\boldsymbol{\omega}}_2 = [0,0,1]^T$

TRUS2 : $\vec{\boldsymbol{\omega}}_0 = [0, \sin 60°, \cos 60°]^T$ $\vec{\boldsymbol{\omega}}_1 = [1,0,0]^T$ $\vec{\boldsymbol{\omega}}_2 = [0,0,1]^T$

Inverse Kinematics

The inverse kinematics problem for the TRUS robot is orienting the probe coordinate system to an arbitrary orientation represented by rotation matrix R by adjusting joint angles of the three rotations. Decomposing an arbitrary rotation matrix R as a product of three rotation matrix about three different axis $e^{\widehat{\omega_0}\theta_0}e^{\widehat{\omega_1}\theta_1}e^{\widehat{\omega_2}\theta_2}$ is known as 'generalized Euler angle' problem and solution is known to exist if and only if first two and last two axes are perpendicular (Davenpor.Pb, 1973), i.e. $\vec{\boldsymbol{\omega}}_{\mathbf{0}} \perp \vec{\boldsymbol{\omega}}_{\mathbf{1}}$ and $\vec{\boldsymbol{\omega}}_{\mathbf{1}} \perp \vec{\boldsymbol{\omega}}_{\mathbf{2}}$. This is the case for both TRUS robots, and the inverse kinematics problem

$$R = e^{\widehat{\omega_0}\theta_0}e^{\widehat{\omega_1}\theta_1}e^{\widehat{\omega_2}\theta_2} \tag{2.4}$$

can be solved for $\theta_0, \theta_1, \theta_2$as below.

First, multiply both side by $\vec{\boldsymbol{\omega}}_{\mathbf{2}}$, since $e^{\widehat{\omega_2}\theta_2}\vec{\boldsymbol{\omega}}_{\mathbf{2}} = \vec{\boldsymbol{\omega}}_{\mathbf{2}}$

$$\vec{\boldsymbol{v}} = R\vec{\boldsymbol{\omega}}_{\mathbf{2}} = e^{\widehat{\omega_0}\theta_0}e^{\widehat{\omega_1}\theta_1}e^{\widehat{\omega_2}\theta_2}\vec{\boldsymbol{\omega}}_{\mathbf{2}} = e^{\widehat{\omega_0}\theta_0}e^{\widehat{\omega_1}\theta_1}\vec{\boldsymbol{\omega}}_{\mathbf{2}} = \vec{\boldsymbol{v}} \tag{2.5}$$

The equation

$$e^{\widehat{\omega_0}\theta_0}e^{\widehat{\omega_1}\theta_1}\vec{\boldsymbol{\omega}}_{\mathbf{2}} = \vec{\boldsymbol{v}} \tag{2.6}$$

is one of Paden-Kahan Subproblem (Murray et al., 1994) which has two pair of solution $[\theta_0, \theta_1]$. Once $[\theta_0, \theta_1]$ is calculated, equation can be manipulated to

$$e^{-\widehat{\omega_1}\theta_1}e^{-\widehat{\omega_0}\theta_0}R\vec{\boldsymbol{\omega}}_1 = e^{\widehat{\omega_2}\theta_2}\vec{\boldsymbol{\omega}}_1 = \vec{\boldsymbol{q}} \tag{2.7}$$

This equation

$$e^{\widehat{\omega_2}\theta_2}\vec{\boldsymbol{\omega}}_{\mathbf{1}} = \vec{\boldsymbol{q}} \tag{2.8}$$

is another Paden-Kahan Subproblem that can be solved for θ_2. The detailed solution of Paden-Kahan subproblems are described in the Appendix.

2.1.2 Motion Analysis

While the accuracy and precision of each robot axis is the basic measure of its mechanical performance, for the TRUS robots, another important measure is the stability of the RCM. For an ideal RCM, the center of any probe rotations generated by the robot will be fixed at the same point in the space. However, this may not be true due to manufacturing tolerances and deformations of the links. Therefore, the stability of RCM can be quantified by the ‘proximity’ of the center of rotations.

Mechanical performance of the TRUS robots was evaluated using an optical tracking system (Polaris, NDI, ON, Canada). For both robots, a 6-DoF active marker was attached to the robot in place of ultrasound probe as shown in Figure 2.4 to measure the pose (= orientation and translation) ${}^{O}_{M}G$, of the marker with respect to the tracker camera at multiple robot joint angles. Accuracy, precision and RCM stability were evaluated from the measured pose data as described below.

Accuracy and Precision Measurement

For each axis of the robot, a set of joint angles equally distributed throughout the range of the axis motion was selected. Then for each joint angle j_i, the axis was commanded to j_i from the reference configuration (zero joint angles) and the pose of the marker at the reference ${}^{O}_{M}G_0$ and the commanded joint angle ${}^{O}_{M}G_i$ were measured. From this, relative pose G_i of the robot at j_i with respect to the reference configuration was calculated ($G_i = {}^{O}_{M}G_0^{-1}\,{}^{O}_{M}G$). This was repeated 10 times for each joint angle.

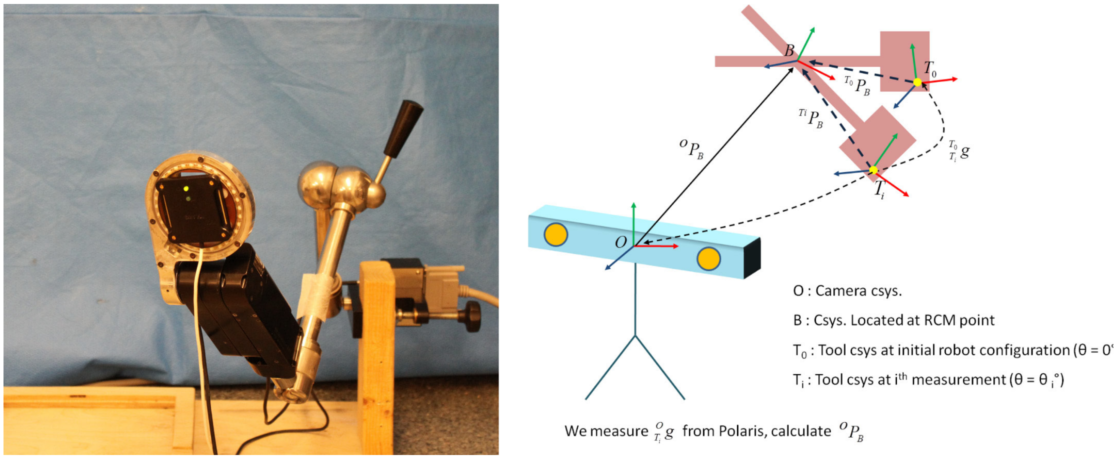

Figure 2.4: Experiment setup for the motion analysis

For the rotational joint, the relative orientation was decomposed into axis $\vec{p}_i$ and angle of rotation θ_i and for translational joint, the magnitude of the relative translation θ_i, was calculated. The accuracy and precision of each axis in the commanded motion to joint angle j_i, was defined as the average error between j_i and θ_i and the difference between the maximum and minimum error, respectively. The result is summarized in Table 1 for TRUS 1 and Table 2 for TRUS 2. On average three axes of the TRUS1-Robot had accuracy of $[-0.886°, -0.228°, -0.757°]$ and precision of $[0.051°, 0.020°, 0.363°]$. Four axes of the TRUS 2-Robot had accuracy of $[-0.328°, -0.729°, -0.361°, -0.054 \text{ mm}]$ and precision of $[0.147°, 0.038°, 0.021°, 0.018 \text{ mm}]$.

Table 1: Accuracy and precision of TRUS1 Robot

i	**TRUS1-Axis 0**			**TRUS1-Axis 1**			**TRUS1-Axis 2**		
	j_i[°]	**Error $(j_i - \theta_i)$[°]**		**j_i[°]**	**Error $(j_i - \theta_i)$[°]**		**j_i[°]**	**Error $(j_i - \theta_i)$[°]**	
		Accuracy	**Precision**		**Accuracy**	**Precision**		**Accuracy**	**Precision**
1	10	-0.229	0.271	5	0.013	0.046	15	0.014	0.337
2	20	-0.538	0.025	10	-0.019	0.015	30	-0.354	0.098
3	30	-0.727	0.014	15	-0.174	0.012	45	-0.384	0.105
4	40	-0.851	0.020	20	-0.110	0.025	60	-0.515	0.660
5	50	-1.019	0.015	25	-0.098	0.025	75	-0.545	0.675
6	60	-1.092	0.013	30	-0.374	0.014	90	-0.617	0.653
7	70	-1.315	0.018	35	-0.279	0.019	105	-0.904	0.613
8	80	-1.316	0.030	40	-0.320	0.018	120	-0.996	0.506
9				45	-0.429	0.008	135	-1.096	0.515
10				50	-0.486	0.016	150	-1.153	0.070
11							165	-1.221	0.061
12							180	-1.313	0.059
Mean		-0.886	0.051		-0.228	0.020		-0.757	0.363

Table 2: Accuracy and precision of TRUS2 Robot

i	TRUS2-Axis 0				TRUS2-Axis 1		
	j_i[°]	Error $(j_i - \theta_i)$[°]			j_i[°]	Error $(j_i - \theta_i)$[°]	
		Accuracy	Precision			Accuracy	Precision
1	10	-0.183	0		5	-0.018	0.148
2	20	-0.608	0.003		10	-0.142	0.032
3	30	-0.108	0.004		15	-0.665	0.112
4	40	0.169	0.444		20	-1.243	0.037
5	50	-0.348	0.026		25	-0.549	0
6	60	-0.441	0.688		30	-0.457	0.010
7	70	-0.343	0		35	-1.281	0
8	80	-0.760	0.014		40	-1.165	0
9					45	-1.045	0
Mean		-0.328	0.147			-0.729	0.038

Set	TRUS2-Axis 2				TRUS2-Axis 3		
	j_i[°]	Error $(j_i - \theta_i)$[°]			j_i[mm]	Error $(j_i - \theta_i)$[mm]	
		Accuracy	Precision			Accuracy	Precision
1	10	0.543	0		6	-0.034	0.016
2	20	-0.148	0.010		12	-0.051	0.015
3	30	-0.173	0		18	-0.063	0.024
4	40	0.455	0.009		24	-0.033	0.033
5	50	-0.570	0.001		30	-0.029	0.016
6	60	-0.756	0.021		36	-0.058	0.019
7	70	-0.808	0		42	-0.067	0.016
8	80	-0.612	0		48	-0.081	0.013
9	90	-1.179	0.152		54	-0.058	0.014
10					60	-0.069	0.016
Mean		-0.361	0.021			-0.054	0.018

RCM Stability Measurement

For each rotational axis of the robot, set of joint angles equally distributed throughout the range of the axis motion was selected and axis was commanded to each joint angle j_i . As it was done in the accuracy and precision measurement, the relative pose G_i robot at j_i with respect to the reference configuration was calculated ($G_i = {}^{O}_{M}G_0^{-1}\,{}^{O}_{M}G$). The axis of screw motion corresponding to each relative pose G_i was calculated, leading to a bundle of axes for each measurement set.

Since the motion generated during each measurement set is pure rotation about the robot's axes, for ideal RCM, screw axes from each G_i within the same measurement set should be aligned with each other and axes for all measurement data should intersect at the same RCM point. Figure 2.5 below shows the plot of the screw axis calculated from each measurement and it can be seen that this is not the case. For more quantified measurement, the intersection between the axes bundles were calculated as the point that minimizes the sum of squared distance to the axes bundles. Also, the mean distance from the intersection to each axis of the bundles were calculated. The results are summarized in Table 3. The fluctuation of the RCM point is within 1.17 mm.

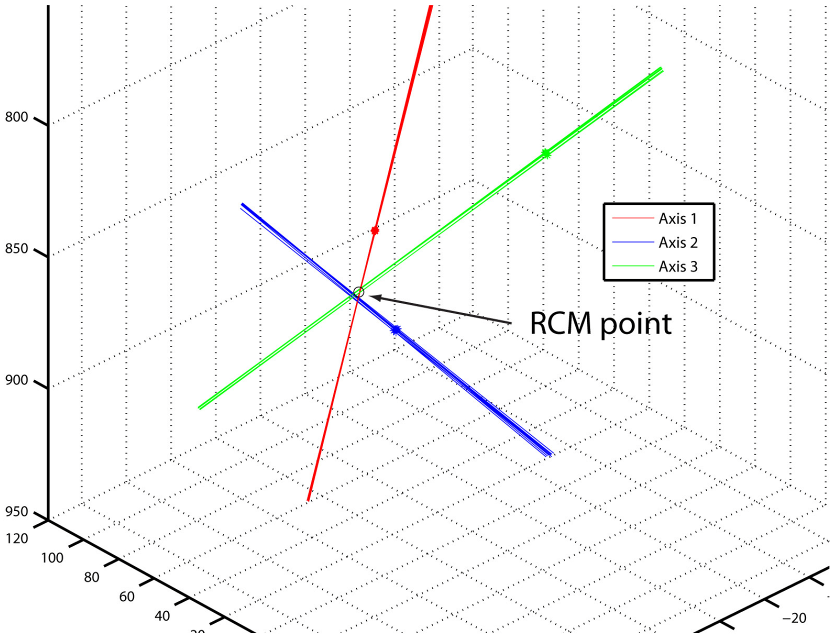

Figure 2.5: RCM stability analysis

Table 3: RCM stability of TRUS 2 Robot

<table>
<tr><th></th><th>Intersection Location</th><th colspan="6">Mean Distance to axes from the intersection</th></tr>
<tr><td>Axis 1 & 2</td><td>(27.6, 49.4, -1859.0)</td><td colspan="3">0.17</td><td colspan="3">0.40</td></tr>
<tr><td>Axis 2 & 3</td><td>(28.7, 49.8, -1858.1)</td><td colspan="3">0.83</td><td colspan="3">0.85</td></tr>
<tr><td>Axis 1 & 3</td><td>(27.8, 48.8, -1857.0)</td><td colspan="3">0.47</td><td colspan="3">0.84</td></tr>
<tr><td>Axis 1 & 2 & 3</td><td>(27.9, 49.4, -1858.2)</td><td colspan="2">0.57</td><td colspan="2">0.80</td><td colspan="2">1.17</td></tr>
</table>

2.2 Ultrasound Probe Calibration

For the image-guidance of the TRUS robots, ultrasound images from the mounted probes are captured to the computer for further processing by digitizing the output video signal from the ultrasound scanner using a frame grabber. Each pixel of the captured images has a 'pixel coordinate' defined with respect to the image coordinate system. To determine the physical location of each pixel with respect to the robot base coordinate system, unknown transformation between the robot and the image coordinate system needs to be identified. This procedure is called 'probe calibration'.

Probe calibration is a procedure required not only for the robot manipulated probe but for all probes that are tracked by some means (optical, magnetic or encoded passive arms). Several ultrasound probe calibration methods (Prager et al., 1998, Boctor et al., 2003, Boctor et al., 2004, Rousseau et al., 2005, Hsu et al., 2008) have been developed. Common to all calibration methods is a calibration rig that is imaged with the tracked probes. The rigs are typically constructed of strings (Boctor et al., 2003, Boctor et al., 2004, Hsu et al., 2008) or planes (Prager et al., 1998, Rousseau et al., 2005) submersed in a water basin. In ultrasound image, strings generate points and planes generate lines. Imaged features (points or lines) of the rigs and calibration parameters must satisfy a set of constraint equations. Typically, these are optimized for the parameters based on experimental images.

Previous ultrasound calibration methods could be applied to calibrate the probes manipulated by TRUS robot, with associated advantages and disadvantages. First, in terms of the calibration rig design, planes generate lines in the image that may be easier to detect by automated means then the points generated by the strings (Mercier et al., 2005). Also, the calibration methods using string calibration rigs usually assume a precisely known geometric relationship between its strings, making it more difficult to manufacture. Therefore, a planar calibration rig was selected for the calibration method developed.

In previous calibration methods using the planar rig, all calibration parameters were formulated into a single constraint equation, leading to a high-dimensional non-linear optimization problem. However, we observed that the optimization problem may be simplified by a sequential approach that separates the scale, isocenter, orientation, and offset parameter identifications. In our case, we further simplified the identification by using a linearizing the constraint equations using matrix exponentials.

The calibration methods and the accuracy of the calibration and image-guided targeting using the calibrated probe were reported in a journal article (Kim et al., 2013). Among the authors, Professor Gregory Chirikjian provided valuable advice on the solution of the optimization problem.

My personal <u>contribution</u> to this project was:

- Formulation of the calibration method.
- Running experiments for probe and needle guide calibration.
- Running experiments for verifying the accuracy of the calibration and image-guided targeting using the calibrated probe.

2.2.1 Calibration Problem

As shown in Figure 2.6, the configuration of the image coordinate system with respect to the TRUS Robot coordinate system is given by $F(\theta_i){}_I^PG$, where $F(\theta_i)$ is the forward kinematics of the robot describing the configuration of the probe coordinate system P with respect to the robot base coordinate system at joint angle θ_i, and ${}_I^PG$ is a constant probe calibration matrix describing the configuration of the image coordinate system I with respect to the probe coordinate system P. The probe calibration matrix ${}_I^PG$ may be expressed as:

$$
{}^{P}_{I}G = \begin{bmatrix} X & \vec{\boldsymbol{x}} \\ \vec{\boldsymbol{0}}^{T} & 1 \end{bmatrix} \begin{bmatrix} s_x & 0 & 0 & 0 \\ 0 & s_y & 0 & 0 \\ 0 & 0 & 0 & 0 \\ 0 & 0 & 0 & 1 \end{bmatrix} \tag{2.9}
$$

where, s_x and s_y are the scale factors (mm/pixel) in x and y directions of the image and S is the scaling matrix, X is a rotation matrix and $\vec{\boldsymbol{x}}$ is an offset between the two systems. The calibration maps any point ${}^{I}\vec{\boldsymbol{p}} = [u, v, 0]^T$ in the ultrasound image measured in pixels to a point ${}^{P}\vec{\boldsymbol{p}} = {}^{P}_{I}G\ {}^{I}\vec{\boldsymbol{p}} = [x, y, z]^T$ in the probe coordinate system measured in mm.

The scope of the calibration is to identify the calibration parameters $(X, \vec{\boldsymbol{x}}, s_x, s_y)$ from the combined robot-probe system based on imaging experiments that image a calibration rig from multiple robot positions $(F(\theta_i))$. Scale, orientation and offset parameters are sequentially identified as follows.

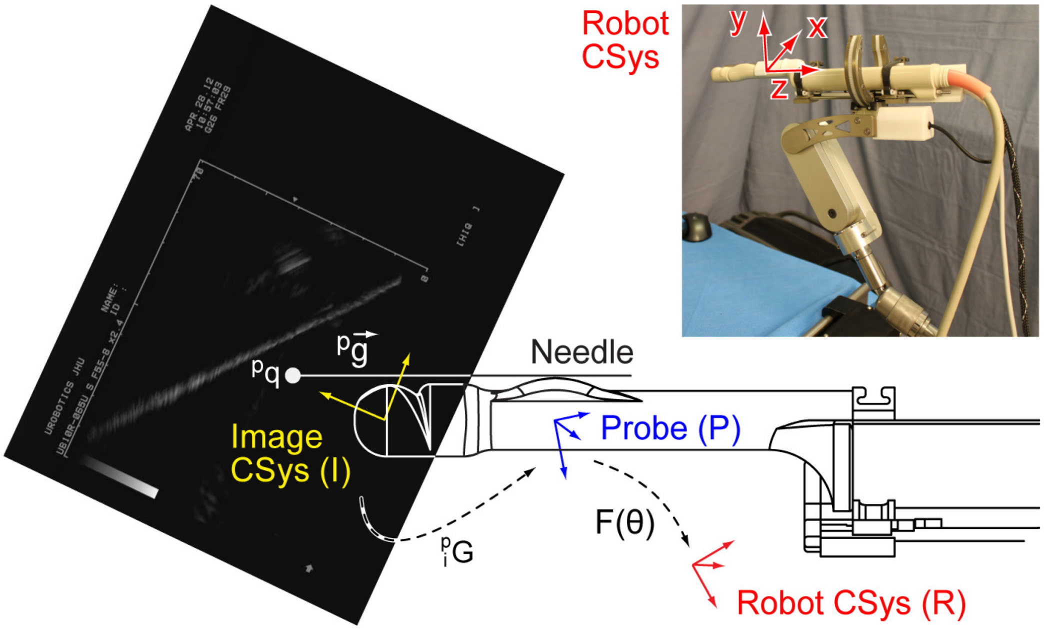

Figure 2.6: Image, probe, and robot coordinate systems (CSys)

2.2.2 Scale Calibration and Identification of Isocenter

Scale factor of the calibration converts image coordinate measured in pixels to physical dimension in mm. While one may think that single scale factor will be enough, the digitization process of the video signal may introduce change in pixel aspect ratio in some cases and therefore the scale factors should be identified in both directions$[s_x, s_y]$. For example, according to ITU-R Recommendation BT.601, digitization of a PAL video signal results 720 x 576 digital image with non-square pixel aspect ratio (width/height) 59/54. For TRUS robot, each s_x and s_y was determined from the mm/pixel ratio of the scale bars available in the image (Figure 2.7). If the scale-bars provided by the ultrasound manufacturer may not be reliable, scale factor should be identified by imaging a calibration rig with known physical dimensions.

Commercial ultrasound image systems are equipped with the function to change the depth settings, which in turn changes the scale factor$[s_x, s_y]$. In addition, if the origin of the image coordinate system is defined on the upper left hand corner of image as it is typically done, its location moves with the change of depth setting and thus the offset $\vec{\boldsymbol{x}}$ of the calibration also changes. However, if the origin of the image coordinates system is conveniently set at the image isocenter ($\vec{\boldsymbol{O}}$ in Figure 2.7), offset can remain constant despite the depth setting change. Physically this isocenter corresponds to the center of the transducer array.

The location of the isocenter in the image can be identified from the images of the planar calibration rig obtained at two depth settings (S_1 and S_2) from several dissimilar robot orientations. For each orientation i and two depth settings (S_1 and S_2), the image of the calibration rig forms a two parallel line 1 and 2 defined by a point $\vec{\boldsymbol{p}}_{i1}$and $\vec{\boldsymbol{p}}_{i2}$and a direction $\vec{\boldsymbol{l}}_i$. Then the pixel distance from the isocenter $\vec{\boldsymbol{O}}$ to line 1 is$\left(\vec{\boldsymbol{p}}_{i1} - \vec{\boldsymbol{O}}\right)^T \vec{\boldsymbol{l}}_i^{\perp}$, where and $\vec{\boldsymbol{l}}_i^{\perp}$ is the direction normal to $\vec{\boldsymbol{l}}_i$. These distances are proportional to the depth settings, therefore:

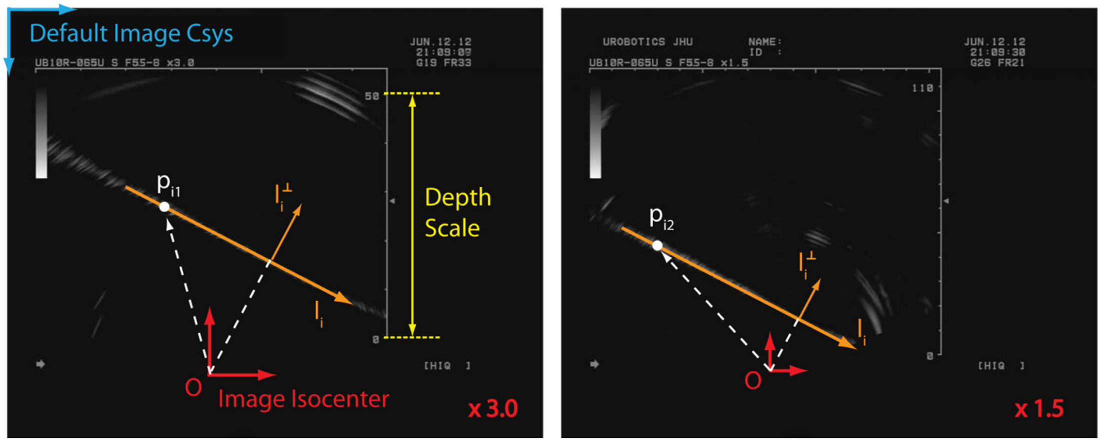

Figure 2.7: Image scale and scale invariant point O defining the image coordinates origin

$$\left(\vec{\boldsymbol{p}}_{i1} - \vec{\boldsymbol{O}}\right)^{\boldsymbol{T}} S_1 \vec{\boldsymbol{l}}_i^{\perp} = \left(\vec{\boldsymbol{p}}_{i2} - \vec{\boldsymbol{O}}\right)^{\boldsymbol{T}} S_2 \vec{\boldsymbol{l}}_i^{\perp} \tag{2.10}$$

In this scalar equation the two unknowns are the pixel coordinates of the isocenter, $\vec{\boldsymbol{O}} = [u_o, v_o]^T$. The measurements of more than two orientations, lead to an over determined system:

$$\begin{bmatrix} (S_1 - S_2)\vec{\boldsymbol{l}}_i^{\perp} \\ \vdots \end{bmatrix} \boldsymbol{O} = \begin{bmatrix} (S_1\vec{\boldsymbol{p}}_{i1} - S_2\vec{\boldsymbol{p}}_{i2})^{\mathrm{T}}\vec{\boldsymbol{l}}_i^{\perp} \\ \vdots \end{bmatrix} \tag{2.11}$$

which can be solved for $\vec{\boldsymbol{O}}$. In all subsequent calibrations, pixels are described with respect to the image coordinate located at the isocenter and calibrated scales S are applied, so that the units of the points and lines selected in the image are directly expressed in mm.

2.2.3 Orientation Calibration

The orientation component of the calibration, defined by rotation matrix X, is determined from the constraints between the images of the calibration rig observed at different orientation. The image of the plane calibration rig obtained at a joint angle θ_i, is a line along the direction $\vec{\boldsymbol{l}}_i$ which can be expressed in the robot base coordinate as:

$$\vec{\boldsymbol{L}}_i = F(\theta_i)^P_I G \vec{\boldsymbol{l}}_i = R_i X \vec{\boldsymbol{l}}_i \tag{2.12}$$

This image corresponds to the line of intersection between the ultrasound image plane and the calibration rig plane. Therefore, the constraint between the images is that all the lines are a line on the plane of the calibration rig.

Two different methods for calibration utilizing this constraint were developed. The first method linearizes the constraint and iteratively searches for the solution starting from the initial estimate X_0. The second method utilizes the robotic manipulation of the probe, using the image of the calibration rig at multiple probe rotations about the same axis. By using this additional constraints on the orientations of the probe, a closed form solution for X can be obtained.

The first method using an iterative solution has the advantages that any orientation can be used, but requires more observation of the calibration rig than the second. However, the closed form solution in the second method is sensitive to the measurement noises and even a slight error in the measurement of the line direction from the image of the calibration rig leads to improbable solution.

Iterative solution using free probe motion

The lines $\vec{\boldsymbol{L}}_i, \vec{\boldsymbol{L}}_j, \vec{\boldsymbol{L}}_k$ from the images acquired at three robot orientations satisfy following constraint:

$$\vec{\boldsymbol{L}}_{\boldsymbol{i}}^{\boldsymbol{T}}\left(\vec{\boldsymbol{L}}_j \times \vec{\boldsymbol{L}}_{\boldsymbol{k}}\right) = \vec{\boldsymbol{l}}_{\boldsymbol{i}}^{\boldsymbol{T}} X^T R_i^T \left(R_j X \widehat{\boldsymbol{l}_{\boldsymbol{j}}} X^T R_j^T R_k X \vec{\boldsymbol{l}}_{\boldsymbol{k}}\right) = 0 \tag{2.13}$$

where, the $\hat{a}$ is a skew-symmetric matrix representation of the cross product such that $\hat{a}\vec{\boldsymbol{x}} = \vec{\boldsymbol{a}} \times \vec{\boldsymbol{x}}$.

This constraint equation is non-linear. Instead of using a non-linear optimization method as commonly done by others (Boctor et al., 2003, Hsu et al., 2008, Prager et al., 1998, Rousseau et al., 2005), we use a simpler method based on linearization. An initial estimate of the image orientation X_0 may be calculated from the CAD model of the ultrasound probe. The actual X will be slightly rotated by a vector $\vec{\delta}$. For a small rotations $|\delta|$, the image orientation can be approximated as:

$$X = X_0 e^{\hat{\delta}} \approx X_0(I + \hat{\delta}) \tag{2.14}$$

This approximation linearizes the constrain equations:

$$\vec{\boldsymbol{l}}_i^T \left(I + \hat{\delta}\right)^T Q_{ji}^T \left(I + \hat{\delta}\right) \widehat{\boldsymbol{l}_j} \left(I + \hat{\delta}\right)^T Q_{jk}(I + \hat{\delta}) \vec{\boldsymbol{l}}_k \tag{2.15}$$

where $Q_{ji} = X_0^T R_j^T R_i X_0$ and $Q_{jk} = X_0^T R_j^T R_k X_0$. Expanding and neglecting higher order terms in $\hat{\delta}$ leads to the following linear system:

$$\begin{bmatrix} \vec{\boldsymbol{a}}_{ji}^T \widehat{\boldsymbol{b}_{jk}} \left(I - Q_{ji}\right) + \vec{\boldsymbol{b}}_{ji}^T \widehat{\boldsymbol{a}_{jk}} \left(I - Q_{jk}\right) \\ \vdots \end{bmatrix} \delta = \begin{bmatrix} \alpha_{ijk} \\ \vdots \end{bmatrix} \tag{2.16}$$

where: $a_{ji} = Q_{ji} \vec{\boldsymbol{l}}_i$, $b_{ji} = \widehat{l_j} Q_{ji} \vec{\boldsymbol{l}}_i$, $\alpha_{ijk} = \vec{\boldsymbol{l}}_i^T Q_{ij} \widehat{\boldsymbol{l}_j} Q_{jk} \vec{\boldsymbol{l}}_k$

For n robot orientations the number of combinations of 3 imaged lines is C_3^n. These can be used to formulate an over determined linear system, that can be solved for δ, determining the image orientation X. This procedure is iterated by updating the initial estimate to $X_0 = X$ until the convergence is reached ($|\delta|$ becomes very small).

Closed form solution using constrained motion

Let's denote by $\mathbf{n}$ the normal of the calibration rig plane. When the manipulator rotates the probe about an axis ω by angle θ_i, the resulting line $\mathbf{l}_i$ in the image corresponds to a line $\mathbf{L}_i$ on the plane. These are related by:

$$e^{\widehat{\omega}\theta_i} X \boldsymbol{l}_i = \boldsymbol{L}_i \tag{2.17}$$

where, X is the unknown rotation matrix describing the orientation of the image coordinate system with respect to the reference coordinate system.

Since the line $\boldsymbol{L}_i$ lies on the calibration rig plane of normal $\boldsymbol{n}$**,** in the reference coordinate system

$$\boldsymbol{n}^T e^{\widehat{\omega}\theta_i} X \boldsymbol{l}_i = 0 \tag{2.18}$$

and, by introducing $\boldsymbol{n}' = X^T \boldsymbol{n}$ and $\boldsymbol{\omega}' = X^T \boldsymbol{\omega}$, this can be reformulated as

$$\boldsymbol{n}'^T e^{\widehat{\omega'}\theta_i} \boldsymbol{l}_i = 0 \tag{2.19}$$

Parameterize $\boldsymbol{n}' = \left[s_\phi c_\alpha, s_\phi s_\alpha, c_\phi\right]^T$ and $\boldsymbol{\omega}' = \left[s_\psi c_\beta, s_\psi s_\beta, c_\psi\right]^T$. Notice that $\boldsymbol{l}_i$ is a line on image plane that is set to be XY plane and thus have coordinate of $\boldsymbol{l}_i = \left[l_{ix}, l_{iy}, 0\right]^T$. The unknowns are the $\phi, \psi, \alpha, \beta$. At the zero configuration $\theta_0 = 0$, equation (2.19) becomes

$$\boldsymbol{n}'^T \boldsymbol{l}_0 = s_\phi c_\alpha l_{0x} + s_\phi s_\alpha l_{0y} = 0 \tag{2.20}$$

leading to:

$$\tan\alpha = -l_{0x}/l_{0y} \tag{2.21}$$

Using Rodrigues Formula $e^{\widehat{\omega}\theta_i} = c_{\theta i} I + s_{\theta i}\,\widehat{\omega} + \overline{c_{\theta \iota}}\omega\omega^T$ and expanding equation (2.19) leads to

$$c_{\theta i}\boldsymbol{n}'^T \boldsymbol{l}_i + s_{\theta i}\boldsymbol{n}'^T \widehat{\boldsymbol{\omega}'} \boldsymbol{l}_i + \overline{c_{\theta \iota}}(\omega'^T \boldsymbol{l}_i)(\boldsymbol{n}'^T \boldsymbol{\omega}') = 0 \tag{2.22}$$

$$s_{\theta i}\boldsymbol{l}_i^T\widehat{\boldsymbol{n}}'\boldsymbol{\omega}' + \overline{c_{\theta\iota}}\boldsymbol{l}_i^T(\boldsymbol{n}'^T\boldsymbol{\omega}')\boldsymbol{\omega}' = -c_{\theta i}\boldsymbol{n}'^T\boldsymbol{l}_i = -c_{\theta i}s_\phi(c_\alpha l_{0x} + s_\alpha l_{0y}) \tag{2.23}$$

Since $s_{\theta i} = 2s_{\theta i/2}c_{\theta i/2}$ and $\overline{c_{\theta\iota}} = 1 - c_{\theta i} = 2s_{\theta i/2}^2$, divide both side of (2.23) by $2s_{\theta i/2}s_\phi$ and writing the equation in matrix form leads to:

$$\begin{bmatrix} c_{\theta i/2}l_{ix} & c_{\theta i/2}l_{iy} & s_{\theta i/2}l_{ix} & s_{\theta i/2}l_{iy} \\ & & & \\ & & & \end{bmatrix}\begin{bmatrix} (\widehat{\boldsymbol{n}}\boldsymbol{\omega}')_x/s_\phi \\ (\widehat{\boldsymbol{n}}\boldsymbol{\omega}')_y/s_\phi \\ (\boldsymbol{\omega}'^T\boldsymbol{n}')\omega_x/s_\phi \\ (\boldsymbol{\omega}'^T\boldsymbol{n}')\omega_y/s_\phi \end{bmatrix} = \begin{bmatrix} \dfrac{-c_{\theta i}}{2s_{\theta i/2}}(c_\alpha l_{ix} + s_\alpha l_{iy}) \\ \\ \\ \end{bmatrix} \tag{2.24}$$

With measurement at 4 or more different rotation angles θ_i, we can formulate the linear system $A\boldsymbol{x} = \boldsymbol{b}$ where:

$$A = \begin{bmatrix} c_{\theta 1/2}\boldsymbol{l}_1^T & s_{\theta 1/2}\boldsymbol{l}_1^T \\ \vdots & \vdots \\ c_{\theta n/2}\boldsymbol{l}_n^T & s_{\theta n/2}\boldsymbol{l}_n^T \end{bmatrix} \quad \boldsymbol{b} = \begin{bmatrix} \dfrac{-c_{\theta 1}}{2s_{\theta 1/2}}(c_\alpha l_{1x} + s_\alpha l_{1y}) & \cdots & \dfrac{-c_{\theta n}}{2s_{\theta n/2}}(c_\alpha l_{nx} + s_\alpha l_{ny}) \end{bmatrix} \tag{2.25}$$

$$\boldsymbol{x} = 1/s_\phi\begin{bmatrix}(\widehat{\boldsymbol{n}}\boldsymbol{\omega}')_x & (\widehat{\boldsymbol{n}}\boldsymbol{\omega}')_y & (\boldsymbol{\omega}'^T\boldsymbol{n}')\omega_x & (\boldsymbol{\omega}'^T\boldsymbol{n}')\omega_y\end{bmatrix}^T \tag{2.26}$$

and solve for $\boldsymbol{x} = [x_1 \quad x_2 \quad x_3 \quad x_4]^T$

Then, we can determine β by:

$$\frac{x_4}{x_3} = \frac{s_\phi(\boldsymbol{\omega}'^T\boldsymbol{n}')\omega_y}{s_\phi(\boldsymbol{\omega}'^T\boldsymbol{n}')\omega_x} = \tan\beta \tag{2.27}$$

With α and β known, to determine $\boldsymbol{\omega}'$ we need to identify ψ. For this, looking at x_1 and x_2

$$x_1 = \frac{(\widehat{\boldsymbol{n}}\boldsymbol{\omega}')_x}{s_\phi} = \frac{s_\phi s_\alpha c_\psi - c_\phi s_\psi s_\beta}{s_\phi} = s_\alpha c_\psi - \cot\phi\, s_\psi s_\beta \tag{2.28}$$

$$x_2 = \frac{(\widehat{\boldsymbol{n}}\boldsymbol{\omega}')_y}{s_\phi} = \frac{c_\phi s_\psi c_\beta - s_\phi c_\alpha c_\psi}{s_\phi} = \cot\phi\, s_\psi c_\beta - c_\alpha c_\psi \tag{2.29}$$

$$\tan\beta\, x_2 + x_1 = s_\alpha c_\psi - \tan\beta\, c_\alpha c_\psi = c_\psi(s_\alpha - \tan\beta\, c_\alpha) \tag{2.30}$$

From (2.30), we have:

$$c_\psi = \frac{\tan\beta\, x_2 + x_1}{s_\alpha - \tan\beta\, c_\alpha} \tag{2.31}$$

With this $\boldsymbol{\omega}' = \left[s_\psi c_\beta, s_\psi s_\beta, c_\psi\right]^T$ is determined.

Since the α and β from (2.21) and (2.27) are not unique, ψ is not unique and as a result, there are 4 possible $\boldsymbol{\omega}'$ depending on the combination of α, ψ and β, namely, $\boldsymbol{\omega}' = \left[\pm s_\psi c_\beta, \pm s_\psi s_\beta, c_\psi\right]^T$ and $\boldsymbol{\omega}' = \left[\pm s_\psi c_\beta, \pm s_\psi s_\beta, -c_\psi\right]^T$.

2.2.4 Translation Calibration

Once the orientation X has been calibrated, the translation $\vec{\mathrm{x}}$ can be easily calibrated from the same set of n images used for the calibration of image orientation. With the X known, the set of lines on the calibration rig plane, $\vec{\mathrm{L}}_\mathrm{i}$, are now known. The normal of the plane $\vec{\mathrm{n}}$ can be determined as a null space of the matrix $\left[\vec{\mathrm{L}}_0 \quad \vec{\mathrm{L}}_1 \quad \cdots \quad \vec{\mathrm{L}}_\mathrm{n}\right]$ by the singular value decomposition.

Then, the robot space position of any point ${}^{\mathrm{I}}\vec{\mathbf{p}}_\mathbf{i}$ selected on a line in the image is:

$${}^{R}\vec{\boldsymbol{p}}_i = R_i X\, {}^{I}\vec{\boldsymbol{p}}_i + R_i \vec{\boldsymbol{x}} + \vec{\boldsymbol{t}}_{\boldsymbol{i}} \tag{2.32}$$

Taking two such points for different joint angles (*i* and *j*)

$$\vec{\boldsymbol{n}}^T\left({}^{B}\vec{\boldsymbol{p}}_i - {}^{B}\vec{\boldsymbol{p}}_j\right) = 0 \tag{2.33}$$

Since both points belong to the rig plane. For n robot orientations the number of combinations of 2 points are C_2^n. These can be used to formulate an over determined linear system:

$$\begin{bmatrix} \vec{\boldsymbol{n}}^T\left(R_i - R_j\right) \\ \vdots \end{bmatrix} \vec{\boldsymbol{x}} = \begin{bmatrix} \vec{\boldsymbol{n}}^T\left(R_i X\, {}^{I}\vec{\boldsymbol{p}}_j - R_j X\, {}^{I}\vec{\boldsymbol{p}}_i + \vec{\boldsymbol{t}}_{\boldsymbol{j}} - \vec{\boldsymbol{t}}_{\boldsymbol{i}}\right) \\ \vdots \end{bmatrix} \tag{2.34}$$

which can be solved for $\vec{\boldsymbol{x}}$ by least squares.

2.2.5 Probe Calibration and Verification

Based on the method described above, the transrectal ultrasound probe mounted on the TRUS robot was calibrated and the calibration was verified by acquiring 3D ultrasound image of the string mockup with precisely known geometry.

Calibration

Figure 2.8(a) shows the probe calibration experimental setup with a UB10R-065U (Shimadzu Precision Instruments, Torrance, CA) TRUS probe supported by the 4-DoF TRUS robot and the plane rig submersed in the water tank. The plane rig is made of thin (0.53 mm) plastic sheet. The sheet was roughened with sand paper to increase the reflection of the ultrasound to the transceiver. Experimentally, this showed a clearer image of the plane [line, Figure 2.8(b)]. The ultrasound video signal was captured in a 720×576 resolution with 59/54 pixel aspect ratio.

To detect the line in the image, this is first eroded to sharpen the line, and pixels belonging to the line were detected by edge detection. A line was then fitted to the detected pixels [see Figure 2.8(c)] using the

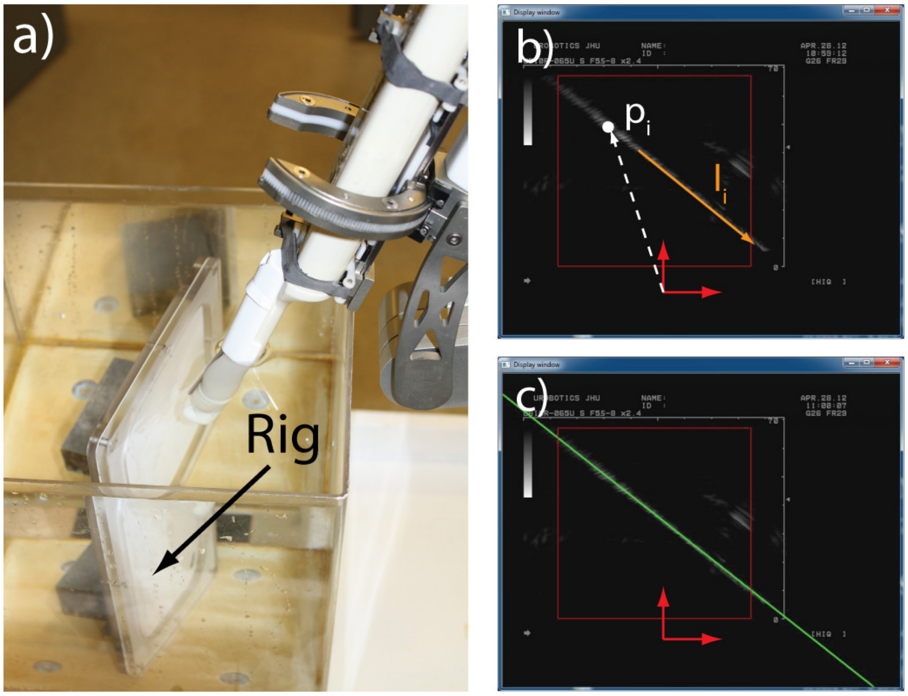

Figure 2.8: Probe calibration experiment
(a) Setup. (b) Image of the rig. (c) Detected line

RANSAC method. First the scales in both directions were calibrated as shown in Section II-C using two different depth settings and the image isocenter was determined from three robot orientations. The thickness of the imaged line is related to the beam thickness of the TRUS probe and its incidence angle to the rig plane and corresponding decrease in reflection. As the incidence angle increases (beam more parallel to the plane), the imaged line becomes wider and dimmer. In our case, the range of orientation was limited by a 20° incidence angle. For the rotation and offset calibrations, we have used a total of $n = 24$ robot orientations

Verification

The accuracy of the probe calibration was verified by imaging a string mockup of known geometry and comparing the acquired image with its CAD model. The mockup consists of six strings (made of Φ 0.36 mm fishing line) forming a 3 x 3 orthogonal grid with 20 mm x 20 mm spacing [see Figure 2.9 (a)]. The mockup was submersed in a water basin and the robot scanned the strings for 3-D imaging [see Figure 2.9 (b)]. The image was then segmented by thresholding and the strings were reconstructed into a surface [(see Fig. 5(c)]. The six strings defining the grid were fitted to the reconstructed surface and the locations of their nine intersection points were calculated. Then, the angles between all pairs of strings from the image and the CAD model (0° or 90°) were compared. Similarly, the distances between all pairs of intersection points were also compared. For both the angular and linear measures, accuracy was defined as the average of the differences, and precision as the corresponding standard deviations, as usual.

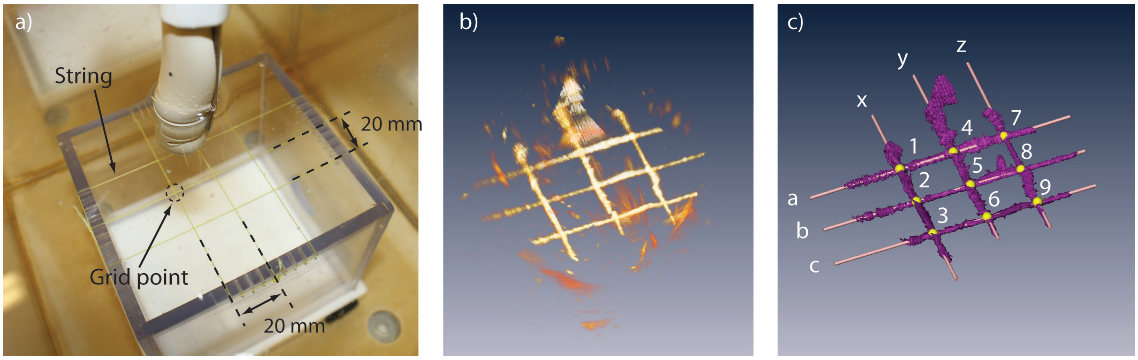

Figure 2.9: Probe calibration accuracy measurement.
a) Experiment setup b) 3D ultrasound image of the test mockup and c) Fitted string and intersection

The angles between the $C_2^6 = 15$ pairs of string measured from their images are compared with thier true value and tabulated in Table 4. The measured angles greed with their true value within 0.380° with a precision of 0.254°. The distance between the $C_2^9 = 36$ pairs of intersection points measured from their images is given in Table 5. The distances agreed with their true value within 0.33 mm with a precision of 0.21 mm. These show that the ultrasound scan follows closely the imaged environment, as shown in Figure 2.9 (c).

Table 4: Calibration accuracy - relative angles

Line Pair	**True Angle (°)**	**Measured angle (°)**	**| Difference (°) |**
x & a	90	90.584	0.584
x & b		89.8465	0.154
x & c		90.0299	0.030
y & a		90.4205	0.421
y & b		89.683	0.317
y & c		89.8664	0.134
z & a		90.8435	0.844
z & b		90.105	0.105
z & c		90.2872	0.287
x & y	0	0.1637	0.164
x & z		0.3837	0.384
y & z		0.5044	0.504
a & b		0.7631	0.763
a & c		0.7049	0.705
b & c		0.3018	0.302
Mean ± Std			0.380 ± 0.254
[Min, Max]			[0.030, 0.844]

Table 5: Calibration accuracy - relative distances

Point pair	True Distance (mm)	Measured Distance (mm)	| Difference|
1 2	20.000	19.828	0.172
1 3	40.000	39.507	0.493
1 4	20.000	20.627	0.627
1 5	28.284	28.691	0.406
1 6	44.721	44.610	0.111
1 7	40.000	40.235	0.235
1 8	44.721	44.819	0.098
1 9	56.569	56.245	0.323
2 3	20.000	19.679	0.321
2 4	28.284	28.757	0.472
2 5	20.000	20.683	0.683
2 6	28.284	28.583	0.298
2 7	44.721	45.036	0.314
2 8	40.000	40.141	0.141
2 9	44.721	44.618	0.104
3 4	44.721	44.754	0.032
3 5	28.284	28.511	0.227
3 6	20.000	20.739	0.739
3 7	56.569	56.674	0.106
3 8	44.721	44.658	0.063
3 9	40.000	40.053	0.053
4 5	20.000	20.094	0.094
4 6	40.000	39.707	0.293
4 7	20.000	19.608	0.392
4 8	28.284	28.049	0.236
4 9	44.721	44.197	0.524
5 6	20.000	19.613	0.387
5 7	28.284	28.178	0.107
5 8	20.000	19.458	0.542
5 9	28.284	27.560	0.725
6 7	44.721	44.412	0.309
6 8	28.284	27.551	0.733
6 9	20.000	19.314	0.686
7 8	20.000	20.345	0.345
7 9	40.000	39.898	0.102
8 9	20.000	19.553	0.447
Mean ± Std			0.332 ± 0.218
[Min, Max]			[0.032, 0.739]

2.2.6 Needle-guide Calibration

Once the probe is calibrated, the TRUS images are localized in the robot space. The robot may then scan a region of interest to collect image slice-position pairs. These may be used for 3D image reconstruction. Accordingly, the resulting 3D images are referenced relative to the robot coordinate space. To implement TRUS-guided needle targeting, an additional calibration of the needle-guide attached to the TRUS probe is needed.

Needle-guide calibration is a process of localizing the trajectory of the needle defined by the needle-guide with respect to the image coordinate and the robot coordinate system. This step is required to guide the needle based on the ultrasound image. In case of the TRUS probe, a needle-guide is commonly attached to the probe. While the location and direction of the needle-guide with respect to the probe is assumed to correspond to the CAD (Computer Aided Design) model, here, we also present an image-to-model calibration of the needle-guide using the calibrated 3D ultrasound.

The calibration consists of identifying the direction of the needle-guide (${}^{P}\vec{\boldsymbol{g}}$) and a position of its reference point (${}^{P}\vec{\boldsymbol{q}}$) (Figure 2.6).To calibrate the needle-guide the location of the inserted needle should be imaged. But when the needle is inserted the probe may not be moved to acquire its image, because this would also move the needle. As such, rather than imaging the needle itself, we implanted a marker segment through the needle and left it in place so that it can be imaged, as follows.

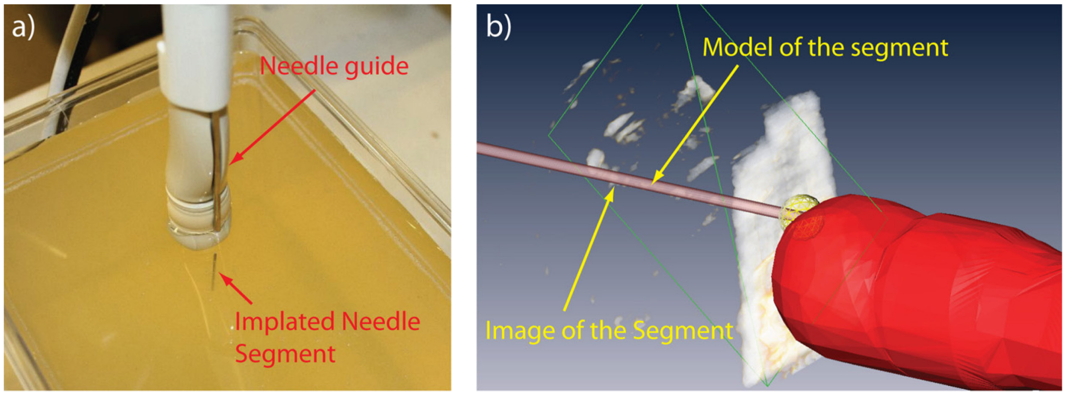

Figure 2.10: Needle-guide calibration showing
a) the needle segment implanted in the gelatin b) superimposed needle segment image and model

For this, the probe was instrumented with an 18Ga needle-guide and a calibration needle (18Ga x 200 mm trocar needle with symmetric, diamond point) was fully inserted into the gelatin through the guide. Then, a 25 mm long segment of an 18Ga stylet was implanted inside the gelatin through the trocar, in a similar way as it is done for brachytherapy seeds, by backing up the trocar while holding the stylet. Doing so leaves the implanted marker aligned along the direction ${}^{P}\vec{\boldsymbol{g}}$ of the needle-guide and the distal end at the location of the needle point ${}^{P}\vec{\boldsymbol{q}}$.

Scanning the implanted marker shows its 3-D ultrasound image (Figure 2.10a). Image-to-model registration between the image of the marker and the model of the needle gives the ${}^{R}\vec{\boldsymbol{g}}$ and ${}^{R}\vec{\boldsymbol{q}}$ needle calibration parameters. The location of the needle model may be calculated based on the position of the robot, as ${}^{P}\vec{\boldsymbol{g}} = F(\theta_i)^{-1}\,{}^{R}\vec{\boldsymbol{g}}$ and ${}^{P}\vec{\boldsymbol{q}} = F(\theta_i)^{-1}\,{}^{R}\vec{\boldsymbol{q}}$. The result show the needle model and marker image superimposed, as shown in Figure 2.10b. For other needle lengths, the point of the needle $\vec{\boldsymbol{q}}'$ can be calculated by an offset λ in the ${}^{R}\vec{\boldsymbol{g}}$ direction as $\vec{\boldsymbol{q}}' = \vec{\boldsymbol{q}} + \lambda\vec{\boldsymbol{g}}$, where λ is the length difference relative to the calibration needle.

2.2.7 Verification by Reverse and Direct Targeting Experiment

Validation of the image-guided targeting accuracy was performed in two experiments which we termed Direct and Reversed Targeting. Direct Targeting is an image-guided targeting accuracy experiment approach, where physical, visible targets are identified from the image and targeted. This is the common image-guided targeting approach that follows the natural workflow of image-guided interventions. A target visible in the image is aimed (“see then target”).

On the other hand, in Reversed Targeting the physical targets are not existent prior to targeting. Instead, these are digitally defined and marked by implanted markers. Their planned vs. actual locations are then compared by imaging. This is not a factual targeting, but rather a correlation of the digitally defined target and its actual image. In this approach markers are implanted at known locations and imaged thereafter (“target then see”).

Both targeting experiments methods give equivalent validation measures, but the Reversed may help in the development stages because the image-to-robot registration is not required prior to targeting. This enables image-based processing such as the calibration to be performed offline, after the images. These may be essential advantages when using CT or MRI (magnetic resonance imaging) guidance, which are less accessible. Moreover, the Reversed Targeting can also be done without a special mockup.

Method

For the reversed targeting experiment, the robot implanted 12 markers in a gelatin base (Figure 2.11a) at the target defined by different robot orientation (Table 6). The markers were made of angel hair spaghetti noodle (Φ 0.83 mm) cut in 3mm segments. The noodles were found to show lesser artifacts than metals in ultrasound (Figure 2.11b). The space of the implanted markers was then scanned in ultrasound. The location of the markers calculated from the forward kinematics (${}^{R}\vec{\mathbf{q}} = F(\theta)\ {}^{P}\vec{\mathbf{q}}$) and their imaged locations (${}^{R}\vec{\mathbf{p}} = F(\theta)\ {}^{P}_{I}G\ {}^{I}\vec{\mathbf{p}}_{\mathbf{i}}$) were compared. Accuracy was calculated as the average of the magnitude of differences between $\vec{\mathbf{p}}$ and $\vec{\mathbf{q}}$ ($|{}^{R}\vec{\mathbf{p}} - {}^{R}\vec{\mathbf{q}}|$) over all 12 markers, and precision was the corresponding standard deviation.

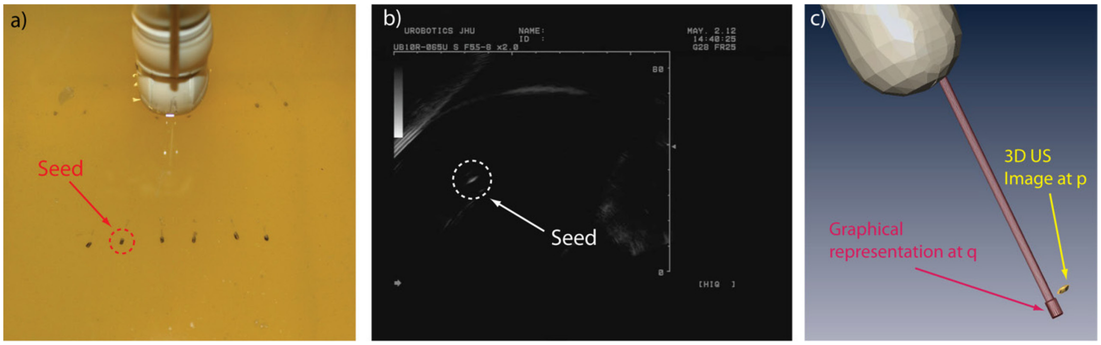

Figure 2.11: Reversed targeting accuracy measurement.
a) Experiment setup after implanting seeds b) Ultrasound image showing the implanted seed.
c) Location of ${}^{R}\vec{p}$ and ${}^{R}\vec{q}$

For the direct targeting experiment, a gelatin mockup with 6 hyperechoic inclusions (Figure 2.12a) was made and the center of the inclusions were targeted with the robot under ultrasound-guidance. Gelatin was used for the base material of the mockup. Cylindrical (Φ 4.8 x 8.3mm, volume 1.5mL, with rounded tip) inclusions were made of agar (Sigma-Aldrich St. Louis MO.), condensed milk, and glass microspheres (P2043SL, Cospheric LLC, Santa Barbara CA.) for higher echogenicity. Indeed, these inclusions are highly visible in ultrasound (Figure 2.12c), as described in (D'Souza et al., 2001).

The cavity of the mockup was filled with water to provide acoustic coupling (Figure 2.12b). A rotary scan (about the probe axis) was performed to acquire the 3D ultrasound image. Each inclusion was segmented by thresholding and reconstructed into a surface. The centroid of each inclusion was targeted with the needle point (Figure 2.12d). Since the 3D image is in robot coordinates, the joint angles were simply generated by inverse kinematics. To mark the location of the targeted needle, markers were implanted. These markers were Φ 0.72 x 5mm cylinders made of ceramic material. The ceramic was chosen for further imaging with Computed Tomography (CT), due to its high density relative to the surrounding gelatin.

The mockup was then scanned in CT. The accuracy of needle placement was defined as the average distance (norm of the error vector) between the center of the inclusion and the implanted seed, measured in CT.

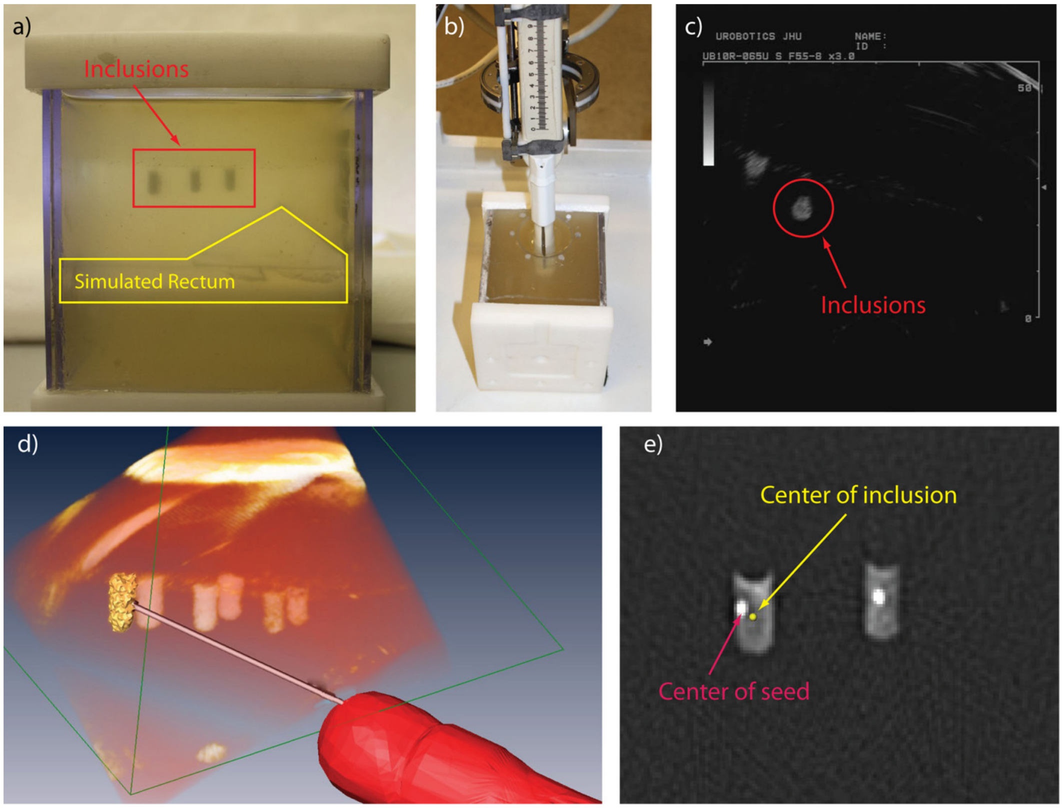

Figure 2.12: Direct targeting accuracy measurement.
a) Mockup b) Targeting setup c) 2D ultrasound image slice
d) 3D ultrasound images and e) CT image slice

Result

A graphic representation of the marker positions calculated from the forward kinematics ($\vec{\boldsymbol{q}}$) and its image ($\vec{p}$) is shown in Figure 2.11c. The reversed targeting accuracy, average magnitude of distance between p and q, was 2.36 mm with a precision of 0.937 mm. The X, Y, and Z error components in the robot coordinate system are included in Table 6.

Table 6: Reverse targeting accuracy results

Robot Orientation [°]			${}^{R}\vec{\boldsymbol{p}} - {}^{R}\vec{\boldsymbol{q}}$ [mm]			
Ry	Rx	Rz	**Δx**	**Δy**	**Δz**	**Norm**
-20	-15	-30	0.690	-0.296	-1.328	1.525
-20	-15	30	0.374	-0.463	0.866	1.051
0	-15	-30	0.045	-1.170	-1.457	1.869
0	-15	30	-0.906	-2.182	-1.711	2.917
20	-15	-30	-0.886	-0.021	-1.409	1.664
20	-15	30	-1.863	-1.756	-2.041	3.274
-20	15	-30	3.944	1.404	-1.355	4.400
-20	15	30	1.112	0.498	-1.895	2.253
0	15	-30	1.019	1.641	-1.889	2.702
0	15	30	-1.427	0.3585	-1.922	2.421
20	15	-30	0.260	1.848	-2.064	2.783
20	15	30	-0.572	0.372	-1.235	1.411
Mean (Accuracy)			0.149	0.019	-1.453	2.356
Std (Precision)			1.528	1.283	0.789	0.937

Direct targeting experiment was performed for 12 inclusions in 2 mockups. Figure 2.12e shows a CT image slice through one of the inclusions and its implanted marker. The direct targeting accuracy, indicating the overall robot-assisted ultrasound guided needle targeting accuracy, was 1.55 mm with a precision of 0.55 mm. Full result is given in Table 7.

Table 7: Direct targeting accuracy result

Mockup	Target #	Accuracy : Distance between the center of the inclusion and implanted seeds measured from CT image slice		
		Δx	**Δy**	**Norm**
1	1	-1.324	0	1.324
	2	-1.324	0.662	1.480
	3	-2.648	1.324	2.961
	4	-0.662	-1.324	1.480
	5	-0.993	0	0.993
	6	-1.324	0.993	1.655
2	1	-1.324	-1.655	2.120
	2	-1.324	-0.993	1.655
	3	0	-0.993	0.993
	4	0.331	-1.324	1.365
	5	-0.662	-1.324	1.480
	6	-0.993	0.331	1.047
Mean ± Std		-1.021 ± 0.753	-0.359 ± 1.032	1.546 ± 0.549
[Min, Max]		[-2.648, 0.331]	[-1.655 1.324]	[0.993 2.961]

Reversed and direct targeting results show 2.36mm and 1.55mm accuracy, respectively. The better result under CT was expected because of its superior measurement resolution and image quality. Since the experiments are equivalent, the 1.55mm accuracy reflects a closer estimate of the targeting performance.

Table 6 shows that the largest component of the reversed targeting error is in the Z coordinate direction (accuracy -1.453 mm). This was expected because the direction on which the markers were implanted has been close to the direction of the Z axis. The markers were seeds resembling that for brachytherapy, which are known to shift when exiting the trocar of the needle (seed "migration").

Overall, these validation experiments demonstrate that the calibration methods were accurate. For the prostate biopsy application, these results suggest that the overall TRUS Robot system may be sufficiently accurate to target clinically significant (0.5mL sphere, 5mm radius) PCa tumors. However, this study was performed in-vitro and under idealized conditions. Most importantly, the probe was carefully kept out of contact with the imaged objects by using water for acoustic coupling. While this was appropriate to validate the works, in a typical clinical setting coupling is achieved with ultrasound gel and the probe is pressed to maintain the contact, which can displace and deform the prostate. As such, the actual targeting will include additional error components that will have to be determined.

2.3 Software for Image-Guided Robot Control

Software of the image-guided robots serves as a human-machine interface between the robot and the physician. Therefore, it is important to design software that will integrate all the information from the robot and the image and display it in intuitive and familiar interface. The image-guided robot control software for TRUS 1 and 2 robots consist of two parts, robot control and image-guidance modules. The robot control software and the image-guidance software run on separate PCs, with the necessary data transferring over the TCP/IP connection. This separation of the robot control and visualization allows resource distribution and provides an additional layer of safety.

The scientific novelty of the research presented in this section is:

- A new algorithm for accelerating the 3D volume generation from the set of arbitrarily distributed image slices by partitioning the volume in octree and sorting the slices.

My personal contribution to this project was:

- Writing robot control software and image-guidance software with 3D ultrasound scanning capability

2.3.1 Robot Control Software

The main features of the robot control software are axis level motion control and a watchdog loop for safety. Axis level motor control is programmed by high-level libraries of the motion control card (MCI-SoftLib, PMDI). The low level motor control is implemented on an MC8000-DUAL (PMDI, Victoria, BC, Canada) motion control card with onboard digital signal processor for real-time motion control.

A software watchdog loop checks the state of several components of the system once every 100 ms and sends signal to the watchdog board if every state is normal. When an abnormal state is detected, the loop stops sending the signal to the board which in turn cuts the power to the robot when the signal is not received for longer than specified period of time.

2.3.2 Image-Guidance Software

The image-guidance software was programmed as a custom extension module of commercial visualization software Amira (Visage Imaging, San Diego, CA). Amira is visualization software developed by Visage Imaging, based on Open Inventor graphic library. The software provides modules for visualizing

2D and 3D image data and surfaces, by various rendering algorithms. It also offers developer pack which contains API for manipulating 3D image data and controlling visualization algorithms for creating custom modules.

The basic role of the image-guidance software is to visualize the robot and acquired ultrasound images in the robot space. Figure 2.13 shows the rendering window of the image guidance software. The position of the robot and image plane, and the captured ultrasound image slices are transferred over the network from the robot control software to the image-guidance software. Based on these received data, the model of the probe and the image slices are rendered in their corresponding position in the robot space.

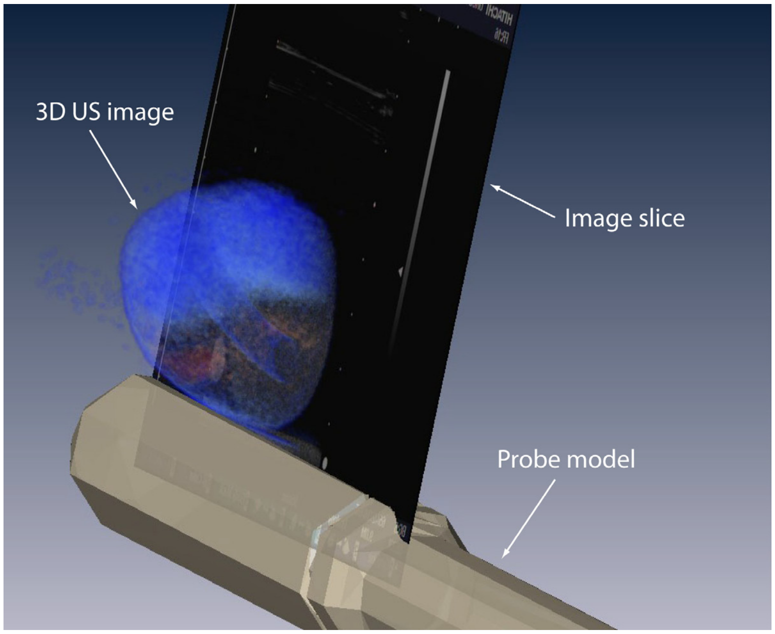

Figure 2.13: Image-guidance software

A major advantage of tracking the ultrasound is the reconstruction of 3D anatomy from the set of 2D images, which is typically done mnemonically by the physician. To do so, image-guidance software uses the position data and maps the pixels of the 2D ultrasound image slices to fill the 3D volume. As a result, the ultrasound probe can be manipulated to scan through the predefined volume and fill up the 3D volume image.

The algorithm for filling the 3D volumes from the sets of tracked 2D image slices was subject to many researches that are reviewed in (Solberg et al., 2007). These algorithms can be classified into two groups based on their principle, Pixel Nearest Neighbor (PNN) and Voxel Nearest Neighbor (VNN).

In PNN, the algorithm iterates through the each pixel in the acquired 2D image slices. The position of each pixel is calculated, index of the voxel in the 3D ultrasound image corresponding to the pixel is identified, and the pixel value is written to the voxel. This method allows slice by slice sequential processing and therefore is suitable for real-time population of the 3D image volume as the 2D image slices are acquired. However its drawback is that it can leave empty voxels.

In VNN, each voxel of the 3D ultrasound image is traversed and a voxel is updated to the value of the pixel that is closes to the voxel. This algorithm has advantages that it completely fills up the volume, but requires all the pixels of the acquired images to be searched and therefore not suitable for real-time update. The difference between the 3D ultrasound images generated by PNN and VNN can be seen in Figure 2.14.

Therefore, for the TRUS Robot, PNN is used to update the coarse 3D ultrasound image in real-time and VNN is used for post processing of the acquired 2D image slices to generate higher resolution 3D ultrasound image. One challenge with the implementation of the VNN algorithm is the time it takes to search the slice sets for the nearest pixel to each voxel.

Several algorithms have been proposed to accelerate the search process in VNN algorithm. In (Coupe et al., 2005), search space for each voxel is limited by using the probe trajectory under the assumption of continuous probe motion without any plane intersection. In (Wein et al., 2006), a fast slice selection algorithm that updates the limited search space as the voxels are traversed is presented and applied to create

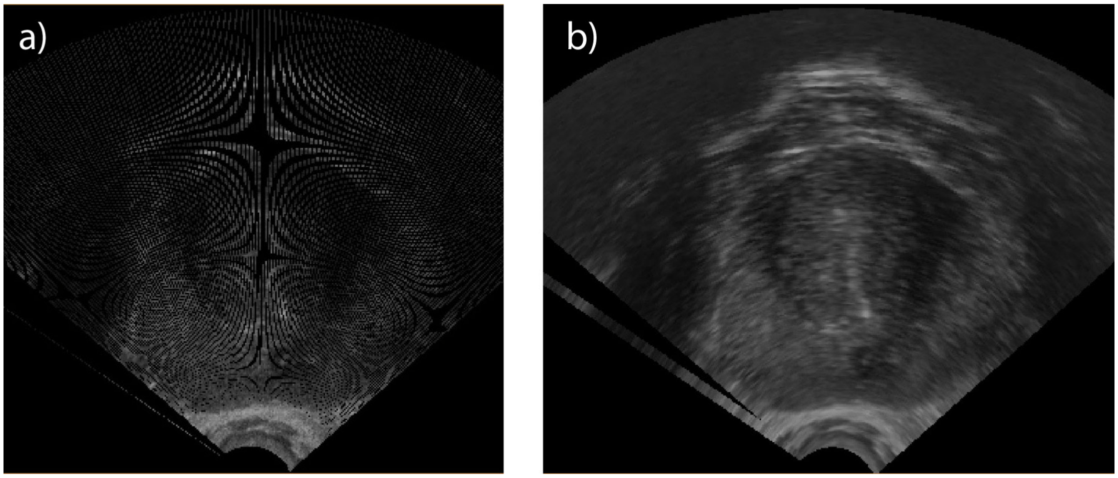

Figure 2.14: Cross section of the 3D US image filled up by
a) PNN and b) VNN from same set of image slices

multi-planar reconstruction directly from the image slices. In (Karamalis et al., 2009), GPU accelerated algorithm is presented. In this dissertation, I present a new algorithm for accelerating the search process by dividing the reconstruction volume into octree whose nodes maintain the list of the slices that intersects them, limiting the search spaces for each voxel.

Each slice is modeled as a box whose width and height corresponds to that of image plane and depth corresponding to 'thickness' of image plane. Then the volume is divided into octants, and number of slices passing through each octant is counted by checking intersection between the boxes of octant and image slice. The intersection between two arbitrarily oriented boxes in the space can be check by separating axes theorem. An octant is subdivided until specified level is reached or until the number of image planes intersecting the octants are less than specified. Then, when filling each voxel, only the slices that intersect the octant containing the voxel are searched. Figure 2.15 shows the 3D ultrasound image volume divided into octree and the search result of the nodes for a single image slice.

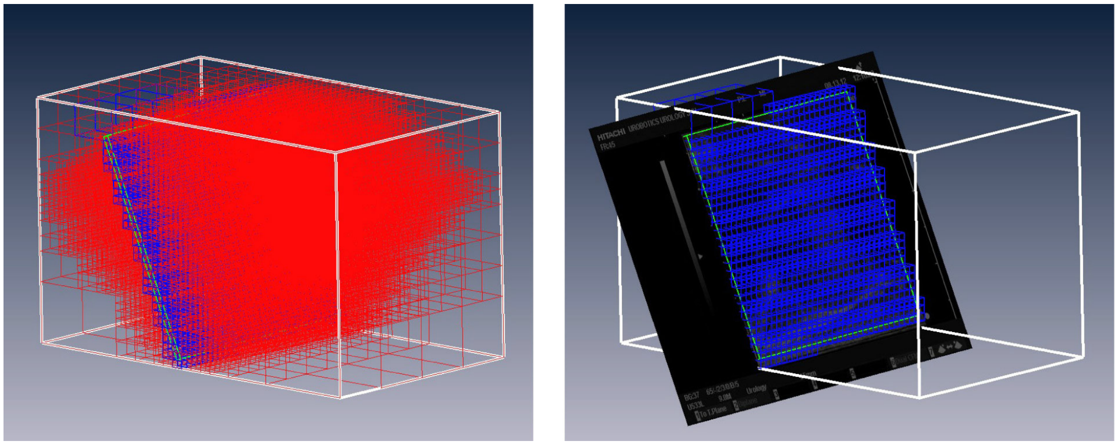

Figure 2.15: 3D ultrasound image volume (white) divided into octree (red) for fast search. Blue indicates the node that intersect with the image plane

2.4 Segmentation of the Prostate

Another role of the image-guidance software is to assist the planning of the intervention. Depending on the type of image intervention to be done, different planning software is required. However, one of the common tasks required for image-guided intervention of the prostate is the segmentation of the prostate from the ultrasound image.

Segmentation, which is a process of delineating the boundaries of the anatomy of interest from the medical image, has been topic of intense research in medical imaging. Segmentation of the ultrasound image is considered to be more challenging than the segmentation of other medical images due to the artifacts such as 'speckle' noise, attenuation and missing boundaries. Many segmentation algorithm for the ultrasound images were developed and reviewed in (Noble and Boukerroui, 2006).

An algorithm for segmenting 3D ultrasound image of the prostate acquired by TRUS robot was developed as part of mage-guidance software. The algorithm combines ideas from the existing algorithms that were used for the segmentation of prostate from 2D (Czerwinski et al., 1999, Abolmaesumi and Sirouspour, 2004a, Abolmaesumi and Sirouspour, 2004b) and 3D (Wang et al., 2003) TRUS images.

As it was done in (Wang et al., 2003), the 3D ultrasound image of the prostate is resliced along the plane of appropriate orientation that emphasizes the boundary to be segmented. Then, the set of resliced 2D images are enhanced by a Sticks filter (Czerwinski et al., 1999) and segmented by an edge-tracking algorithm similar to the one used in (Abolmaesumi and Sirouspour, 2004a, Abolmaesumi and Sirouspour, 2004b), which has been modified to utilize the segmentation result of the adjacent slices.

The scientific <u>novelty</u> claimed in this section is

- A new algorithm for segmenting the 3D ultrasound image of the prostate by combining the previous arts of using non-orthogonal reslicing and probabilistic edge tracking method, cited above.

My personal <u>contribution</u> to this project was:

- Writing software for the segmentation

2.4.1 Algorithm

In many previous 3D prostate segmentation algorithms, the image is resliced into multiple 2D cross sections and each slice is segmented and combined into the final result. In most of cases, the direction of

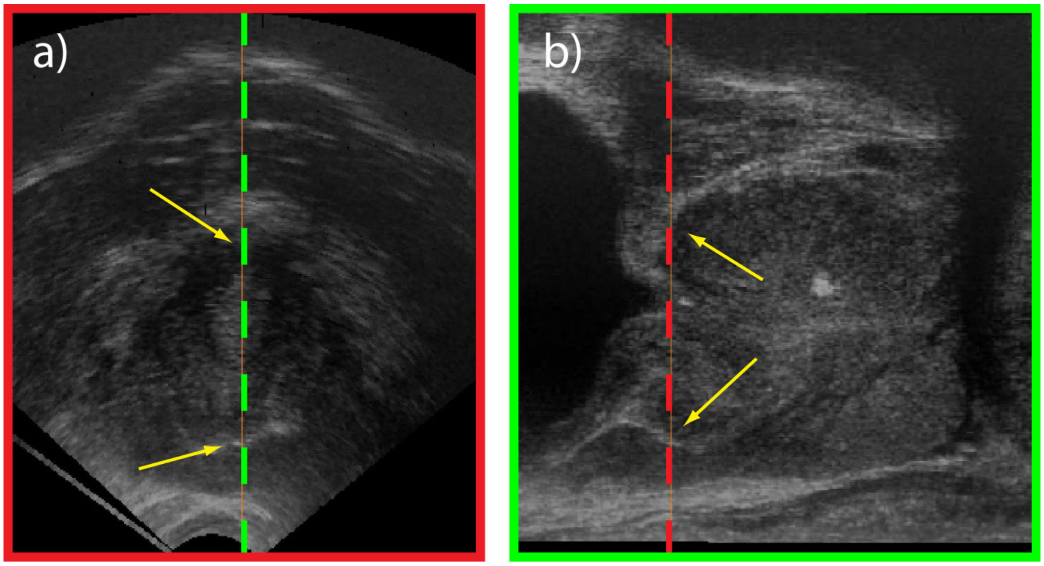

Figure 2.16: Visibility of prostate boundary depends on reslicing plane orientation
a) Transverse cross section of the prostate through the base of the prostate, red line in b)
b) Sagittal cross section of the prostate, the boundary at the base region is more visible than in a)

the reslicing plane was kept constant, usually being the transverse cross section. However, the visibility of the prostate boundary depends on the orientation of reslicing plane. For example, as shown in Figure 2.16, the boundary of the prostate at the base and apex region is not easily identifiable in the transverse section of the prostate. These, however, are more clearly visible in sagittal cross sections. In some algorithms, a statistical model based on training dataset has been used to overcome the problem of poor visibility.

In our segmentation algorithm, 3D image is resliced along a plane that emphasizes the boundary to be segmented, depending on the region of the prostate to be segmented. A transverse cross section is used for the segmentation of the mid-gland region and sagittal and coronal cross sections are used at the base and apex regions. These lead to easier segmentation at the apex and base region without relying on a pre-acquired training dataset. A similar approach has been taken in (Wang et al., 2003).

Resliced 2D images are then enhanced by Sticks filter before segmentation. Sticks filter, developed by (Czerwinski et al., 1998) and used in 2D TRUS image first in (Pathak et al., 2000), is a filter that enhances thin bright feature in the ultrasound image. The boundary of the prostate with surrounding organ is characterized by such feature. The response to the Sticks filter for a pixel at (u, v) is defined as a maximum of the responses to a set of N kernels of radius r. Each ith kernel of the set is defined by their angle $\theta_i = \frac{\pi i}{N}$

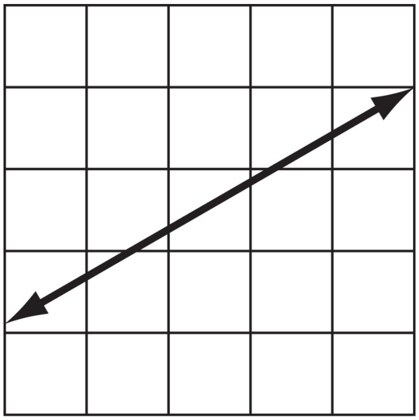

0	0	0	0	0
0	0	0.0134	0.1402	0.1464
0	0.0866	0.2268	0.0866	0
0.1464	0.1402	0.0134	0	0
0	0	0	0	0

Figure 2.17: Example of Stick Filter Kernel

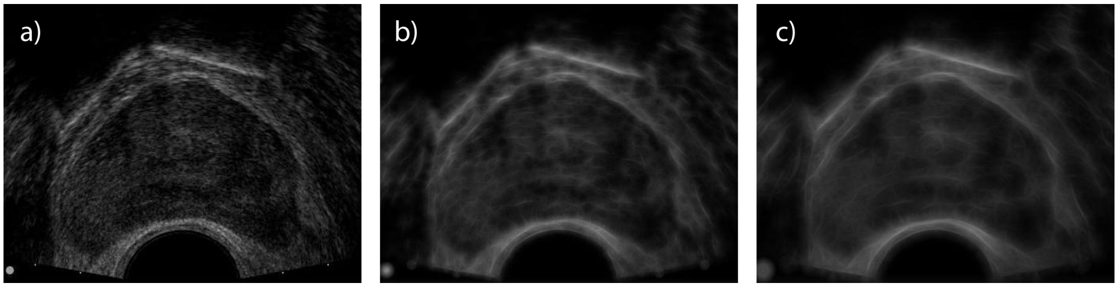

Figure 2.18: Stick Filter applied to ultrasound image, in plane
a) original, b) r = 6, c) r = 12

and when applied to a pixel at (u, v), the kernel averages the pixels in along the line $l_i = [\cos\theta_i \sin\theta_i]$ centered at (u, v). An example of the kernel with $r = 2$ and $\theta = 30°$ is shown in Figure 2.17. According to (Czerwinski et al., 1998), the angle θ_i corresponding to the maximum response is the most likely direction of the edge at that pixel, under the assumption of Gaussian noises in the image.

Figure 2.18 shows the Sticks filter applied to a single ultrasound image. It can be seen that the larger the filter radius, more enhancement is achieved, but hairy artifacts are also increased as well. However, for 3D images, these artifacts can be avoided while still enhancing the images by applying a filter and reslicing the images in mutually perpendicular direction. By doing so, edge enhanced images with minimal artifact can be achieved as shown in Figure 2.19. For our application, as the prostate will be resliced in transverse and coronal plane for segmentation, Sticks filter was applied in sagittal plane which is perpendicular to both of the planes.

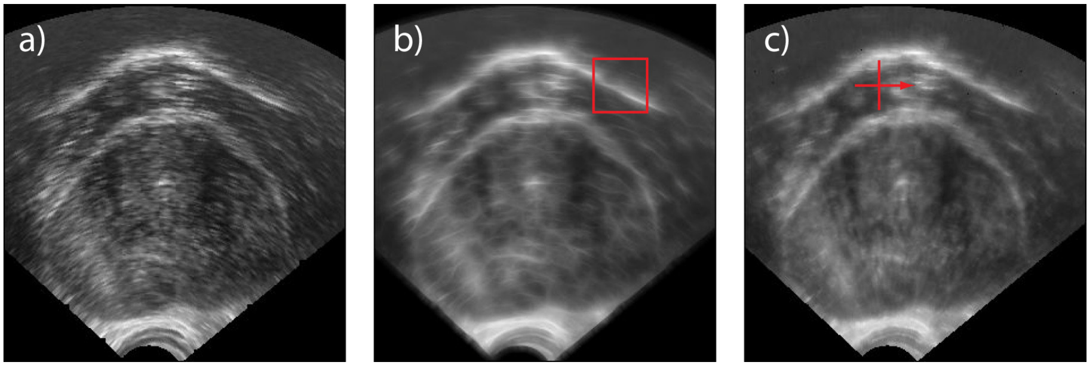

Figure 2.19: Effect of the stick filter application direction
a) original image, filter applied in b) in plane and c) out of plane

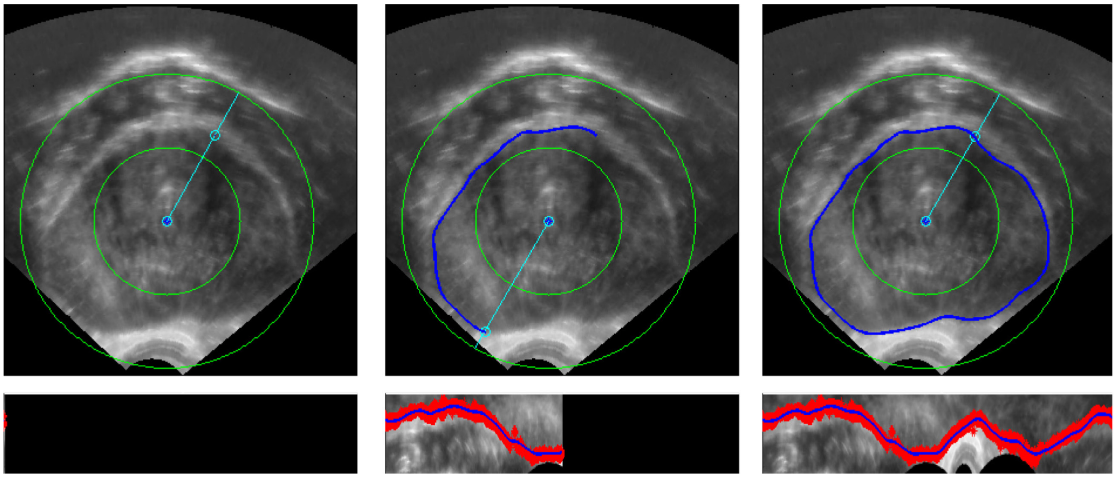

Figure 2.20: Segmentation of enhanced slice by PDAF

The enhanced image slice is segmented. Several algorithms have been developed for the segmentation of the prostate from 2D image slices. Our segmentation algorithm is based on the 'Star-Kalman' filter algorithm, which is used to segment a closed contour from the ultrasound image (Abolmaesumi et al., 2002). In this algorithm, the boundary of the closed contour is segmented by 'measuring' its edge points along the radial direction and 'tracking' it as the radial line spins and sweeps across the image. (Figure 2.20) This 'measurement' and 'tracking' process is performed by using the Probabilistic Data Association Filter (PDAF), technology for estimation and tracking in temporal domain using the multiple detected data from the radar tracking and used in contour tracking for the segmentation in (Abolmaesumi and Sirouspour, 2004a). These previous developments are extended for 3D ultrasound image segmentation by incorporating the model from the segmentation result of the adjacent image slice into PDAF.

The segmentation algorithm is initialized by selecting a center point inside the closed loop boundary and drawing a ray from the center to the initial point on the boundary. Then the contour can be parameterized in polar coordinates $d(\theta)$, where d is the distance to the boundary from the center point along the ray at angle θ. Starting from this initial point at $[d_o, \theta_o]$, the ray is rotated by angle $\Delta\theta$ to θ_1, and the new location of the edge d_1 is calculated by combining the 'prediction' based on the model of the contour and the 'measurement' by the edge detection along the ray. Since the ultrasound image is influenced by speckle noise, resulting multiple edge detected along the ray, the 'prediction' and the 'measurement' is combined by using PDAF.

The initial model of the contour is a circle with constant radius with noisy variation in the radius. In discrete form, it is:

$$d_{t+1} = d_t + w_k \tag{2.35}$$

where $w_k$is a normal distributed noise zero mean and covariance P_k. However, once a single slice has been segmented, this segmentation can be used as an input to the contour model used for the segmentation of the adjacent slice, In discrete form, it is:

$$d_{t+1} = u_t + w_k \tag{2.36}$$

where the input u_t is derivative of the previous contour $u_t = \frac{du}{d\theta}$

With the model defined, PDAF update process is performed as follows. First, given the distance to the boundary $d(k-1|k-1)$, the distance to the boundary at next angular step is predicted by the model described above, and variance is updated

$$d(k|k-1) = d(k-1|k-1) \tag{2.37}$$

$$P(k|k-1) = P(k-1|k-1) + Q(k) \tag{2.38}$$

Then based on predicted distance, predicted measurement and its covariance are updated.

$$z_o = d(k|k-1) \tag{2.39}$$

$$S_k = P(k|k-1) + R_k \tag{2.40}$$

The measurement - edge detection along the radial line - is done by sampling the image along the radial and filtering the sampled line by modified derivative kernel:

$$\frac{(x_{k+2} + x_{k+1} + x_k) - (x_{k-1} + x_{k-2} + x_{k-3})}{3} \tag{2.41}$$

The location of maximum 6 values of the derivative was selected as a measurements z_i. From these multiple measurements z_i, a single measurement $z(k)$ is calculated by averaging each measurement z_i by their likelihood β_i in following manner:

$$z(k) = \frac{\sum_i \beta_i z_i}{\sum_i \beta_i} \tag{2.42}$$

$$\beta_0 = 1 - P_d \quad \beta_i = \frac{1}{\sqrt{2\pi S_k}} \exp(z_i - z_o)^T S_k^{-1} (z_i - z_o) * \frac{P_d}{N} \tag{2.43}$$

This gives minimal squared error estimate of the measurement under assumptions and variance corresponding to this estimation is:

$$\tilde{P} = \sum_i \beta_i (z_i - z_o)(z_i - z_o)^T - \left(\sum_i \beta_i (z_i - z_o)\right)\left(\sum_i \beta_i (z_i - z_o)\right)^T \tag{2.44}$$

Finally, the prediction is corrected by measurement in a similar way as in Kalman filter. The update of the variance includes the contribution of the usual Kalman filter variance update and also from the variance $\tilde{P}$ associated with the measurement association uncertainty.

$$d(k|k) = d(k|k-1) + K_k e_k \tag{2.45}$$

$$K_k = P(k|k-1) S_k^{-1} \tag{2.46}$$

$$P(k|k) = \beta_0 P(k-1|k-1) + (1-\beta_0)(I - K_k) P(k|k-1) + K_k \tilde{P} K_k^T \tag{2.47}$$

This process is illustrated in Figure 2.21 below.

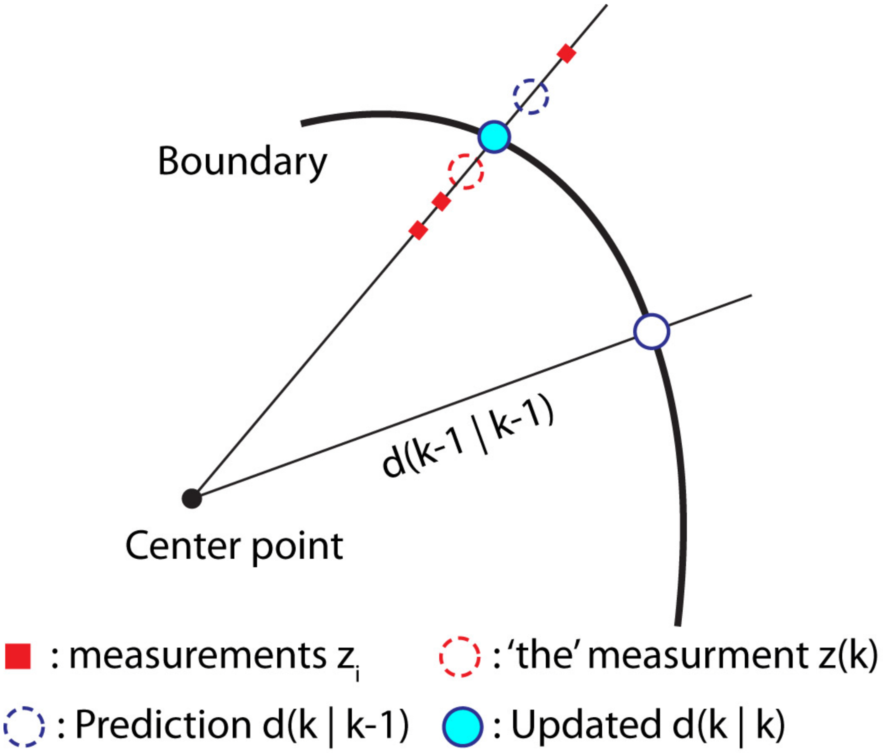

Figure 2.21: PDAF update process (Abolmaesumi and Sirouspour, 2004a)

2.4.2 Results

The segmentation algorithm was initially applied to one of the 3D ultrasound images of prostate acquired during the clinical trials of Tandem Robot assisted Radical Laparoscopic Prostatectomy (T-RALP). A 3D volume image was generated from 294 image slices acquired while rotating TRUS probe about its axis as shown in Figure 2.22a. The Sticks filter was applied in sagittal (YZ plane) direction (Figure 2.22c), resulting in enhanced images with minimum artifact when resliced about XY plane as shown in Figure 2.22b.

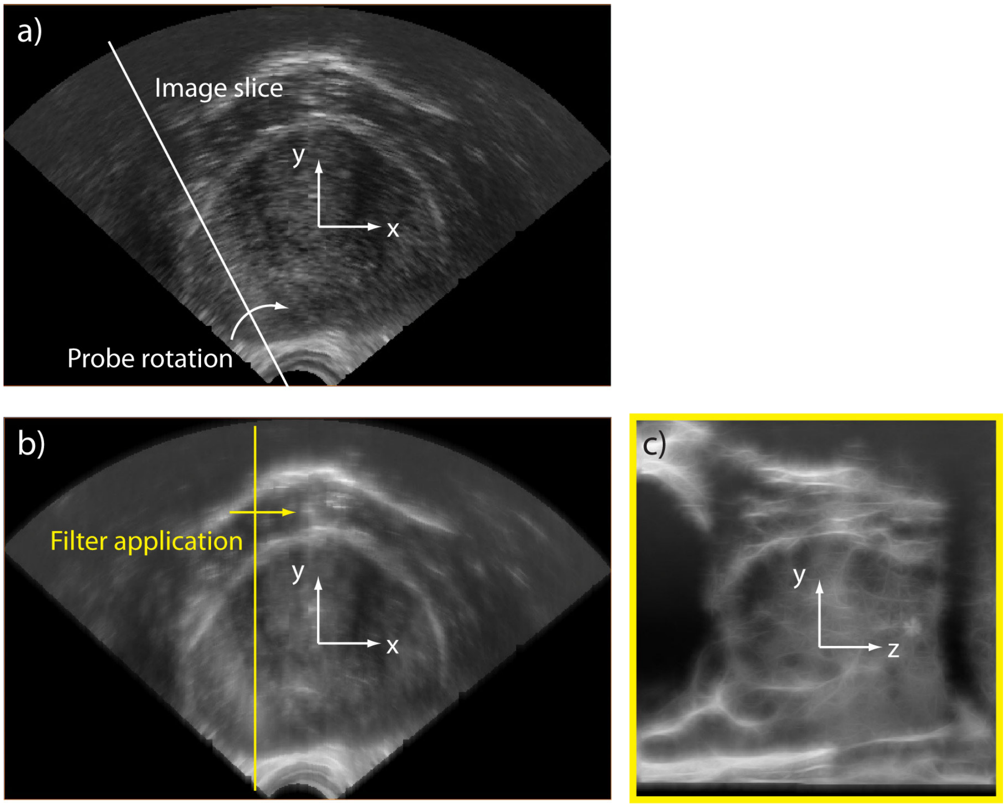

Figure 2.22: Enhancement of the TRUS image
a) XY plane cross section of the 3D US image of the prostate generated from rotary scan,
b) The image enhanced by applying Sticks filter in YZ plane and c) image slice from the YZ plane

Central transverse (XY plane) cross section images of the prostate with highly visible boundary were selected as a initial slice for the segmentation and segmented as shown in Figure 2.23. Then the reslicing plane is rotated about the X axis with a 3 degree increment and each resliced image is segmented by using the segmentation result of the previous reslice as an input. This results in gradually building up of the 3D structure by each set of segmented contours as shown in Figure 2.24.

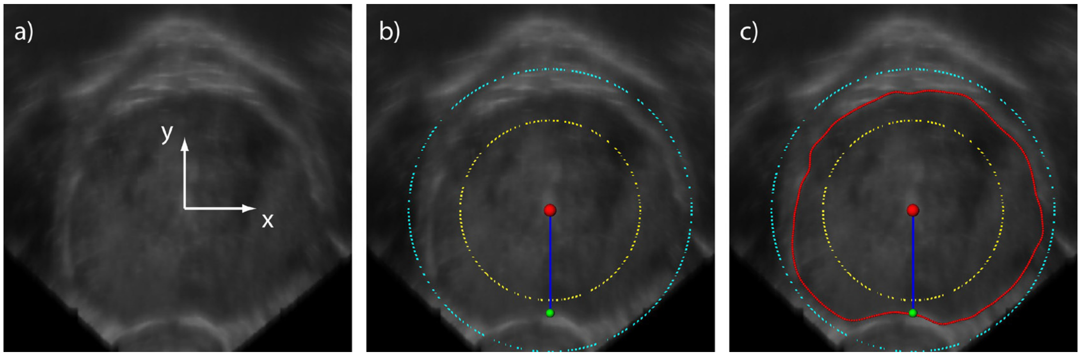

Figure 2.23: Segmentation of the initial slice.
a) Image slice in XY plane, b) Range settings for edge tracking and c) Resulting tracked edge

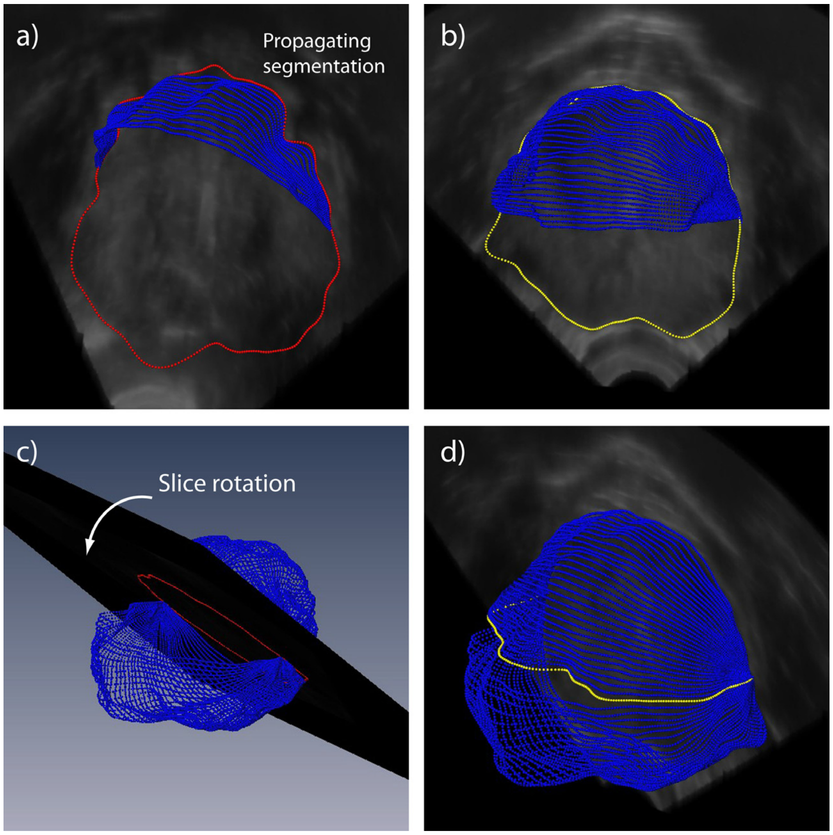

Figure 2.24: 3D segmentation by propagating segmentation through the rotating reslice plane

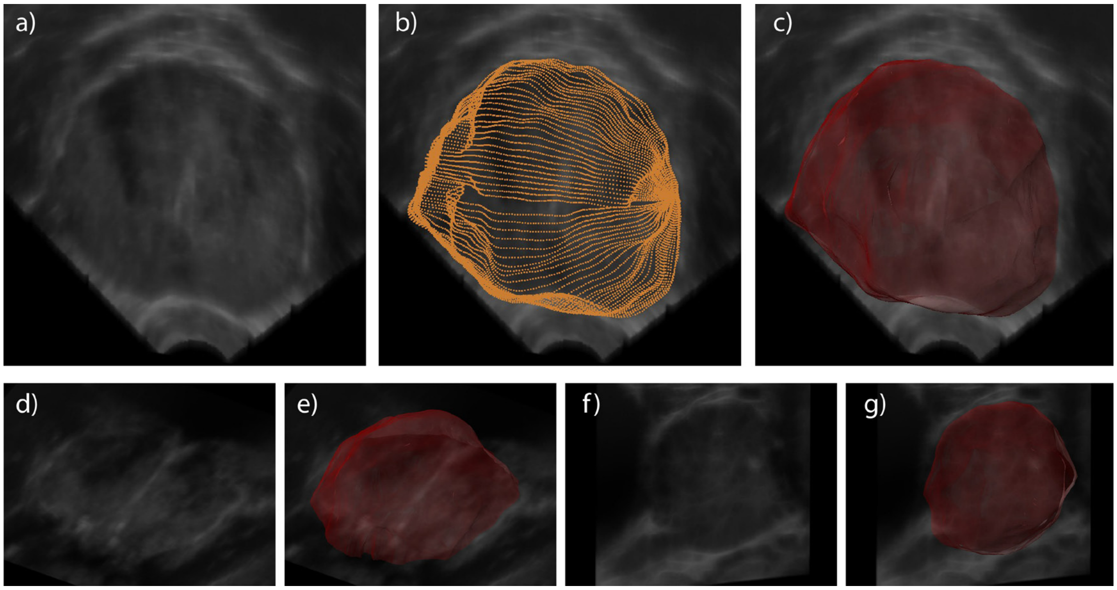

Figure 2.25: 3D reconstruction of the prostate from the segmented contours
a) Transverse slice, b) Set of segmented contours.
3D reconstructed surface overlaid on c) Transverse, d & e) Coronal, and f & g) Sagittal image

Finally, a 3D surface reconstruction of the prostate is generated from the set of points of the segmented contours. Figure 2.25 shows the 3D reconstruction of the prostate and the image slices. It can be seen that the segmentation closely follows the boundary in the image slices with some limitations in the apex and base region of the prostate where the boundary is not prominent in the original image.

This segmentation algorithm may be further evaluated on additional 3D TRUS images and compared with the manual segmentation by urologist.

3 Applications of the Ultrasound Image-Guided Robot

Using robotics in image-guided intervention may bring computer controlled precision and reliability to the procedure. In addition, the robot serves as a platform for integrating the information, and provides physicians with richer information. Likewise, the TRUS robot provides precise and steady handling of the ultrasound probe and the needle-guide, and also combines the 2D ultrasound images to generate 3D reconstruction of the anatomy. Many potential image-guided intervention procedures using the TRUS robot system were devised and their feasibility was tested through in-vitro experiments and clinical trials. The following section describes these tests, procedures, and their results.

3.1 Tandem Robot Assisted Radical Laparoscopic Prostatectomy

The first application of the TRUS robot was Tandem Robot Assisted Radical Laparoscopic Prostatectomy (T-RALP). T-RALP is a Robot Assisted Laparoscopic Prostatectomy (RALP), in which the TRUS robot is used in tandem with the daVinci surgical robot (Intuitive Surgical Inc. Sunnyvale, CA) to provide intraoperative guidance and visualize Neurovascular Bundle (NVB) during the surgery.

3.1.1 Radical Prostatectomy and Intraoperative Guidance

Radical prostatectomy (RP) is a procedure for treating prostate cancer by resecting the prostate gland containing cancer. In radical prostatectomy, preservation of NVB around the prostate is important for preventing tumor recurrence and preserving sexual potency following radical prostatectomy (Walsh et al., 1983). However, visualizing NVB during surgery can be challenging due to the periprostatic connective tissues and intraoperative hemorrhage.

Intraoperative TRUS imaging during RP may help visualizing the NVB and guiding the surgery. The blood flow through NVB can be visualized with the Doppler ultrasound and the tips of the surgery tools appear as a hyperechoic lesions under B-mode ultrasound. This idea was initially tested in (Gill and Ukimura, 2007), where the human assistant manipulated TRUS during Laparoscopic Radical Prostatectomy (LRP) without robot assistance. The authors reported that the TRUS images guidance can potentially provide a decreased rate of positive surgical margins and improve the dissection of the NVB.

However, in RALP, which is more commonly performed than LRP, there is not enough space between the daVinci robot and the patient for a human assistant. Therefore, in T-RALP, TRUS robot was used to manipulate the probe in place of human assistant and provide intraoperative guidance. The use of TRUS robot allows more stable manipulation of the probe and acquisition of ultrasound images with the positional data for additional analysis.

Table 8 below compares previous research on intraoperative ultrasound guidance of radical prostatectomy. Our clinical trial of the T-RALP (Han et al., 2011), stands as the first research to use a robot manipulated TRUS probe to provide intraoperative ultrasound image guidance during radical prostatectomy and showed the feasibility of the approach.

Table 8: Previous publications on intraoperative ultrasound guided prostatectomy

Reference	TRUS Probe Manipulation	Procedure	Achievement
(Gill and Ukimura, 2007)	Human assistant	LRP.	First trial of intraoperative guidance in radical prostatectomy
(Han et al., 2011)	TRUS2 Robot	RALP	First using robot manipulated TRUS probe.
(Hung et al., 2012)	Commercial endoscope manipulator (ViKY)	RALP	
(Adebar et al., 2012, Mohareri et al., 2013).	Robot based on a brachytherapy stepper	RALP	daVinci tool registered to the TRUS image and tracked by the robot.

The scientific novelty of the research presented in this section is:

- The first clinical trial of the TRUS image-guided RALP using the robotic ultrasound, verifying the feasibility of the approach.

This has been reported in a journal article (Han et al., 2011). Among the authors, Dr. Misop Han was the surgeon performing the prostatectomy and my personal contribution to this project was:

- Write the software for acquisition of the robot position and ultrasound image data
- Participate in the clinical trials as a robot operator and acquire data

3.1.2 T-RALP: Procedure and Results

In T-RALP, TRUS robot is installed between the patient's legs and the daVinci robot as shown in Figure 3.1. TRUS robot is mounted on the surgery table and the TRUS probe is placed in the patient prior to docking the daVinci robot. The video output from the ultrasound scanner is fed into surgeon's console and can be displayed simultaneously with the laparoscopic camera view on the console by using the 'TilePro' function of the daVinci robot. This allows the surgeon to see the TRUS image while operating. During the surgery, the TRUS robot manipulates the probe to examine the prostate and capture the TRUS images for further analysis.

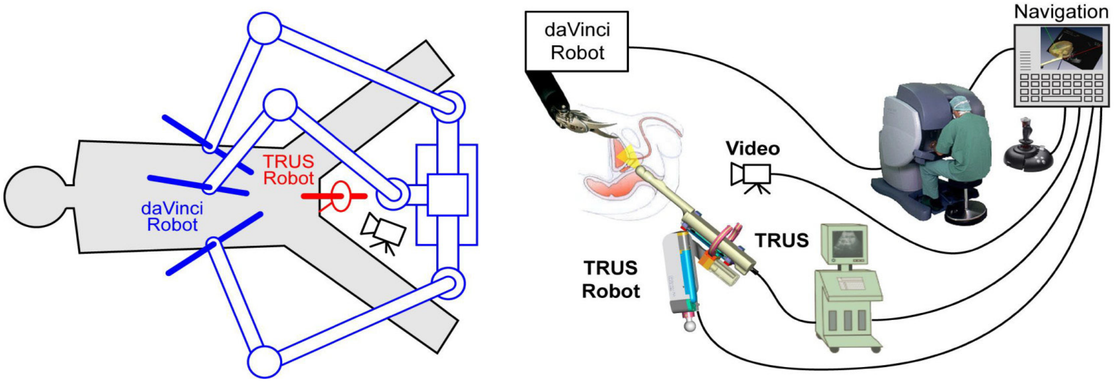

Figure 3.1: T-RALP Setup

After feasibility study on 3 subjects, 55 clinical trial of T-RALP was performed. At each case, image data were acquired for further analysis. At the beginning of the surgery, prostate was 'scanned' by rotating the probe while capturing the sagittal image slices. The collected image and position data was used to generate 3D ultrasound image after the surgery and also segmented to create 3D reconstruction of the prostate as shown in Figure 3.2. During the surgery, the NVB and surgical tool tip was identifiable from the image as shown in Figure 3.3. The distance between the prostate boundary and the NVB was measured for 31 patients. The average distance between the prostate and the NVB on right side and the left side of the prostate was 2.72 and 2.96 mm respectively. After the surgery, Doppler ultrasound was used to confirm the preservation of the NVB.

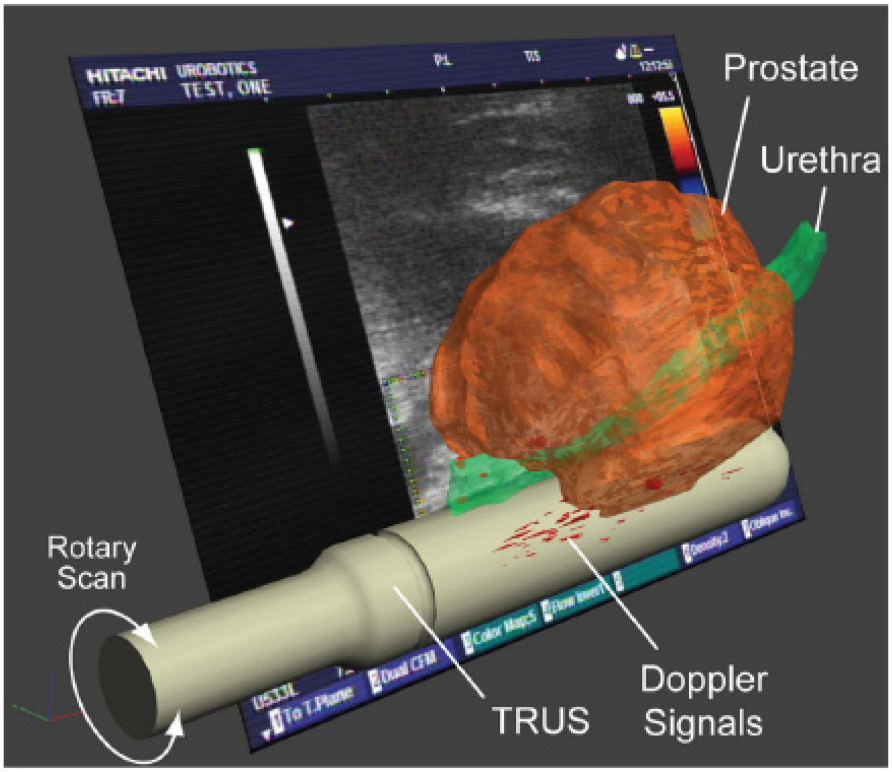

Figure 3.2: 3D reconstruction of the prostate and NVB from preoperative scan

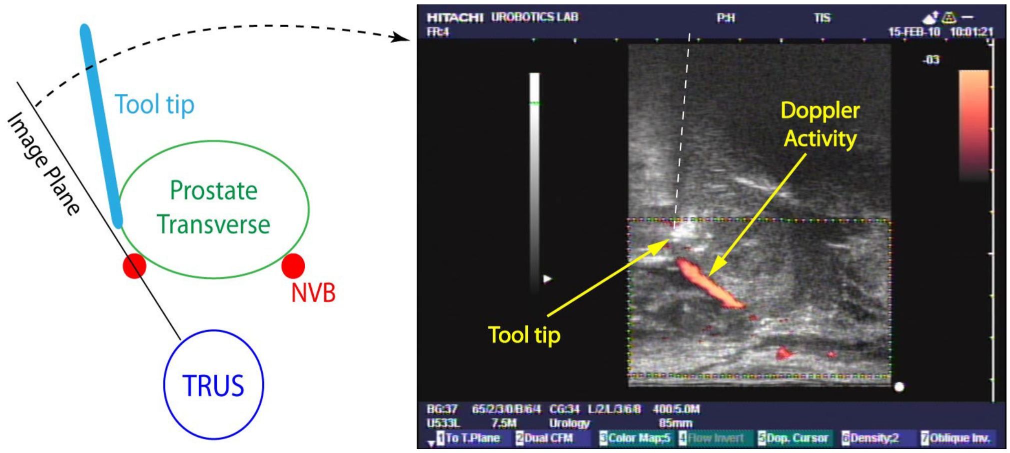

Figure 3.3: Doppler ultrasound image of the prostate
a) before b) during c) after the operation

3.2 Robot Assisted TRUS Guided Transrectal Prostate Biopsy

One of the primary ultrasound image-guided interventions in urology is prostate biopsy. Usually, prostate is sampled under the guidance of TRUS image by transrectally delivered biopsy needle (Figure 3.4a). As the prostate cancer is not visible in ordinary B-mode ultrasound image, the goal of standard TRUS guided transrectal prostate biopsy is to uniformly sample the prostate according to the 'systematic sextant' plan as shown in Figure 3.4b. The urologist performing the biopsy will try to achieve this goal while manipulating the probe and the biopsy needle, and at the same time, mnemonically reconstructing the 3D anatomy of the prostate from the series of observed 2D image slices. This is very challenging hand-eye coordination task that can be assisted with the stability and precision of the robotic probe manipulation and 3D ultrasound imaging. Under this idea, an experiment comparing the accuracy of the systematic TRUS guided transrectal prostate biopsy by human and by TRUS robot was performed, and the result was reported in (Han et al., 2012).

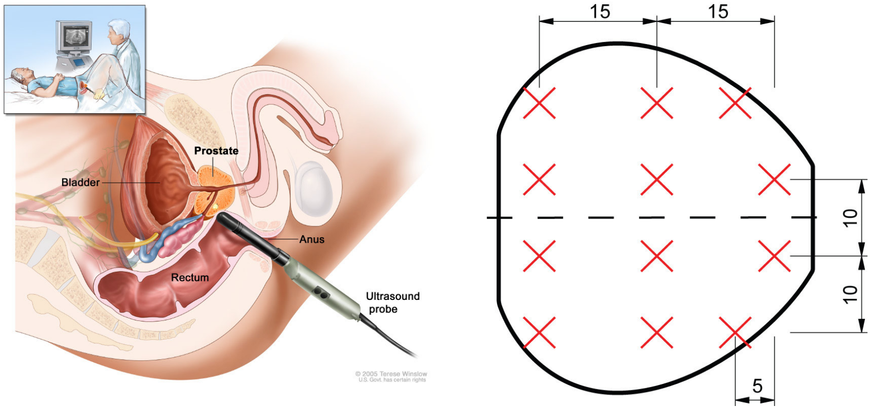

Figure 3.4: Transrectal prostate biopsy and sextant plan

The scientific <u>novelty</u> of the research presented in this section is:

- In-vitro experiment setup for measuring the accuracy and repeatability of the systematic biopsy by human and robot assistance.
- A system for robot assisted TRUS-guided systematic biopsy demonstrating improved accuracy and repeatability over the manual biopsy in in-vitro experiment.

This has been reported in a journal article (Han et al., 2012). Among the authors, Doyoung Chang and Hyungjoo Kim designed the experiment setup and ran the human biopsy experiments. My personal contribution to this project was:

- Write the software for 3D image-guided biopsy of the prostate
- Ran the robot biopsy experiment.

3.2.1 Accuracy Measurement of Human vs. Robot Biopsy

For this experiment, a biopsy simulation system with pelvic mockups and a Polaris® optical tracking system (Northern Digital Inc. Ontario, Canada) was developed as shown in Figure 3.5. The pelvic mockup included a 24 cm^3 model prostate fabricated from gelatin and a cavity simulating the rectum. Gold standard biopsy targets were defined on the model prostate as 12 points arranged as usual in an extended sextant biopsy schema (Figure 3.4b).

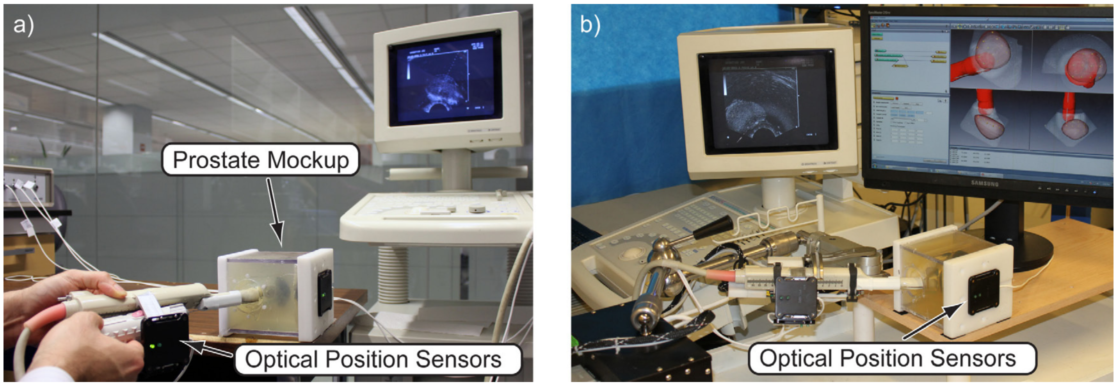

Figure 3.5: Biopsy simulation system with prostate mockup and optical tracking system
The system is used for measuring accuracy of 12 core sextant biopsy by a) Human and b) Robot

The optical tracking system was configured to estimate the locations of the actual biopsy cores. One active optical tracking marker (M1) was assembled on the mockup box. Since the mockup was molded with precisely defined geometry to standardize the model prostate position and configuration in the box, the locations ${}^{M1}\vec{t}$ of the gold standard targets with respect to the coordinate system of the marker M1 are known from the design of the mockup. Moreover, these are the same for all the mockups that were identically built.

Two active markers (M2 and 3) were placed on the TRUS probe handle to measure its location and orientation. They were attached facing opposite sides so that at least one of them will be always visible to the camera of the tracking system throughout the biopsy procedure. For needle-guide calibration, a straight needle with two passive markers attached was inserted through the guide. Then the equation of the line $\vec{\boldsymbol{q}} + \lambda\vec{\boldsymbol{l}}$ defining the needle-guide with respect to the coordinate system of the marker M2 and M3 was identified as a line passing through the two passive markers.

One passive marker (M4) was placed on the biopsy needle shaft with known distance d_0 from the tip of the needle to measure the needle insertion depth. When the mockup is biopsied using the needle passing through the needle-guide attached to the TRUS probe, the configuration of the active markers' coordinate system ${}^{O}_{M1}G$, ${}^{O}_{M2}G$, ${}^{O}_{M3}G$ and the position of the passive marker ${}^{O}\vec{\boldsymbol{p}}_4$ with respect to the tracker camera is measured. Then, the location of the target ${}^{O}\vec{\boldsymbol{t}}$ and the biopsy needle tip ${}^{O}\vec{\boldsymbol{x}}$ are given by:

$$ {}^{O}\vec{\boldsymbol{t}} = {}^{O}_{M1}G\,{}^{M1}\vec{\boldsymbol{t}} \quad \text{and} \quad {}^{O}\vec{\boldsymbol{x}} = {}^{O}\vec{\boldsymbol{p}}_4 + d_0\,{}^{O}_{M2}G\,{}^{M2}\vec{\boldsymbol{l}} \tag{3.1} $$

The mockups were biopsied in a freehand manner by 5 urologists and by TRUS robot. All followed the usual 12-core sextant biopsy schema on 6 mock-ups (left/right × medial/lateral × apex/mid/base). During the biopsy by the TRUS robot (Figure 3.5b), the tracked probe and the needle was mounted on the TRUS robot and the 3D ultrasound image of the mockup was acquired by rotary scan. In real cases, the image needs to be segmented to create model of the prostate and the targets need to be planned accordingly. However, since the precise model of the prostate with the defined target was available, the model of the prostate with its planned target was loaded and manually aligned to the acquired 3D ultrasound image.

3.2.2 Results

Targeting error was calculated by measuring the 3D distance in mm between the gold standard target and the actual measured biopsy location. The accuracy and precision of the repeat biopsies and the estimated significant prostate cancer (0.5 cm^3 or greater) detection rate using a probability based model was calculated according to the definition given in (Han et al., 2012).

Table 9 shows the result of the accuracy of the robot biopsy compared to the human. As shown in Figure 3.6, result show that human biopsy resulted clustered patterns and under sampling of the prostate while the robot closely followed the pre-defined biopsy schema. The mean targeting error of the urologists and the robot was 9.0 and 1.0 mm, respectively. Robotic assistance significantly decreased repeat biopsy errors with improved accuracy and precision. The mean significant prostate cancer detection rate of the urologists and the robot was 36% and 43%, respectively ($p < 0.0001$).

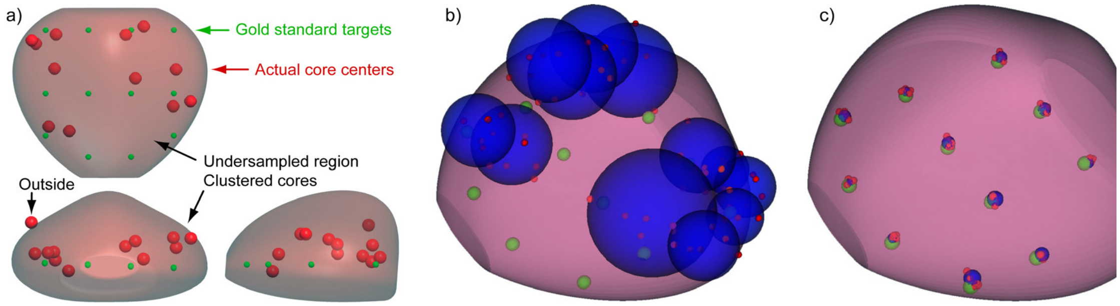

Figure 3.6: Biopsy accuracy measurement result.
a) Targeting error. Two views of prostate with gold standard. b) Core distribution by 1 urologist shows gold standard (green circles) and actual cores (red circles) of all 6 mock-ups, and minimum enclosing spheres for each gold standard point (blue circles). c) same core distribution with robotic assistance

Table 9: Comparison of biopsy targeting error, accuracy and precision of repeated biopsy, and significant PCa detection rate between the urologist and human

	Mean ± SD Targeting Error (mm)	Mean ± SD Repeat Biopsy (mm)		Mean ± SD Detection Rate (%)
Urologist No.		**Accuracy**	**Precision**	
1	11.4 ± 5.0	24.5 ± 8.7	11.3 ± 2.9	37.1 ± 5.4
2	10.2 ± 4.8	25.9 ± 6.6	10.5 ± 2.1	36.4 ± 3.9
3	8.5 ± 3.9	21.1 ± 7.4	11.0 ± 2.5	38.9 ± 3.1
4	7.1 ± 3.2	21.5 ± 7.1	9.1 ± 1.6	37.7 ± 2.7
5	7.9 ± 3.6	25.1 ± 7.3	8.6 ± 1.7	30.5 ± 3.6
Avg	9.0 ± 4.4	23.6 ± 7.4	10.1 ± 2.2	36.1 ± 3.3
TRUS Robot	1,0 ± 0.3	0.6 ± 0.2	1.7 ± 0.3	43.3 ± 0.7

3.3 Elastography

As shown in the previous section, the accuracy of the standard TRUS guided prostate biopsy can be improved by the robot. Another approach to improve the prostate biopsy is to perform ‘targeted biopsy’ guided by the advanced imaging modalities that can differentiate the tumors. One of the advanced imaging modalities that have potential to differentiate the tumor and the ordinary tissue is ultrasound elastography.

Ultrasound elastography is an image modality that can measure the stiffness of the tissue. As the cancerous and normal tissues typically differ in stiffness, targeted biopsy under elastography will allow suspicious regions identified in the image to be biopsied, independently or in addition to the sextant plan. Starting from 1990s, many methods for obtaining ultrasound elastography images have been developed (Ophir et al., 1991, Lerner et al., 1990, Nightingale et al., 2002, Turgay et al., 2006). Their principles behind the image formations are similar. The echoes from the tissues under varying level of mechanical stress or excitation are analyzed to infer the underlying mechanical properties of the tissues.

One of the first elastography images was acquired by Ophir et al. (Ophir et al., 1991) using the method which is now referred to as quasi-static elastography. In quasi-static elastography, the image is generated by correlating the ultrasound echo signals from the tissues under different levels of displacement. For each element of the transducer, the displacement of the tissue along the direction of the insonification (direction

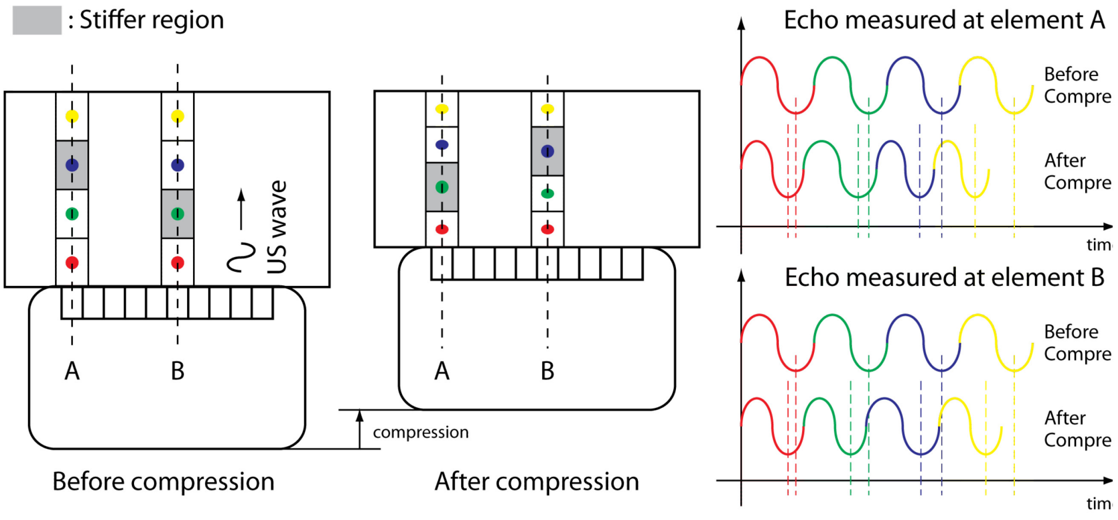

Figure 3.7: Principle of Quasi-static Elastography

of pulse and echo travel) is measured by the time delay estimation between the echo signals, as illustrated in Figure 3.7. Then, the strain of the tissue, which is inversely proportional to the stiffness under uniform stress, is estimated from the measured displacement. The required displacement of the tissues is usually generated from the compression induced by the imaging probe itself.

At the similar time, another method for acquiring elastography images, termed ‘Sonoelastography' was developed by Lerner et al. (Lerner et al., 1990). In sonoelastography, the tissues were vibrated at low frequencies (10-1000 Hz) by an external device to induce oscillations within soft tissues, and motion was detected by Doppler ultrasound. Nightingale et al. (Nightingale et al., 2002) developed an elastography imaging method named Acoustic radiation force impulse imaging (ARFI). In ARFI, focused ultrasound radiation force is used to generate a localized displacement within the tissue which is analyzed to deduce its mechanical properties. Salcudean et al. (Turgay et al., 2006) developed ‘Vibro-elastography’ where the tissue is externally vibrated over a range of frequencies simultaneously and the mechanical properties of the tissues are analyzed from a transfer function analysis of the resulting tissue displacements.

Among the all elastography methods described above, quasi-static elastography is the method that has been most widely implemented in commercial systems. However, as can be inferred from its principle explained above, the quality of the acquired images depends heavily on the displacement generated by the compression of the probe. Several researches have been made to improve the elastography image quality in this aspect. Boctor et al. (Foroughi et al., 2010), tracked an ultrasound probe as it was compressed against the tissue to acquire elastography and developed a method to select the best pairs of images for computing elastography based on the tracked position of the probe during the compression.

All the above mentioned methods for generating elastography images require access to the RF echo signal and ultrasound scanners that are equipped with special signal processing hardware and software. On the other hand, elastography images may be also generated from the standard B-mode images, which can be acquired from the video output of ultrasound scanners.

There are several pros and cons for generating elastogram from series of B-mode images. Possible advantages are:

1. It will allow elastography imaging on any existing ultrasound machine that are not equipped with the elastography function.

2. Advanced image processing algorithms are capable of measuring 2D in-planar displacements or even out of plane displacements, while the quasi-static elastography imaging that is currently widely used in commercial ultrasound scanners is only capable of measuring 1D displacements along the insonification direction. As the deformation of the tissue is inherently 3D phenomena, use of image processing algorithms may lead to more accurate analysis of the displacement and strain.

On the other hand, a possible disadvantage is that compared to the raw echo signals that are used internally by ultrasound machines for quasi static elastography, the B-mode images that are captured from the video output port of the ultrasound machines may have lower resolution.

Several previous research have generated elastography image from B-mode images (Revell et al., 2005, Zakaria et al., 2010). In (Revell et al., 2005),elastography image is generated from the B-mode image sequences of the Achilles and patella tendon undergoing deformation by flexion to extension movements. Deformation of the tissue is tracked by multiple hierarchical region-based matching using Normalized Cross Correlation and CD_2 (Cohen and Dinstein, 2002) as a similarity measure. In (Zakaria et al., 2010), elastography image of a hypertensive rat carotid artery is generated from its B-mode image sequence. Deformation of the tissue is tracked by calculating optical flow between series of image.

In this dissertation, different methods for generating displacement of the tissues to improve the quality of 'quasi-static' elastography images acquired from commercial ultrasound scanners were explored. The following paths for tissue displacements are considered, transrectal by robot manipulated TRUS probe, and transurethral or transperineal by external devices. Also, the possibility of generating elastography image from standard B-mode images by combining the image and the position information acquired from the controlled robot motion are explored.

The research in this section (Section 3.3) was supported by Prostate Cancer Training Award I received from Department of Defense (Grant No. W81XWH-11-1-0662). The scientific novelty claimed in this project is

- Controlled palpation of the prostate through the robot manipulated probe and other external palpation devices was tested for improving the quality of the elastography image.
- Generation of the elastography image from the series of B-mode images acquired during the robot controlled probe motion.

My personal <u>contribution</u> to this project was:

- Design of the palpation devices and experiments
- Development of robot motion control algorithm for controlled palpation of the prostate
- Development of image processing method for acquisition of elastography image from the series of B mode images acquired under controlled probe motion

3.3.1 Transrectal Palpation of the Prostate by Robot Controlled Probe Motion

The most commonly used method of generating varying level of tissue displacement required for elastography is by pressing the ultrasound probe against the skin with varying magnitude of pressure. Physicians are required to continuously 'palpate' the tissue by repeatedly compressing and retracting the ultrasound probe while imaging. Executing and maintaining such a controlled palpating motion to generate stable elastography image requires careful control of the probe by physician. This becomes even more challenging in case of biopsies where the physician has to concentrate on finding and targeting lesion in addition to palpating motion. As such, these suggest possible advantages of robot automation for elastography and targeting.

Due to the principle behind the image formation, the quality of the acquired elastography image is significantly influenced by the characteristic of this palpation motion. The palpation motion must follow certain constraints in order to acquire high quality elastography images. First, the orientation of the ultrasound imaging plane must remain constant throughout the palpation. Failing to do so will generate echoes from different regions of tissues to be compared against each other, leading to incorrect displacement measurement. Second, the palpation motion must generate the displacement of tissue along the insonification direction, as shown in Figure 3.8. Therefore, the ideal motion satisfying both constraints will be a pure in-plane translation of the image plane along the direction of the insonification. However, in case of prostate elastography, the anatomical constraint of the transrectal access imposes additional constraints, making the ideal motion difficult to achieve.

In the ideal conditions, to translate the image plane while maintaining its orientation, imaging the prostate requires full 6 degree of freedom (DoF) control (3 for constraining rotation + 3 for generating translation). However, this requirement conflicts with anatomical constraints, as shown in Figure 3.8. While in place, the motion of the probe is constrained to pivoting motion about the rectal sphincter and a translation about

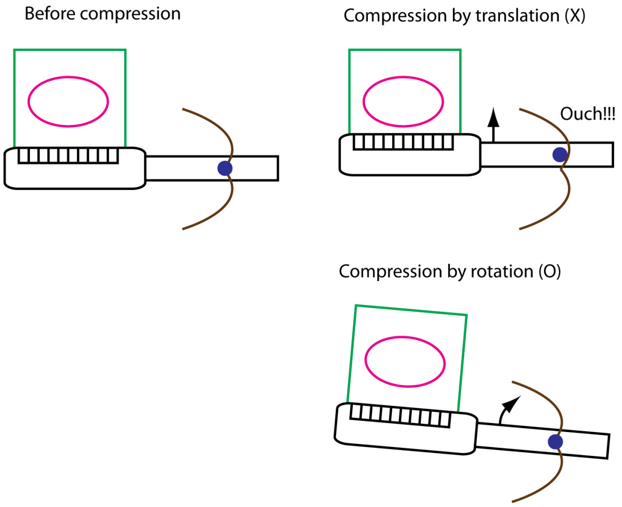

Figure 3.8: Constraints of the TRUS probe motion for elastography of the prostate

the probe axis. Accordingly, the TRUS robot has 4-DoF (3 rotational + 1 translational) for manipulating the probe. While 3 rotational DoF allows full control of the image plane orientation, 1 translational DoF restricts the possible pure translation along insonification direction to the direction of this DoF. The ideal palpation motion is only possible in the cases where the image plane lies on the axis of translation and the insonification direction of the probe is aligned with the axis.

As such, the optimal elastography palpating motion under constraints has been developed. This was implemented for lateral fire, sagittal, linear array TRUS probes (Hitachi EUP-U533). For this probe type, insonification is constant. Therefore, the ideal motion will be a translation that is not aligned with the translation degree of freedom of the robot. The solution is to rotate the image plane about its normal, compressing against the rectal wall while rotating the image plane about its normal direction $\vec{z} = [0,0,1]^T$. This ensures the palpation motion while maintaining the tissues to be imaged in the image plane. Moreover, for small angles the resulting motion will be close to translation along the insonification direction.

Configuration $G(\vec{\theta})$of the image plane with respect to the robot base coordinate system when the TRUS robot is at joint angle $\vec{\boldsymbol{\theta}} = [\theta_1, \theta_2, \theta_3, \theta_4]$, is described by following forward kinematics.

$$G(\vec{\boldsymbol{\theta}}) = \begin{bmatrix} R_1R_2R_3 & R_1R_2R_3\theta_4\vec{\boldsymbol{\omega}}_4 \\ \vec{\mathbf{0}} & 1 \end{bmatrix} \begin{bmatrix} R_0 & \vec{\mathbf{t}}_0 \\ \vec{\mathbf{0}} & 1 \end{bmatrix} \tag{3.2}$$

where $\begin{bmatrix} \mathrm{R}_0 & \vec{\mathbf{t}}_0 \\ \vec{\mathbf{0}} & 1 \end{bmatrix}$ is probe calibration describing configuration of the image plane at robot zero, $\mathrm{R}_\mathrm{i} = \mathrm{e}^{\widehat{\omega_\mathrm{i}}\theta_\mathrm{i}}$ is product of exponential formula for the rotation about axis $\vec{\boldsymbol{\omega}}_\mathrm{i}$ by θ_i. Image coordinate system is defined such that x and y axis corresponds to the horizontal and vertical direction of the image.

Image plane can be defined by its normal $\vec{\mathrm{n}}$ and an origin $\vec{\mathrm{p}}$ that it passes. From the kinematics of the robot, the coordinate of the normal $\vec{\mathrm{n}}$ and the origin $\vec{\mathrm{p}}$ in robot base coordinate system at certain reference configuration $\vec{\boldsymbol{\theta}} = [\theta_1, \theta_2, \theta_3, \theta_4]$ is given by $\vec{\mathbf{n}} = \mathrm{R}_1\mathrm{R}_2\mathrm{R}_3\mathrm{R}_0\vec{\mathrm{z}}$ and $\vec{\mathbf{p}} = \mathrm{R}_1\mathrm{R}_2\mathrm{R}_3\overrightarrow{\mathbf{t_0}} + \mathrm{R}_1\mathrm{R}_2\mathrm{R}_3\theta_4\vec{\boldsymbol{\omega}}_4$. Therefore all the points $\vec{\mathrm{x}}$ in space that lies on the image plane will satisfy relation:

$$\vec{\mathbf{n}}^\mathrm{T}\vec{\mathrm{x}} = (\mathrm{R}_1\mathrm{R}_2\mathrm{R}_3\mathrm{R}_0\vec{\mathrm{z}})^\mathrm{T}\vec{\mathbf{x}} = \vec{\mathbf{n}}^\mathbf{T}\vec{\mathbf{p}} = \vec{\mathbf{z}}^\mathrm{T}\mathrm{R}_0^\mathrm{T}(\overrightarrow{\mathbf{t}_0} + \theta_4\vec{\boldsymbol{\omega}}_4\ ) \tag{3.3}$$

If through the palpation motion the robot moves the joint angle to $\overrightarrow{\boldsymbol{\theta}'} = [\theta_1', \theta_2', \theta_3', \theta_4']$ such that the image plane is rotated about its normal $\vec{\mathbf{n}}$ by angle α, the normal and the origin of the image plane changes to $\vec{\mathbf{n}}' = \mathrm{R}_1'\mathrm{R}_2'\mathrm{R}_3'\mathrm{R}_0\vec{\mathrm{z}} = \mathrm{e}^{\hat{\mathrm{n}}\alpha}\vec{\mathbf{n}} = \vec{\mathbf{n}} = \mathrm{e}^{\hat{\mathrm{n}}\alpha}\mathrm{R}_1\mathrm{R}_2\mathrm{R}_3\mathrm{R}_0\vec{\mathrm{z}}$ and $\vec{\mathbf{p}}' = \mathrm{R}_1'\mathrm{R}_2'\mathrm{R}_3'\mathrm{R}_0\overrightarrow{\mathbf{t_0}} + \mathrm{R}_1'\mathrm{R}_2'\mathrm{R}_3'\mathrm{R}_0\theta_4'\vec{\boldsymbol{\omega}}_4$and the points $\vec{\boldsymbol{x}}'$ on this image plane will satisfy:

$$\vec{\mathbf{n}}'^\mathrm{T}\vec{\mathbf{x}}' = \vec{\mathbf{n}}^\mathbf{T}\vec{\mathbf{x}}' = \vec{\mathbf{n}}'^\mathrm{T}\vec{\mathbf{p}}' = \vec{\mathbf{z}}^\mathrm{T}\mathrm{R}_0^\mathrm{T}(\overrightarrow{\mathbf{t}_0} + \theta_4'\vec{\boldsymbol{\omega}}_4) \tag{3.4}$$

If θ_4 remains constant during palpation ($\theta_4 = \theta_4'$) and the joint angles $[\theta_1', \theta_2', \theta_3']$ that satisfy $\mathrm{R}_1'\mathrm{R}_2'\mathrm{R}_3'\mathrm{R}_0 = \mathrm{e}^{\hat{\mathrm{n}}\alpha}\mathrm{R}_1\mathrm{R}_2\mathrm{R}_3\mathrm{R}_0$ exists, then the points $\vec{\boldsymbol{x}}$ and $\vec{\boldsymbol{x}}'$ satisfy same equation meaning that the points on the image planes will remain same at both configuration.

To find a trajectory of joint angles $\vec{\theta}'(\mathrm{t}) = [\theta_1', \theta_2', \theta_3', \theta_4']$ that will generate a motion that will rotate image plane about its normal by given angular profile $\alpha(\mathrm{t})$ starting from the reference $\vec{\theta}$, inverse kinematics problem:

$$\mathrm{R}_1'\mathrm{R}_2'\mathrm{R}_3' = \mathrm{e}^{\widehat{\omega_1}\theta_1'}\mathrm{e}^{\widehat{\omega_2}\theta_2'}\mathrm{e}^{\widehat{\omega_3}\theta_3'} = \mathrm{e}^{\hat{\mathrm{n}}\alpha}\mathrm{R}_1\mathrm{R}_2\mathrm{R}_3 = \mathrm{R}_1\mathrm{R}_2\mathrm{R}_3\mathrm{R}_0\mathrm{e}^{\hat{\mathrm{z}}\alpha}\mathrm{R}_0^\mathrm{T} = \mathrm{X} \tag{3.5}$$

needs to be solved for every α. Solution to this problem is described in Chapter 2.

This motion keeps all the points on the image plane during palpation, but the motion of the tissue relative to the probe is not necessarily translation along beam direction. When the amplitude of rotation is small, this can approximate the pure translation.

3.3.2 Transurethral Palpation of the Prostate

The most common palpation mode for elastography is with the probe itself, as shown above. Alternatively, displacement of the prostate for elastography can be generated by external palpating devices, providing additional options to potentially improve the quality of elastography imaging and prostate cancer detection.

An alternative palpation motion that we propose and investigate is transurethral. A palpating device has been developed and is being tested. This consists of a pulsating air pump and an inflatable balloon connected to a catheter, as shown in Figure 3.9. The balloon can be placed through the urethra within the prostate. The frequency of pulsation and pressure of the air are adjustable to periodically inflate and deflate the catheter balloon.

Figure 3.9 shows also the experiment setup for the transurethral palpation. Commercially available prostate elastography mockup do not simulate a hollow physical urethra, to which the catheter can be inserted. Special prostate elastography mockups were constructed for the experiments. The mockup is made in a gelatin box with cavity simulating rectum, the prostate with stiffer lesions, and the urethra. The model prostate was made of tofu with cooked chicken breast inclusions. In order to confirm the findings of the

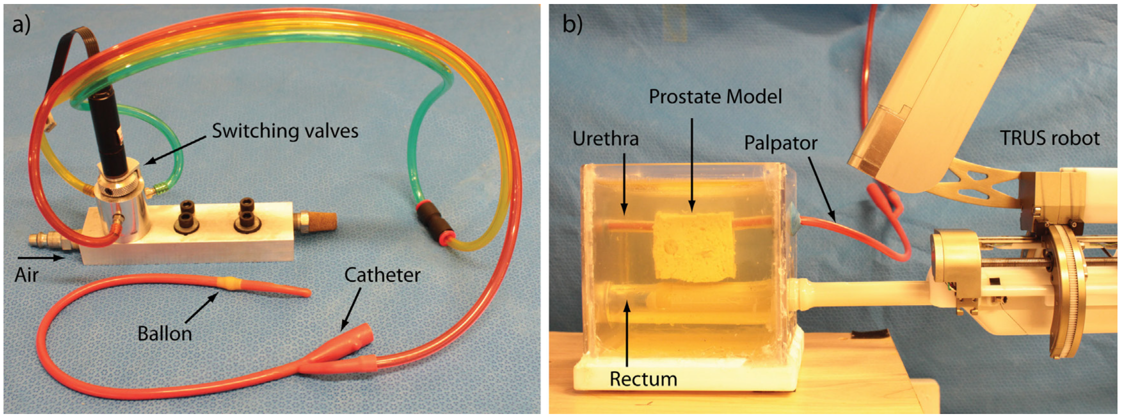

Figure 3.9: Setup for the elastography image acquisition using transurethral palpation. a) Transurethral Palpator and pump. b) Experimental Setup showing the custom prostate model, the TRUS robot supporting the probe, and the palpator placed through the simulated urethra.

elastography image the inclusions are slightly visible in B-mode ultrasound.

Figure 3.10 shows the elastography image of the mockup acquired using the transurethral palpating device. It can be seen that the inserted lesion made of cooked chicken, which is stiffer than tofu, shows up as a stiff lesion enclosed in the softer region (blue area enclosed in green and red) in the elastography image. Since the catheter of the device is filled with the air, a portion of the mockup above the inserted catheter is not visible in ultrasound. This can be corrected by replacing the air with a liquid. This and additional experiments are in progress.

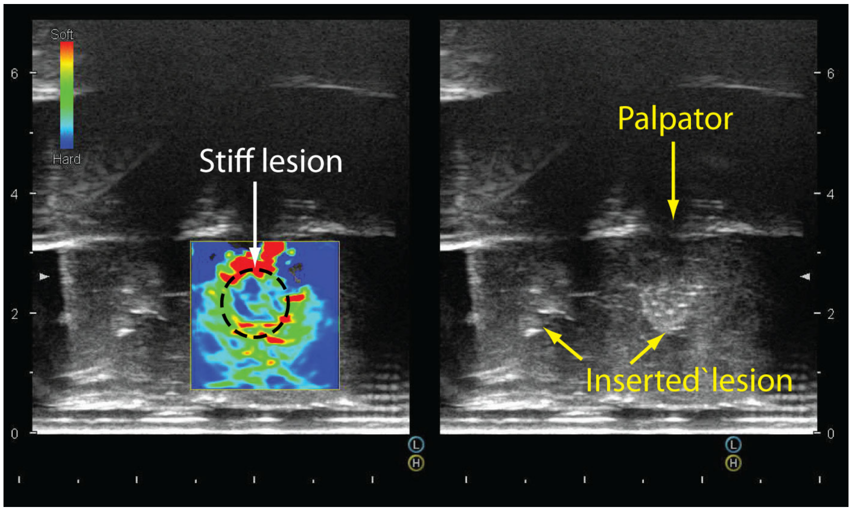

Figure 3.10: Elastography image acquired under transurethral palpation

3.3.3 Transperineal Palpation of the Prostate

Yet another possible way to palpate the prostate is through the perineum wall. A transperineal palpating device developed for this is shown in Figure 3.11, installed on the commercial prostate elastography mockup, (CIRS Inc. Norfolk, VA) for the imaging test. The device consists of a round palpation plate connected to the spring loaded piston that is actuated by the same pulsating air pump used for the transurethral palpator. The device can apply a periodical compression on the perineum skin through the plate and generate uniform stress over the entire transverse section of the prostate. Elastography image of the transverse section of the mockup obtained under transperineal palpation is shown in Figure 3.11. The image reveals a stiff lesion that is not visible n B-mode image.

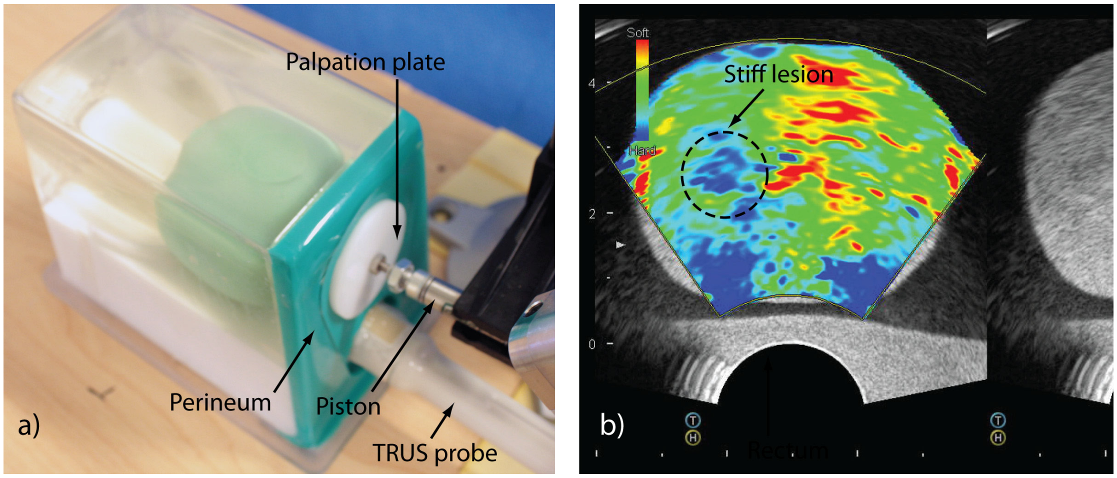

Figure 3.11: Setup for the elastography image acquisition using transperineal palpation.
a) Experiment setup showing the transperineal palpator and prostate mockup
b) Elastography image of the mockup acquired under transperineal palpation

3.3.4 Elastography Imaging from Robotically Acquired B-mode Image Series

In this section, a possibility of generating elastography images from the series of B-mode images captured during robotic palpation with the TRUS was investigated. The deformation of the tissue under robotic palpation was tracked by optical flow and the strain of the tissue was estimated from the tracked deformation. Relative motion in the image originating from the palpating motion of the probe is compensated by using the tracked position of the probe.

As shown in Figure 3.12, during elastography imaging, displacement of the object can occur from two sources, one from the rigid body motion plus deformation of the tissue by the compression of the probe and the other from the relative motion between the probe and the object. The latter does not reflect the true displacement of the tissue and needs to be compensated for to correct displacement measurements. Therefore, when the probe is moved to apply deformation, optical flow estimated from the B-mode images will not reflect true displacement unless the probe motion is tracked and compensated from the calculated flow. The ability of the TRUS2-Robot with the calibrated probe to track the position of the individual pixel throughout the palpation motion allows the accurate estimation of the displacement from the optical flow.

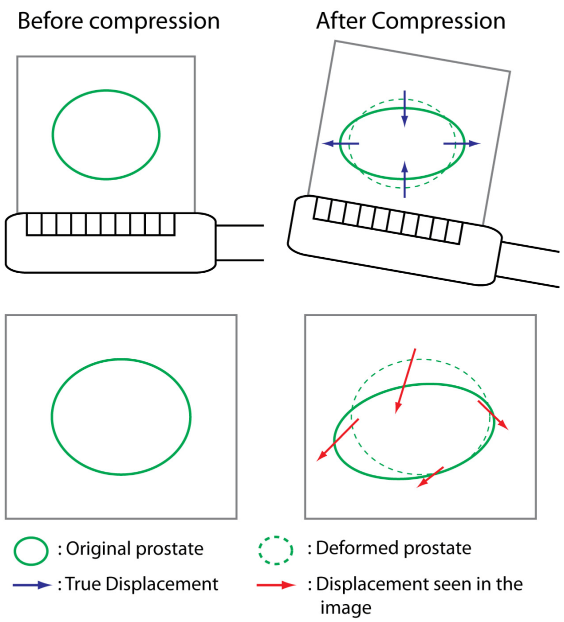

Figure 3.12: Displacement in the image during palpation

In this research iterative Lucas-Kanade method (Bouguet, 2001) and Farneback's algorithm (Farnebäck, 2003) were tried as their robust implementation was available in OpenCV software library (http://opencv.org/). Lucas-Kanade method assumes that intensities of pixels remain constant through the motion and tries to find displacements that minimize the brightness difference between the reference and displaced patch. Farneback's algorithm tries to find displacement by modeling local image patches as quadratic function and then comparing model of the reference and displaced patch.

From the optical flow measurement, at reference robot configuration $\vec{\theta}_0$ a pixel located at $[u_0, v_0]$. After the robot moves to joint angle $\vec{\theta}_i$, from the optical flow measurement, this pixel is seen to be moved to $[u_i, v_i]$. The displacement of the pixel $[\Delta u, \Delta v] = [u_i - u_0, v_i - v_0]$ can be coming from the motion of the tissue or from the motion of the probe relative to the tissue. The true displacement of the tissue can be recovered by mapping these image coordinate measurement to the robot base coordinate system by kinematics and calibration. The coordinate $[x_i, y_i, z_i]$of the pixels $[u_i, v_i]$ will be:

$$[x_i, y_i, z_i, 1]^T = \begin{bmatrix} R_1R_2R_3 & R_1R_2R_3\theta_4\vec{\omega}_4 \\ 0 & 1 \end{bmatrix} \begin{bmatrix} R_0 & \vec{t}_0 \\ 0 & 1 \end{bmatrix} [u_i, v_i, 0,1]^T = g(\vec{\theta}_i)[u_i, v_i, 0,1]^T \tag{3.6}$$

Then, the true displacement of pixel from their reference position will be:

$$[\Delta x, \Delta y, \Delta z, 1]^T = G(\vec{\theta}_i)[u_i, v_i, 0,1]^T - G(\vec{\theta}_0)[u_0, v_0, 0,1]^T \tag{3.7}$$

$$G^{-1}(\vec{\theta}_0)[\Delta x, \Delta y, \Delta z, 1]^T = [\Delta u', \Delta v', 0,1]^T = G^{-1}(\vec{\theta}_0)g(\vec{\theta}_i)[u_i, v_i, 0,1]^T - [u_0, v_0, 0,1]^T \tag{3.8}$$

and the strains must be estimated from $[\Delta u', \Delta v']$ instead of $[\Delta u, \Delta v]$

From the continuum mechanics theory, the 2-D Lagrangian strain tensor E of the particle that was at $[x_0, y_o]^T$ in the reference configuration, that is displaced by $[u(x_0, y_0), v(x_0, y_0)]^T$ in current configuration is give as:

$$E = \frac{1}{2}\begin{bmatrix} \left(\frac{\partial u}{\partial x}\right)^2 + \left(\frac{\partial u}{\partial y}\right)^2 + 2\frac{\partial u}{\partial x} & \frac{\partial u}{\partial x}\frac{\partial v}{\partial x} + \frac{\partial u}{\partial y}\frac{\partial v}{\partial y} + \frac{\partial u}{\partial y} + \frac{\partial v}{\partial x} \\ \frac{\partial u}{\partial x}\frac{\partial v}{\partial x} + \frac{\partial u}{\partial y}\frac{\partial v}{\partial y} + \frac{\partial u}{\partial y} + \frac{\partial v}{\partial x} & \left(\frac{\partial v}{\partial x}\right)^2 + \left(\frac{\partial v}{\partial y}\right)^2 + 2\frac{\partial v}{\partial y} \end{bmatrix} \tag{3.9}$$

For small infinitesimal displacement this becomes:

$$E = \frac{1}{2}\begin{bmatrix} 2\frac{\partial u}{\partial x} & \frac{\partial u}{\partial y} + \frac{\partial v}{\partial x} \\ \frac{\partial u}{\partial y} + \frac{\partial v}{\partial x} & 2\frac{\partial v}{\partial y} \end{bmatrix} \tag{3.10}$$

The displacement field $[u(x, y), v(x, y)]^T$obtained from the optical flow calculation is noisy and simply taking partial derivatives of this will amplify the noise, leading to very noisy strain field estimation. Therefore least square strain estimator presented in (Kallel and Ophir, 1997) for 1 dimension strain estimation was extended to 2 dimension as in (Pan et al., 2012) and used to estimate smoother strain field from the displacement field.

For each point $[x, y]^T$in the displacement field, $(2n + 1) \times (2m + 1)$ patch centered at $[x, y]^T$ is selected. Displacement field $[u(x, y), v(x, y)]^T$within this patch is modeled to be linearly varying as

$$\begin{bmatrix} u(x, y) \\ v(x, y) \end{bmatrix} = \begin{bmatrix} a_1x + b_1y + c_1 \\ a_2x + b_2y + c_2 \end{bmatrix} \tag{3.11}$$

The coefficients a_1 to c_2s can be determined by least square fitting the displacement field data to the model by solving over constrained system:

$$\begin{bmatrix} x_{-m} & y_{-n} & 1 \\ \vdots & \vdots & \vdots \\ x_m & y_n & 1 \end{bmatrix} \begin{bmatrix} a_1 & a_2 \\ b_1 & b_2 \\ c_1 & c_2 \end{bmatrix} = \begin{bmatrix} u_{-m} & v_{-n} \\ \vdots & \vdots \\ u_m & v_n \end{bmatrix} \tag{3.12}$$

Then the strain can be calculated from the coefficients as:

$$E = \frac{1}{2} \begin{bmatrix} 2a_1 & b_1 + a_2 \\ b_1 + a_2 & 2b_2 \end{bmatrix} \tag{3.13}$$

Figure 3.13 below shows the pair of B-mode image of a prostate mockup, optical flow calculated between two images and elastography image of a same region generated from the optical flow and ultrasound machine's elastography. This shows an image comparable to the one generated by ultrasound machine's elastography also shown in Figure 3.13.

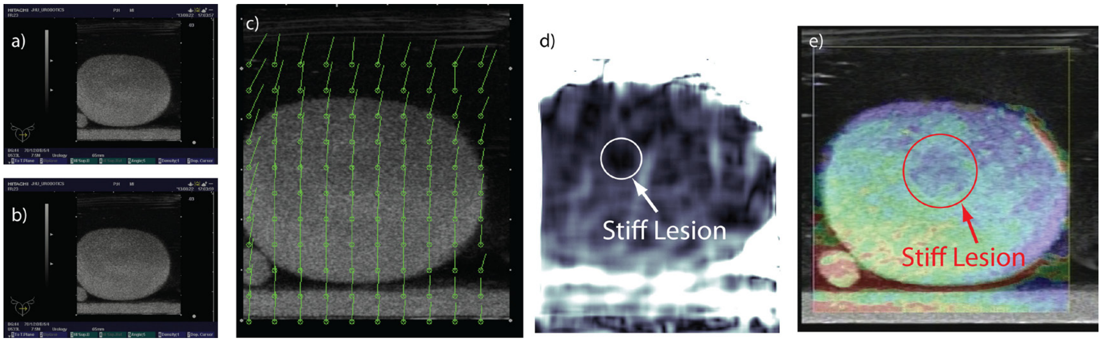

Figure 3.13: Elastography images generated from the B-mode images.
a, b) Pair of B mode image used for optical flow calculation, c) Calculated optical flow
d) Elastography image generated from the optical flow, and e) Elastography image of the same region acquired by the ultrasound machine. Notice the same stiff lesion is detected from both image.

3.4 Ultrasound-CT Image Fusion

Fusing image sets A and B of the same anatomical site is the process of finding the optimal transformation ${}^{A}_{B}T$ between their coordinate systems that aligns the corresponding anatomical features as well as possible. This is usually done by calculating the transformation that minimizes the distance between the homologous anatomical landmarks identified in each image or by iteratively searching for a transformation from one image to another that optimizes a certain similarity metric between the images.

One of the biggest challenges in similarity based fusion methods is finding the similarity measure between the two images. This is especially difficult in case of cross modality image-fusion, where the same anatomical structures have different appearances due to the different principles of image formation in each medical imaging modality. Many similarity metrics have been used for cross modality image-fusion such as correlation ratio (Leroy et al., 2004, Penney et al., 2004, Roche et al., 2001), mutual information (Wein et al., 2007, von Berg et al., 2004) and LC2 (Linear Correlation of Linear Combination) (Wein et al., 2008). Even though particular methods work impressively well in specific situations, there is no commonly accepted or golden standard measure for image similarity.

The difficulty of finding similarity metrics can be circumvented by introducing a common reference frame to which both images can be registered. This approach has been employed in several existing researches on fusion between the fluoroscope images (Jain et al., 2012, Jain et al., 2007, French et al., 2005) or CT images (Steggerda et al., 2005) of the implanted seeds and the TRUS image of the prostate during brachytherapy for intraoperative dosimetry. Jain et al. (Jain et al., 2007, Jain et al., 2012) used a special fiducial marker designed to track the non-isocentric C-Arm (Jain et al., 2005), and triangulated the location of the implanted seeds from multiple C-Arm view. This marker was also registered to the TRUS, enabling the measured seed locations to be displayed on the TRUS image of the prostate. French et al. (French et al., 2005) and Steggerda et al. (Steggerda et al., 2005) used the image of the TRUS probe itself to register the image of the seeds to the TRUS image.

This section presents a method of image-fusion between ultrasound and CT following a similar approach using the TRUS robot co-registered to both image modalities. For the TRUS robot with the calibrated probe, the ultrasound image is registered to the robot base frame. If the robot is also registered to the CT scanner, then image-fusion between the ultrasound and CT images can be acquired. This circumvents the calculation of similarity measures or finding homologous features. The accuracy of the image-fusion is evaluated, and its utility is verified in a fused image-guided targeting experiment simulating percutaneous access to the kidney.

The scientific novelty of the research presented in this section is:

- A new method of ultrasound to CT image-fusion facilitated by using the TRUS robot as a common reference.

My personal contribution to this project was:

- Design and software implementation of the method for registering TRUS1 robot to CT image.
- Design and software implementation of the image fusion algorithm and evaluation

Registration of TRUS Robot to CT Image

In order to fuse the ultrasound and CT image, TRUS1 robot needs to be registered to the CT image. Several methods have been developed for the registration of the image-guided robots to CT image. In (Susil et al., 1999, Fichtinger et al., 2002), image-guided robot is registered to the CT through the stereotactic frame attached to the end-effector of the robot. The frame is based on the Brown-Roberts-Wells frame (Brown, 1979) and allows registration from single CT image slices provided that the frame is oriented such that the image slice intersects all of its line segments. In (Patriciu et al., 2001), image-guided robot is registered without imaging by aligning the end effector needle to the laser markers equipped in the CT scanner.

Since the end effector of the TRUS1 robot is abdominal ultrasound probe, it will be difficult to use laser based registration methods proposed in (Patriciu et al., 2001). Instead, a CT registration marker was mounted on the TRUS1-Robot. The registration marker consists of a CT line marker (CT-SPOT, Beekeley Corp. Bristol, CT) wrapping around the probe adapter of the robot as shown in Figure 3.14. The line marker forms two intersecting planes that are defined by equation ${}^{R}\boldsymbol{n}_1 \cdot \boldsymbol{x} = d_1$ and ${}^{R}\boldsymbol{n}_2 \cdot \boldsymbol{x} = d_2$ in robot coordinate system. The normal vector of the planes (${}^{R}\boldsymbol{n}_1$, ${}^{R}\boldsymbol{n}_2$) and their distance (d_1, d_2) from the robot coordinate system origin are known from the CAD model of the robot.

Configuring the line markers in N-shaped configuration as it was done in (Susil et al., 1999, Fichtinger et al., 2002) could have allowed registration using a single image slice, instead of scanning the entire registration marker to acquire the image of the intersecting planes. However, this does not necessarily mean that the separate registration CT scan is necessary as the robot and the registration marker will be imaged with the patient during diagnostic scan at the beginning of the intervention procedure.

The robot is scanned in CT and then from its image, the markers are segmented by thresholding and region growing as shown in Figure 3.14. From the set of voxels belonging to the marker, two planes are fitted as shown in Figure 3.15. The normal vector and the distance pair (${}^{I}\boldsymbol{n_1}, c_1$) and (${}^{I}\boldsymbol{n_2}, c_2$) defining the two fitted planes in image coordinate system are calculated.

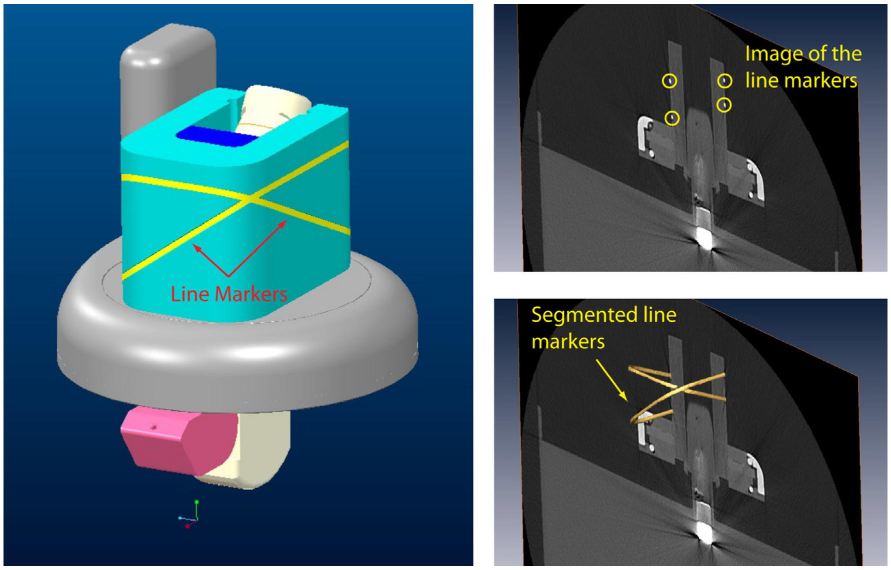

Figure 3.14: Registration marker and its CT image

The correspondence between the two planes in the image and the robot coordinate system, determines the 5 out of 6-DoF in the registration ${}^{I}_{R}G = \begin{bmatrix} {}^{I}_{R}R & {}^{I}_{R}\boldsymbol{t} \\ \boldsymbol{0} & 1 \end{bmatrix}$ between the robot and the image coordinate system, with the remaining 1-DoF being the translation along the line of intersection between the planes, as proved in the calculation below. This final DoF is constrained by translating the model of the registration marker along the intersection line until it overlaps the segmented image, as shown in Figure 3.15.

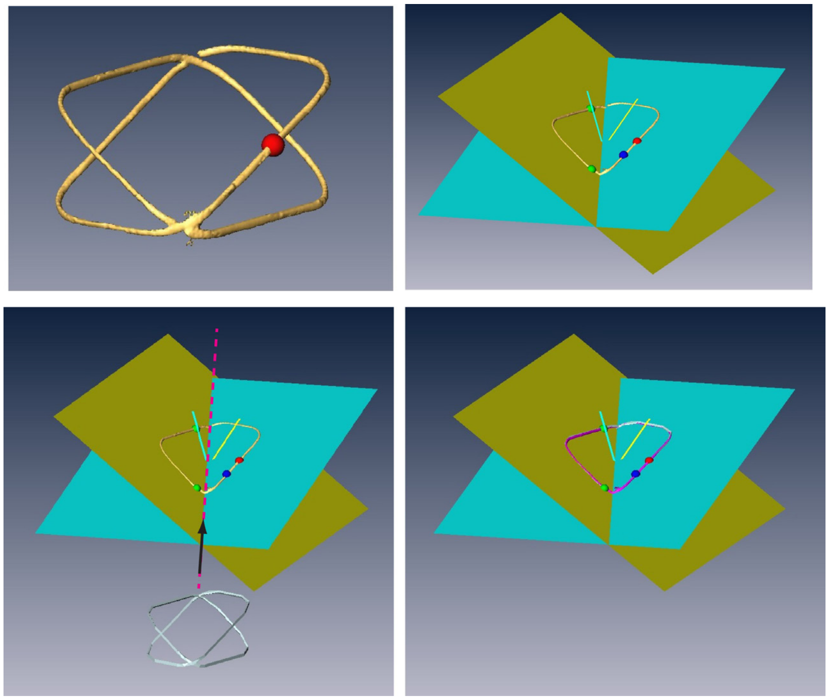

Figure 3.15: Marker model registered to its segmented image by fitted planes

Registration from two corresponding planes

From the CAD model and the images of the registration marker we have two pair of correspondence between the planes in the image and the robot coordinate system.

$$({}^{R}\boldsymbol{n_1}, d_1) \text{ and } ({}^{I}\boldsymbol{n_1}, c_1) \qquad ({}^{R}\boldsymbol{n_2}, d_2) \text{ and } ({}^{I}\boldsymbol{n_2}, c_2)$$

Let's denote the unknown registration from robot to image coordinate system ${}^{I}_{R}G = \begin{bmatrix} {}^{I}_{R}R & {}^{I}_{R}\boldsymbol{t} \\ \boldsymbol{0} & 1 \end{bmatrix}$, then we have following relation between the corresponding normal vectors.

$${}^{I}\boldsymbol{n_1} = {}^{I}_{R}R\ {}^{R}\boldsymbol{n_1} \tag{3.14}$$

$${}^{I}\boldsymbol{n_2} = {}^{I}_{R}R\ {}^{R}\boldsymbol{n_2} \tag{3.15}$$

Parameterizing the unknown rotation ${}^{I}_{R}R = e^{\widehat{\boldsymbol{\omega}}\theta}, |\boldsymbol{\omega}| = 1$ we have

$$\boldsymbol{\omega}^T\ {}^{I}\boldsymbol{n_1} = \boldsymbol{\omega}^T e^{\widehat{\boldsymbol{\omega}}\theta}\ {}^{R}\boldsymbol{n_1} = \boldsymbol{\omega}^T\ {}^{R}\boldsymbol{n_1} \text{ and } \boldsymbol{\omega}^T\ {}^{I}\boldsymbol{n_2} = \boldsymbol{\omega}^T\ {}^{R}\boldsymbol{n_2} \tag{3.16}$$

which is arranged as

$$\boldsymbol{\omega}^T\left({}^I\boldsymbol{n}_1 - {}^R\boldsymbol{n}_1\right) = 0 \text{ and } \boldsymbol{\omega}^T\left({}^I\boldsymbol{n}_2 - {}^R\boldsymbol{n}_2\right) = 0 \tag{3.17}$$

Then $\boldsymbol{\omega}$ can be calculated by

$$\boldsymbol{\omega} = \left({}^I\boldsymbol{n}_1 - {}^R\boldsymbol{n}_1\right) \times \left({}^I\boldsymbol{n}_2 - {}^R\boldsymbol{n}_2\right), |\boldsymbol{\omega}| = 1 \tag{3.18}$$

and θ can be calculated by solving Paden-Kahan subproblem 1 ${}^I\boldsymbol{n}_1 = e^{\widehat{\omega}\theta}\,{}^R\boldsymbol{n}_1$

Now for any corresponding points ${}^I\boldsymbol{x}$ and ${}^R\boldsymbol{x}$ on the planes in image coordinate system and the robot coordinate system, respectively we have following relation.

$${}^I\boldsymbol{n}_1^T\,{}^I\boldsymbol{x} = {}^I\boldsymbol{n}_1^T\left({}^I_R R\,{}^R\boldsymbol{x} + {}^I_R\boldsymbol{t}\right) = {}^R\boldsymbol{n}_1^T\,{}^R\boldsymbol{x} + {}^I\boldsymbol{n}_1^T\,{}^I_R\boldsymbol{t} = d_1 + {}^I\boldsymbol{n}_1^T\,{}^I_R\boldsymbol{t} = c_1 \tag{3.19}$$

$${}^I\boldsymbol{n}_2^T\,{}^I\boldsymbol{x} = {}^I\boldsymbol{n}_2^T\left({}^I_R R\,{}^R\boldsymbol{x} + {}^I_R\boldsymbol{t}\right) = {}^R\boldsymbol{n}_2^T\,{}^R\boldsymbol{x} + {}^I\boldsymbol{n}_2^T\,{}^I_R\boldsymbol{t} = d_2 + {}^I\boldsymbol{n}_2^T\,{}^I_R\boldsymbol{t} = c_2 \tag{3.20}$$

This leads to under constrained system of equation

$$\begin{bmatrix} {}^I\boldsymbol{n}_1^T \\ {}^I\boldsymbol{n}_2^T \end{bmatrix} {}^I_R\boldsymbol{t} = \begin{bmatrix} c_1 - d_1 \\ c_2 - d_2 \end{bmatrix} \tag{3.21}$$

Therefore ${}^I_R\boldsymbol{t}$ can be parameterized as ${}^I_R\boldsymbol{t} = \boldsymbol{p} + \lambda\boldsymbol{l}$ where $\boldsymbol{p}$ is a one of solutions to above under constrained equation and $\boldsymbol{l} = {}^I\boldsymbol{n}_1 \times {}^I\boldsymbol{n}_2$, which implies that the parameterized line is the line of the intersection between two planes.

3.4.1 Image Fusion and Accuracy Measurement

From the registration process described in previous section, the TRUS1-Robot is registered to CT image ${}^I_R G = \begin{bmatrix} {}^I_R R & {}^I_R\boldsymbol{t} \\ \boldsymbol{0} & 1 \end{bmatrix}$. Abdominal ultrasound probe mounted on the TRUS1-Robot is calibrated using the same method described in Chapter 2 and thus the ultrasound is registered to the robot ${}^R_U G = \begin{bmatrix} {}^R_U R & {}^R_U\boldsymbol{t} \\ \boldsymbol{0} & 1 \end{bmatrix}$. Then, the image-fusion between the ultrasound and CT image can be calculated as ${}^I_U G = {}^I_R G \cdot {}^R_U G$. The accuracy of this fusion method was verified by imaging a mockup with the inclusions that are both visible in the ultrasound and CT image.

The mockup, shown in Figure 3.16, is a box of gelatin containing 4 by 4 array of cylindrical shaped inclusion with 15 mm spacing between the neighboring inclusions. The inclusions were made of agar and glass beads were mixed to make the inclusions highly visible in both ultrasound and CT. This mockup was submerged in the water tank and the robot was placed to image the mockup with the ultrasound. The entire

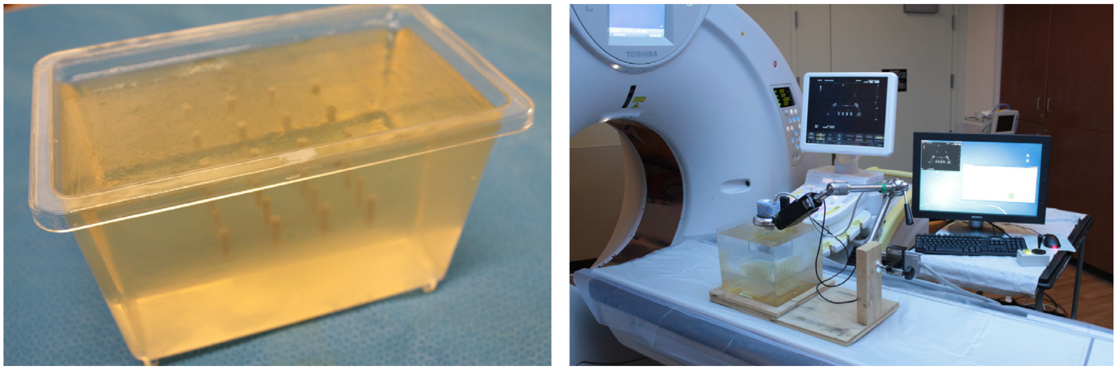

Figure 3.16: Mockup and the experiment setup for measuring fusion accuracy

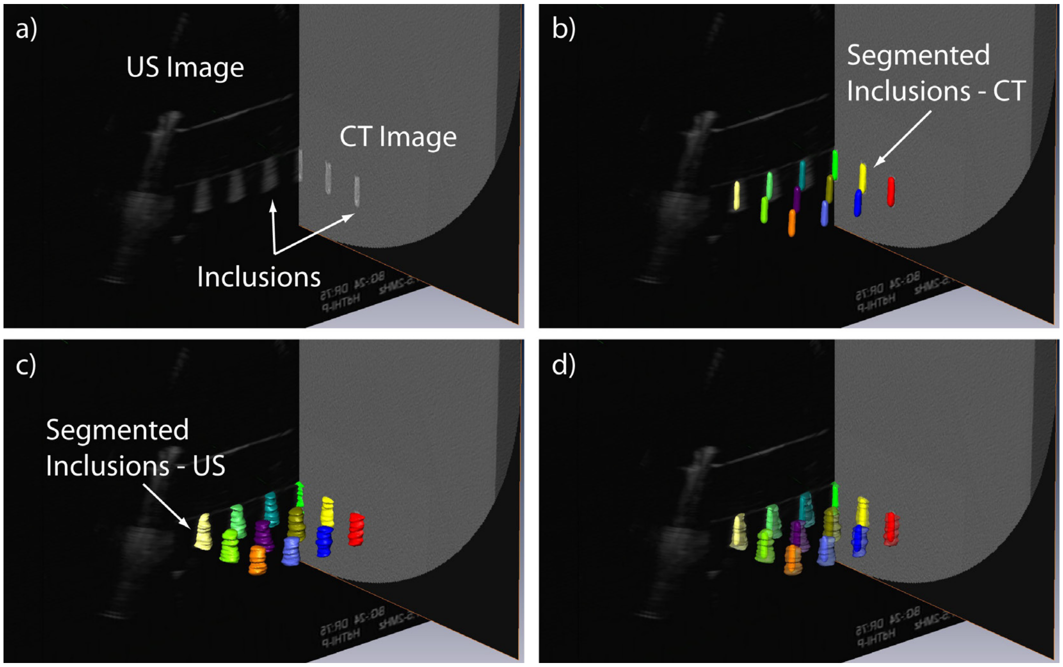

Figure 3.17: Fused ultrasound and CT images and segmented inclusions

robot and the mockup assembly were imaged in the CT scanner as shown in Figure 3.16. and right after the CT scan, robot moved the probe to scan the mockup with the ultrasound. In order to prevent the mockup from moving inside the aquarium, the CT images were acquired without moving the scanner bed.

3D ultrasound images were generated from the acquired 2D image slices and robot position data. The inclusions were manually segmented from both the 3D ultrasound and CT images. The robot was registered to the CT image by ${}^{I}_{R}G$ and the 3D ultrasound image was overlaid to the CT image as shown in Figure 3.17 by using the registration ${}^{R}_{U}G$. The accuracy of the image-fusion (Table 10) was measured as a distance between the centroid of the inclusions segmented from ultrasound and CT image.

Table 10: Image fusion measurement accuracy result.

Tgt #	**dx**	**dy**	**dz**	**Norm**
1	0.736	0.731	1.780	2.060
2	0.413	0.300	0.060	0.514
3	0.699	-0.973	-0.760	1.419
4	1.616	-1.947	-1.580	2.983
5	0.223	0.587	1.460	1.589
6	0.442	-0.615	0.590	0.960
7	0.945	-1.548	-0.710	1.947
8	1.535	-1.722	-1.750	2.895
9	-0.417	0.020	1.190	1.261
10	0.273	-0.880	-0.150	0.933
11	1.007	-1.820	-1.120	2.362
12	1.683	-1.667	-1.900	3.037
13	-0.603	0.078	0.190	0.637
14	0.255	-1.333	-0.860	1.607
15	0.930	-1.431	-1.750	2.444
16	1.368	-1.362	-2.350	3.041
Mean ± Std	0.694 ± 0.676	-0.849 ± 0.912	-0.479 ± 1.272	**1.856 ± 0.873**
[Min, Max]	[-0.603, 1.683]	[-1.947, 0.731]	[-2.350, 1.780]	**[0.514, 3.041]**

3.4.2 Fused Image-Guided Targeting Test

In urology, potential application of the describe image-fusion method is cryoablation of the kidney tumor or percutaneous nephrolithotomy (PCNL). Both procedures requires percutaneous access to the targets identified in CT image and can benefit from real-time monitoring of the procedure by ultrasound. For example, in cryoablation, cryoprobe is percutaneously delivered to the kidney tumor identified in CT image, and ultrasound can be used to monitor the growth of the iceball during the ablation to ensure optimal margins.

Ultrasound and CT image-guided targeting experiment simulating the situation of percutaneous access to the kidney will be performed to verify the utility of the fusion method.

4 MRI-guided Robot for Prostate Biopsy

One of the limitations of the current transrectal ultrasound (TRUS) image-guided prostate biopsy is that the TRUS imaging cannot typically discriminate cancerous from the normal tissues. As a result, instead of sampling the cancer suspicious regions (CSR) identified from the image, normally the prostate is systematically sampled by targeting the biopsies according to the sextant plan.

There have been many researches made on imaging prostate cancer. Among the imaging modalities, Magnetic Resonance Imaging (MRI) provides the highest spatial and contrast resolution on prostate anatomy (Hricak et al., 2007) and functional MRI techniques (MR spectroscopy, diffusion-weighted, and dynamic contrast enhanced imaging) have shown substantial potential to complement T2-weighted MRI in improving prostate cancer localization (Kelloff et al., 2009). Therefore, an MRI-guided robot that can precisely deliver a needle to the location identified in the MR image, can enable targeted sampling of the prostate at CSR. Furthermore, such a robot can be also used as a tool for precisely sampling the tissues to examine the correlation between the image abnormalities and the pathology.

Most challenging and important requirement for an MRI-guided robot is the MRI safety of the robot hardware. American Society for Testing and Materials (ASTM) set a series of standards to test (ASTM F2052, F2213, F2182, F2119) and classify (ASTM F2503) devices for the MRI environment, as shown in Table 11. In the U.S., compliance to these standards is required for medical device regulatory clearance by the Food and Drug Administration (FDA).

The space inside the MRI scanner bore is characterized by high static magnetic field (up to 3T in clinical scanners), rapidly changing radiofrequency and gradient of the fields. As a result, magnetic materials will experience high force and torques, and conducting materials have danger of heating by induced eddy current. Therefore, the ASTM standards specifically note that devices may classify as MRI-Safe on a scientifically based rationale of being nonconducting and nonmagnetic.

In addition to the safety, influence of the devices on the MR image quality is as important, especially if the devices are used for MRI-guided interventions where position errors due to image artifacts can affect the outcome of the interventions. Magnetic susceptibility, geometry of the material and MR imager settings

Table 11: ASTM F2503 Classification for the MRI environment

MRI-Safe MR	Is an item that poses no known hazards in all MR environments.
MRI-Conditional MR	Is an item that has been demonstrated to pose no known hazards in a specified MR environment with specified conditions of use. Field conditions that define the specified MR environment include field strength, spatial gradient, dB/dt (time rate of change of the magnetic field), radio frequency (RF) fields, and specific absorption rate (SAR).
MRI-Unsafe MR	Is an item that is known to pose hazards in all MR environments.

can affect the magnitude and direction of the artifacts (Schenck, 1996) , and electric signals inside the devices may interfere with the scanner field and generate noise.

These requirements for MRI safety and image quality impose constraints on the materials, sensors and actuators used in the MRI-guided robots. To meet these requirements, pneumatic stepper motor (PneuStep) (Stoianovici et al., 2007) was developed in Urology Robotics lab. The motor is completely made of nonmagnetic, nonconducting materials, actuated by air and sensed by lights. This MRI-safe motor was used as a basic actuator for the MRI-guided robots presented in this chapter.

This chapter presents two different MR image-guided robots and their application to prostate biopsy. One robot is used for transrectal biopsy in the animal study and the other MRI-guided robot is currently undergoing clinical trial for transperineal saturation biopsy. The contributions to the development of these systems included in this dissertation are partially related to the design, preclinical evaluation, in-vivo animal / human experiments, validation of the MRI safety and accuracies in various environments, and fully on the development of the registration algorithm and image-guidance software.

4.1 MRI Guided Robot for Transrectal Biopsy

The following section presents the MRI-guided robot developed for transrectal prostate biopsy and the result from animal study (Srimathveeravalli et al., 2013, Stoianovici et al., 2013b). The structure of the robot, kinematics, evaluation of its performance, effect of the robot in the MR image and animal experiment for evaluating the feasibility of the biopsies are described.

As have been reviewed in Chapter 1, one of the first devices developed for MRI-guided transrectal access of the prostate robot was the APT-I (Access to Prostate Tissue under MRI Guidance) system by Krieger et al.(Krieger et al., 2005). This device presented a novel 2-DoF mechanism consisting of rotating sheath and steerable needle-guide for aligning the needle insertion direction to the prostate. In subsequent developments, the registration and tracking was improved (APT-II) (Krieger et al., 2011) and actuation was added (APT-III) (Krieger et al., 2013) while maintaining the basic mechanism.

The robot presented in this section is similar to the system presented in (Krieger et al., 2013) for its way in which the transrectal access is performed. Moreover, the reported device is an MRI-Safe robot and presents an additional DoF that controls the needle insertion depth. In APT systems, the needle insertion was performed manually and physician performing the insertion was fully responsible for controlling the insertion depth to match the target value computed by robot software. In the presented system, while the needle insertion is still manually performed, the insertion depth of the needle is constrained to the desired value by an actuated needle depth driver that adjusts the position of the stopper on the needle.

Additionally, the presented robot is MRI-safe while the first APT system was a passive device, and the most advanced is MRI-Conditional at best. The presented robot was entirely built of nonmagnetic and electrically nonconductive materials, is electricity free, and a control structure devised according to MRI safety considerations was used. On the other hand, as reported in (Krieger et al., 2013), APT-III system contains small aluminum and brass parts in the needle-guide, uses electro-optical encoding and actuated by piezo motor. The use of the electricity will likely exclude the MRI-Safe option, because currents generate electromagnetic waves and require wires.

Being MRI-conditional does not mean that cannot become effective clinical tools, but more comprehensive tests will be required for regulatory clearances (FDA, European Community, and other) and their application will be restricted to specified MR environments and specified conditions of use. But most importantly, the level of image interference for MRI-Safe and MRI-Conditional devices is substantially different, inherently, by the nature of the materials and energies used.

In APT-III system, the motor casing had to be placed 20 cm or more away from the prostate to reduce the susceptibility artifacts caused by metallic motor component (Krieger et al., 2013). Even so, up to 80% SNR loss is reported when the piezo motors are activated even without motion. Shielding the motor casing reduced SNR loss but it was still 40% to 60%. Alternatively, as presented in the following section, the SNR loss of the presented MRI-Safe robot is at a different order of magnitude. For example, we measured 0.1% loss due to the robot and 0.71% due to motion, values including experimental measurement errors. The SNR loss due to MRI-Safe devices may be very small, virtually zero.

Table 12 below summarizes existing researches on the devices for the MRI-guided transrectal interventions to the prostate and compares the position of the robot presented in this section with respect to the prior arts.

Table 12: Devices for MRI-guided transrectal access to the prostate

Reference	Actuation	Tracking	Validation
APT-I (Krieger et al., 2005)	Manual	Active coils.	37 clinical trials
(Beyersdorff et al., 2005) & (Engelhard et al., 2006) & (Hambrock et al., 2008)	Manual	Real time image of the needle-guide	47 clinical trials total
APT-II (Krieger et al., 2011)	Manual	Encoded joints.	57 clinical trials
(Elhawary et al., 2010)	Piezo motor	Active coils.	Phantom experiment
(Schouten et al., 2010b) & (Yakar et al., 2011)	Pneumatic turbine	Real time image of the needle-guide	10 clinical trials
APT-III (Krieger et al., 2013)	Piezo motor	Encoded piezo motors.	Phantom experiment
Presented Robot (Stoianovici et al., 2013b)	Pneumatic Step motors	Encoded step motors	Animal experiment

The scientific novelty of the research presented in this section is:

- A new MRI-Safe robot for transrectal biopsy of the prostate.

My personal contribution to this project was:

- Writing entire robot control software and image-guidance software

- Evaluating the accuracy of the robots in various setting (bench, in-vitro, in-vivo)
- Evaluating the effect of robot on MR image Signal to Noise Ratio
- Running animal experimentsin collaboration with Memorial Sloan Kettering Cancer Center

4.1.1 Structure

The entire system consists of a robot, needle depth driver, interface box, and a controller. Schematic of the entire robot system and the picture of the robot is shown in Figure 4.1,. The robot is entirely made of plastic and ceramic and actuated by pneumatic step motor (Stoianovici et al., 2007) that is actuated by air and is encoded by fiber optics connection. Hence, the robot is completely MRI-Safe and can be placed inside the scanner. On the other hand, the control electronics of the robot and the air supply is not MRI compatible and must be placed outside the scanner room. The interface box lying in between contains the piezoelectric valves that controls the air supply to the robot and optoelctrical interface that converts the encoded light signal to electrical signal. This interface box is MRI-Conditional and can be place in the scanner room but away from the scanner table. Needle depth driver that adjusts the stopper of the needle is located on top of the interface box.

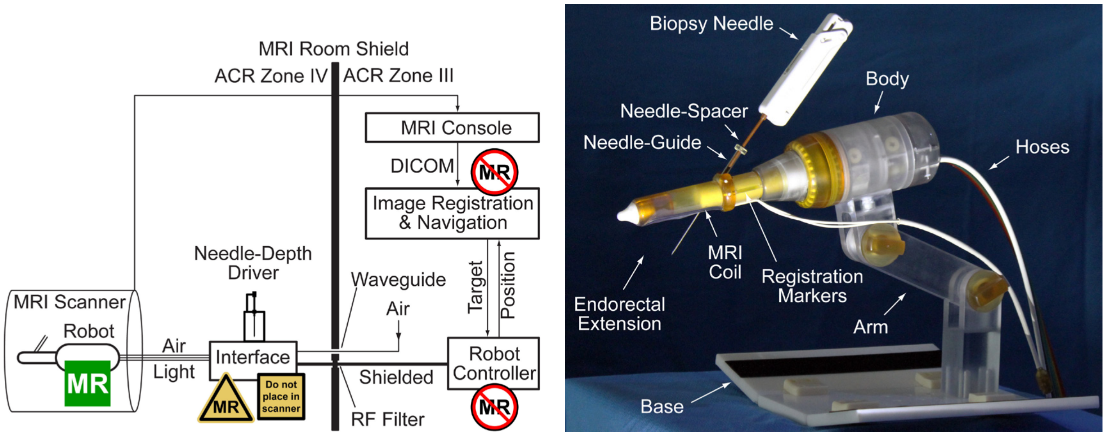

Figure 4.1: MRI-Safe robot system

4.1.2 Kinematics Analysis

The robot consists of an endorectal extension and a needle-guide. Needle-guide is constrained to rotate on a plane fixed to the endorectal extension. The rotation of the needle-guide is achieved by translating one part of the needle-guide respected to the other fixed to the endorectal extension.

The robot has 2-DoF that aligns the needle insertion direction to the target. The first degree of freedom rotates the endorectal extension about fixed robot body, to bring the target onto the plane of needle-guide rotation. Then the second degree of freedom rotates needle-guide to align the guide to the target. Needle depth driver is attached to the interface box and adjusts the position of the stopper on the biopsy needle to adjust the depth of insertion.

The kinematics of robot can be derived as follows. The robot base coordinate system $\boldsymbol{XYZ}$ is attached to the robot with $\boldsymbol{Z}$ axis aligned along the axis of the endorectal extension and lie of the needle-guide contained in the $\boldsymbol{YZ}$ plane as shown in Figure 4.2. Motor 1 rotates its output shaft with angle θ_1 and engages a harmonic transmission (ratio $H = -1/49$) that rotates the endorectal extension about the $\boldsymbol{Z}$-axis with angle $R1 = \mathrm{H}\theta_1$, where $\theta_1 = \mathrm{tr_m} \times \mathrm{step_1}$ with $\mathrm{tr_m} = 4°/\mathrm{step}$ is the transmission ratio of the motor. This rotates the center point $\boldsymbol{p_0}$of the RC joint and direction of the $\boldsymbol{Y}$ axis

$$\boldsymbol{p} = \begin{bmatrix} \cos \mathrm{R}_1 & \sin \mathrm{R}_1 & 0 \\ -\sin \mathrm{R}_1 & \cos \mathrm{R}_1 & 0 \\ 0 & 0 & 1 \end{bmatrix} \mathbf{p}_0 \text{ and } \boldsymbol{Y'} = \begin{bmatrix} \sin R_1 \\ \cos R_1 \\ 0 \end{bmatrix} \tag{4.1}$$

Now the Motor 2 translates the sliding needle-guide, adjusting the direction of the needle-guide within the $\boldsymbol{Y'Z}$ plane. The resulting needle-guide direction $\boldsymbol{v}$ is given by

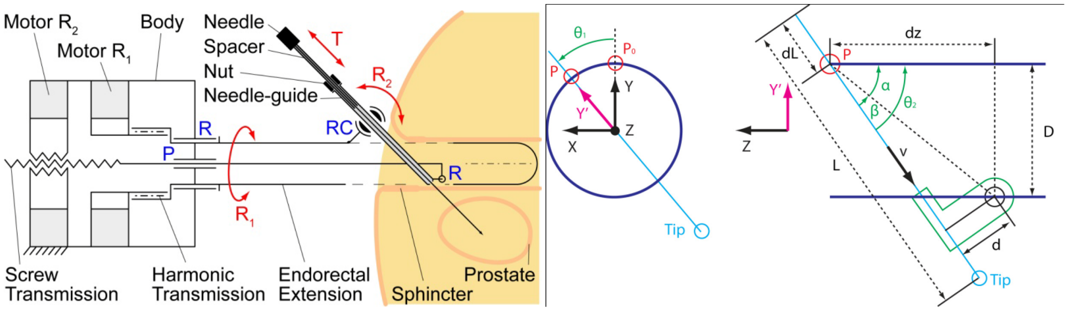

Figure 4.2: Kinematics of the robot

$$\boldsymbol{v} = -\sin \mathrm{R}_2\, \mathbf{Y}' - \cos \mathrm{R}_2\, \mathbf{Z} \tag{4.2}$$

with $\mathrm{R}_2 = \alpha + \beta$. From simple geometric analysis of Figure 4.2, the value of the α and β can be calculated as $\tan\alpha = \mathrm{D}/\mathrm{dz}$ and $\sin\beta = \mathrm{d}/\sqrt{\mathrm{dz}^2 + \mathrm{D}^2}$. D and d are constant design parameter and

$$\mathrm{dz} = \mathrm{dz}_0 + \mathrm{tr}_\mathrm{p} \times \left(\mathrm{tr}_\mathrm{m} \times \mathrm{step}_2 - \frac{\mathrm{tr}_\mathrm{h}}{360} \times \mathrm{step}_1\right) \tag{4.3}$$

is the translation of the sliding needle-guide caused by motor 1 and 2. $\mathrm{tr}_\mathrm{p} = 2.54\ \mathrm{mm}/360°$ is the pitch of the screw driving the translation. The final position of the inserted needle tip in robot coordinate as a function of the motor angles is then

$$\mathbf{p}_\mathrm{tip} = \mathbf{p} + (\mathrm{L} - \mathrm{dL})\mathbf{v} \tag{4.4}$$

where $(\mathrm{L} - \mathrm{dL})$ is a length of the needle L, adjusted by needle stopper travels distance $\mathrm{dL} = \mathrm{tr}_\mathrm{m} \times \mathrm{tr}_\mathrm{n} \times \mathrm{step}_3$ with the $\mathrm{tr}_\mathrm{n} = 0.7\ \mathrm{mm}/360°$ being the pitch of the screw on which the stopper nut translates.

The inverse kinematics is derived as follow. Given the robot coordinate of the target, $\mathbf{t} = \left[\mathrm{t}_\mathrm{x}, \mathrm{t}_\mathrm{y}, \mathrm{t}_\mathrm{z}\right]^\mathrm{T}$, the required motor steps can be calculated in the similar manner. First, by rotating motor 1, the YZ plane is rotated by $\theta_1$such that the target will be lying on the rotated plane.

$$\mathrm{step}_1 = \theta_1/(\mathrm{tr}_\mathrm{m} \times \mathrm{tr}_\mathrm{h}) \text{ and } \theta_1 = \tan^{-1} \mathrm{t}_\mathrm{y}/\mathrm{t}_\mathrm{x} \tag{4.5}$$

Once the target is on the Y'Z plane, by rotating motor 2, the direction of the needle-guide is adjusted to be aligned with the line $\overrightarrow{\mathbf{pt}}$, this determines θ_2, dz and step_2.

$$\begin{gathered}\mathbf{v} = -\sin\theta_2\, \mathbf{Y}' - \cos\theta_2\, \mathbf{Z} = \overrightarrow{\mathbf{pt}}\,/|\overrightarrow{\mathbf{pt}}\,| \\ \mathrm{dz} = (\mathrm{D}\cos\theta_2 + \mathrm{d})/\sin\theta_2 \\ \mathrm{step}_2 = \left(\frac{\mathrm{dz} - \mathrm{dz}_0}{\mathrm{tr}_\mathrm{p}} + \frac{\mathrm{tr}_\mathrm{h}}{360} \times \mathrm{step}_1\right) / \mathrm{tr}_\mathrm{m}\end{gathered} \tag{4.6}$$

Finally, required distance for the stopper to place the needle tip at the target is given by

$$dL = L - |\overrightarrow{\mathbf{pt}}| \tag{4.7}$$

The kinematics of the robot was simulated to measure the size of the workspace as shown in Figure 4.3. and the MR image of the rectum and the prostate was overlaid to the CAD model to ensure the coverage of the prostate.

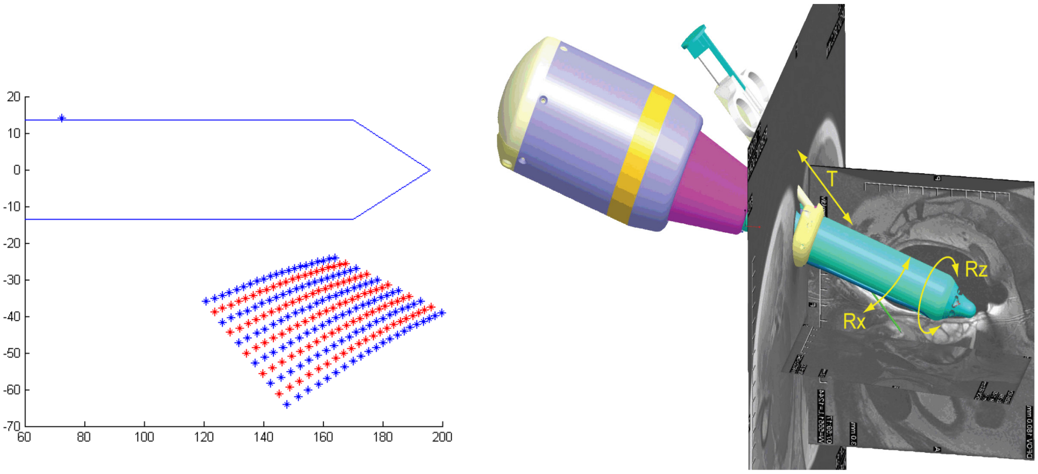

Figure 4.3: Workspace of the robot

4.1.3 Bench Test of Robot Precision and Accuracy

The accuracy and the precision of the robot were evaluated by using an optical tracker system to measure the position of a passive marker attached at the tip of the needle as shown in Figure 4.4. The center of the passive marker was located 128.9 mm from the entrance of the needle-guide.

Accuracy Measurement

Robot axis 0 (translation of the needle tip) was moved (100, 300, 500, 700, 900, 1100) steps. For each step, axis 1 (rotation of the needle) was moved (-600, -400, -200, 0, 200, 400, 600) steps. In robot coordinate system, this corresponds to translation of 2.82 to 31.04 mm along y axis and -49° to 49° rotation about y axis. This generates 42 different locations of the marker. For each location, the tracker coordinate $p_c = (x_c, y_c, z_c)$ of the marker was measured. Also, for each location, the robot coordinate $p_r = (x_r, y_r, z_r)$ of the marker was calculated from the forward kinematics of the robot.

Using the set of corresponding coordinates of the marker in camera coordinate system and robot coordinate system, transformation from the camera coordinate to the robot coordinate, ${}_{c}^{r}g$ was estimated. The registered sets of points are shown in Figure 4.5. Accuracy is calculated by calculating $|{}_{c}^{r}g\ p_c - p_r|$ for each point and averaging it. The result was $(\Delta x, \Delta y, \Delta z) = (0.0969, 0.1734, 0.0814)\ mm$ and magnitude is 0.2147 mm.

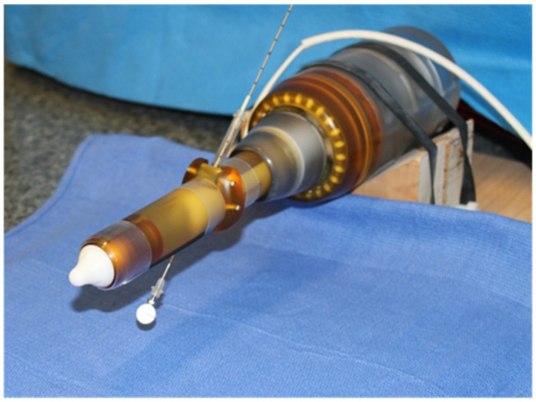

Figure 4.4: Accuracy and precision measurement

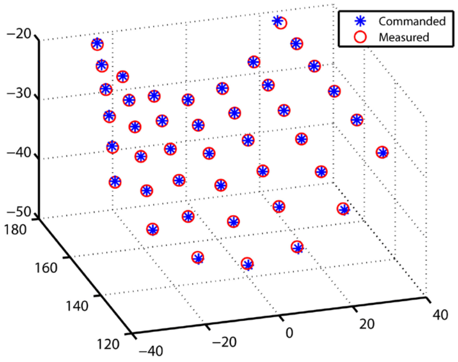

Figure 4.5: Registered robot and tracker coordinate showing the accuracy

4.1.4 MRI Compatibility Test

For the MRI safety, the device should not experience any force or torque by the magnetic field of the scanner. According to ASTM F2052, magnetically induced force on the devices can be measured by hanging the device at the entrance of the scanner bore and measuring the deflection (Schaefers, 2008). Though it was obvious that there will be no force exerted on the robot as there is no magnetic material in the robot, nevertheless, the robot was hanged by its cable at the entrance of the scanner bore as shown in Figure 4.6 to check for any noticeable deflection or oscillating motion. Video of the robot hanging at the entrance of the scanner was taken. No oscillation or deflection of the robot was observed.

In addition to safety, the device should not compromise the image quality. The effect of the robot's presence and actuation on the quality of the MR image was measured in another experiment. Two different metric, 'image deterioration factor' (Stoianovici, 2005), and SNR defined in National Electrical Manufacturers Association (NEMA) standard , was used to quantify the effect.

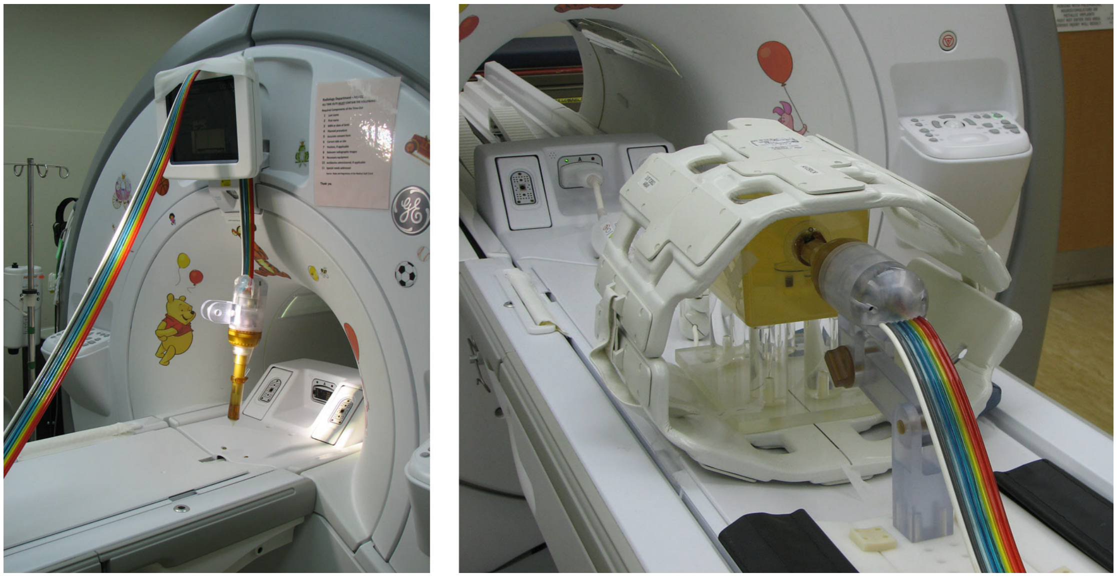

Figure 4.6: Image compatibility test

A mockup was built to simulate endorectal access to a “prostate” structure showing fine geometric patterns of lines and circles (Braino MRI test mockup). This was embedded within a gelatin base and placed in a plastic container as shown in Figure 4.6. This mockup was imaged in 3T scanner under three different conditions:

Sets NR: No Robot (mockup only), used as a reference image

Sets R: Image of the mockup with the robot in place, powered but not in motion

Set RM: Image of the mockup with the robot in motion

For each condition, two sets of image were acquired (NR1& NR2, R1 & R2, RM1 & RM2). For the consistency of the imaging condition, with or without the robot, all images have to be acquired using same imaging coil. Therefore, the built in endorectal coil was removed from the endorectal extension and pelvic coil wrapped around the mockup was used for imaging.

Image of the mockups from the experiment (Figure 4.8, Figure 4.9 and Figure 4.7) show unperceivable differences between the NR, R, and RM sets. Suggesting that robot has no influence on image quality. This is verified by quantified analysis described below.

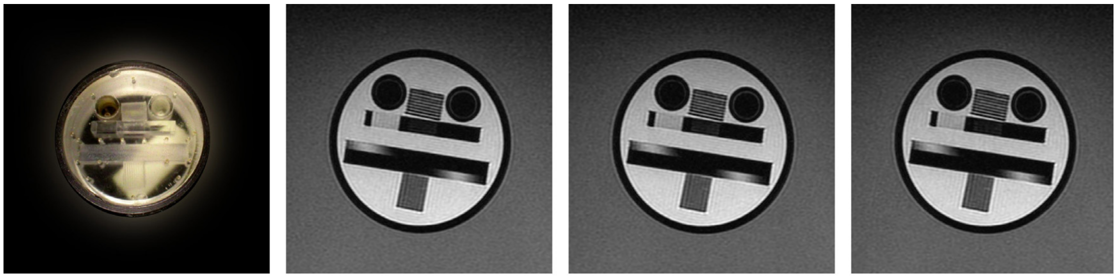

Photo No-Robot Robot Stationary Robot Moving

Figure 4.7: Image of the Mockup under different condition

Variation of the Image Deterioration Factor

Image deterioration factor quantifies the change of the image of same region under different imaging conditions. Given the pair of image (I1, I2) of same region acquired under different condition, 'image deterioration' ϵ between two images is calculated as

$$\epsilon = [\text{average of squared pixel value of I1-I2}] / [\text{range of pixel value}]^2 \text{ x } 100\ [\%] \tag{4.8}$$

The values of these measures range between 0% which corresponds to no deterioration, and 100% which corresponds to total degradation of the images.

For the calculation of the image deterioration factor, thin-section high-resolution axial image of the mockup (TR/TE = 3943/118.784 ms, Slice thickness 2 mm., Matrix 512 x 512, Scanning sequence: SE, Phase enc. direction: ROW) was acquired. Figure 4.8 shows one of the image slices and the difference images. Four different image deterioration factors ($\epsilon^{P1}, \epsilon^{P2}, \epsilon^{A1}\epsilon^{A2}$) were calculated using four different pairs of the image sets.

1) Coefficient ϵ^{P1} between two sets taken without the robot (NR1-NR2).

2) Coefficient ϵ^{P2} between two sets taken without and with the robot (NR1-R1).

3) Coefficient ϵ^{A1} between two sets taken with the robot (R1-R2).

4) Coefficient ϵ^{A2} between two sets taken with the robot and with the moving robot (R1-RM1).

These factors are plotted for each axial slice in the region containing the prostate structure (slice 4 to 36) in Figure 4.10.

The average difference between ϵ^{P2} and ϵ^{P1} over the geometric mockup gives the passive image deterioration factor E_P and, respectively, the average difference between ϵ^{A1} and ϵ^{A2} plots gives the active factor E_A. They measure how much image deterioration changes when the robot is present and activated compared to the base deterioration when the robot is not present. Their experimental values are $E_P = 2.53 \times 10^{-4}$ % and $E_A = 5.68 \times 10^{-5}$%

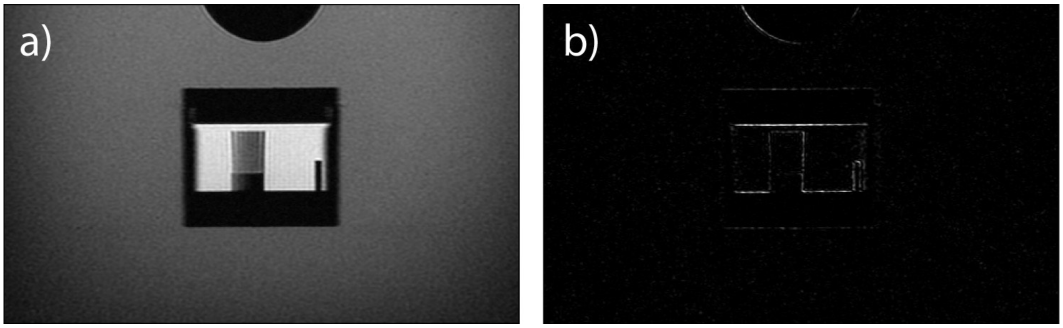

Figure 4.8: Image deterioration measurement
a) Axial image of mockup from set RM1 and
b) Difference image (R1-RM1) used for the calculation of $\boldsymbol{\epsilon^{A2}}$

Variation of the SNR measured under different circumstances.

Signal to Noise ratio is a measure for quantifying the noise level of the MRI scanner device. from an image of a mockup. According to NEMA standard , SNR is calculated as follow. From a pair of image series acquired at same condition and containing the same scan volume, one of the series is chosen as the 'reference'. SNR region of interest (SROI) is defined within the reference image. Then for each slice, difference image (the other - reference) is calculated. For each slice in the series, ‘Signal’ is calculated as the average pixel values within the SROI in reference series and the ‘'Noise' is calculated as the standard deviation of the difference image within the SROI divided by square root of 2. SNR is calculated as the Signal/Noise

To measure the effect of the robot on the SNR of the MR-imaging, thin-section high-resolution coronal image of the mockup (TR/TE = 3604/122.4 ms, Slice thickness 2 mm, Matrix 512 x 512, Scanning sequence: SE, Phase enc. direction: ROW) was acquired. Figure 4.9 shows pair of image slices and their difference image used for the SNR calculation. Three SNR were calculated from pair of images acquired under three different conditions

1) Base SNR of the imager (NR) from two sets acquired without robot (sets NR1 & NR2)

2) SNR with the robot (R) from two sets acquired with robot (sets R1 & R2)

3) SNR with the robot moving (RM) from two sets acquired with robot moving (sets RM1 & RM2)

SROI was 400 by 400 pixel area centered at [250, 250].

The relative change of the in SNR throughout the imaging volume due to the presence (R) and motion (RM) of the robot, relative to the no robot (NR) case is plotted in Figure 4.10. The graphs show very small positive and negative changes. On average, the SNR change due to the robot is –0.1% and due to its motion –0.71% (negative is loss). Since there is no reason to believe that the presence of the robot in the imaging field enhances the quality of the images, we estimate that the fluctuations shown in the graph are due to experimental measurement errors and that the SNR change is very small, virtually zero.

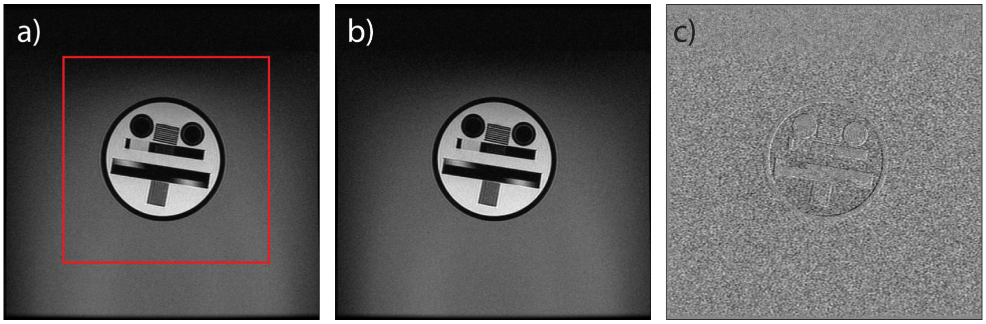

Figure 4.9: SNR measurement
a) and b) Pair of image slices from set RM1 and 2. Red rectangular indicates SROI
c) Difference image between a) and b)

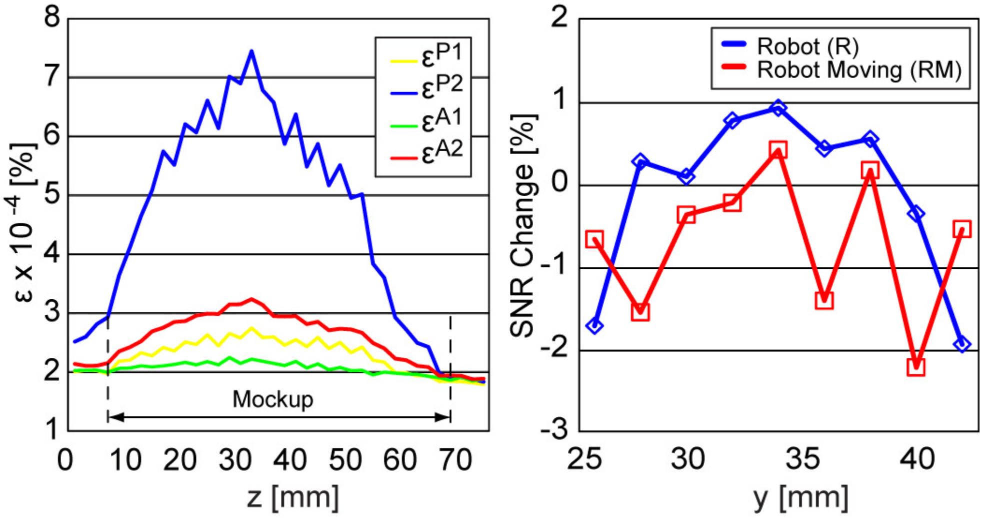

Figure 4.10: Image deterioration factor and SNR

4.1.5 Registration and Image-Guidance Accuracy Test

The robot has four registration marker made of glass tubes filled with the MRI contrast agent as shown in Figure 4.11a. These markers generates high signal in the image and can be easily segmented from the MR image of the robot by using simple isosurfacing. The CAD model of the marker is registered to the surface of the segmented marker by iterative close point algorithm.

The accuracy of the robot under image-guidance was verified in the experiment under CT image guidance. While the contrast agent is not visible in CT image, the glass tubes containing the fluid is highly visible in the CT and therefore the same registration marker can be used to register the robot in CT image.

The robot was scanned in CT scanner, the registration marker was segmented and reconstructed into 3D surface as shown in Figure 4.11b. Then the CAD model of the markers (Figure 4.11c) was registered onto the segmented surface by iterative closes point algorithm (Figure 4.11d). From the registration, transformation from image to robot coordinate ${}^{R}_{I}G$ was obtained. Then the robot was moved to position the tip of the needle to 24 locations ${}^{R}\boldsymbol{x}_i$ within the workspace. At each tip location, the robot was scanned in the CT and the image coordinate of the needle tip ${}^{I}\boldsymbol{x}_i$ was measured. The 'target registration error' (TRE) was measured by $|{}^{R}_{I}G\ {}^{I}\boldsymbol{x}_i - {}^{R}\boldsymbol{x}_i|$.

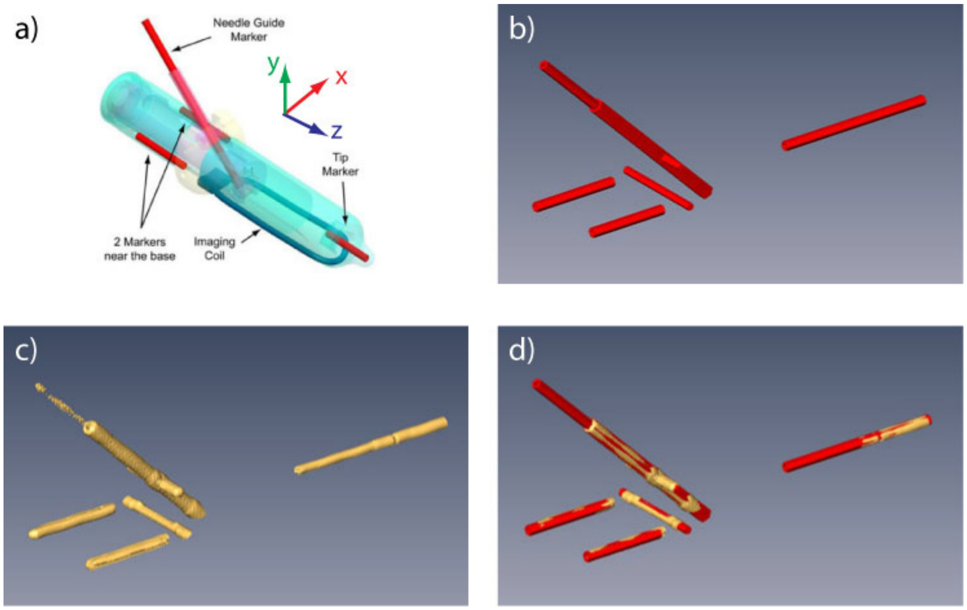

Figure 4.11: Robot registration process
a) Location of the registration marker b) Model of the registration marker
c) Segmented surface from the CT image d) Model registered to image

Table 13 below shows the summarized result. Average target registration error was 1.104 mm.

Table 13: Target Registration Error

	Δx (mm)	Δy (mm)	Δz (mm)	$\lvert {}^R_I G\ {}^I x_i - {}^R x_i \rvert$ (mm)
Mean	0.017	-0.375	-0.691	1.104
Stdev	0.642	0.499	0.274	0.331

4.1.6 Animal Experiment

In-vivo animal test was performed to evaluate the feasibility of the MRI-guided transrectal biopsy using the robot. The animal experiment was conducted at the Memorial Sloan Kettering Cancer center in New York. After obtaining Institutional Animal Care and Use Committee approval, seven male beagles were used to perform the study. The dogs were acquired when they were ~9-14 months of age, weighing between 9 and 11 kgs. The dogs were screened using ultrasound imaging and only those with a prostate that was at least 15 x 15 mm at the largest cross section were selected for use in the study.

At the beginning of the experiments, dog was anesthetized and place head first prone on 3 Tesla Signa HDxMRI scanner (GE Healthcare Systems, Schenectady, NY, USA) as shown in Figure 4.12. Foam pads and towels were used to elevate the pelvis of the animal by 20 to 30degree angle, which facilitated the placement of the robot into the rectum of the animal. The pelvic region of the dog was imaged before placing the robot into the rectum to check for any obstruction in the rectum or un ultrasoundual anatomy that will prevent the placement of the robot.

The robot was placed in the dog and T2-weighted fast spin echo images (TE:102 TR:4500 FOV: 20 Echo train length:12 ST:2 mm NEX: 2 Matrix: 256 x 256 acquired in the axial plane) were acquired to register the robot. The images were acquired using both eight-channel torso coil and the endorectal coil of the robot. Figure 4.12 shows the model of the marker registered to MR image.

After registering the robot, targets for needle placement and biopsy was selected from the same set of image. For each dog, trained interventional radiologist chose up to six targets that were equally located on either side of the urethra in the peripheral and central zone of the organ. Robot joint angle for targeting the selected location was calculated and robot was moved to align the needle-guide to the target and the stopper was adjusted.

Needle was placed into the dog and after each insertion, the prostate and the adjacent rectal region was scanned (T2-weighted fast spin echo, TE:102 TR:4500 FOV: 20 Echo train length:12 ST:2 mm NEX: 2 Matrix: 256 x 256 acquired in the axial plane) to acquire the image of the needle. In four of six dogs, prostate biopsy was performed using an 18-G, 175-mm fully automatic biopsy needle (Invivo MR18G175, Pewaukee, WI, USA) and the acquired cores were analysed for quantity and quality (diagnostic value) of the sampled tissue.

After completing the needle placement, the robot was removed and dogs were imaged to check for any damages in the rectum and were observed for 1 week to check for any unintended morbidities arising as a result of robot-assisted needle placements. . All the dogs used in the study recovered and were adopted after the observation period.

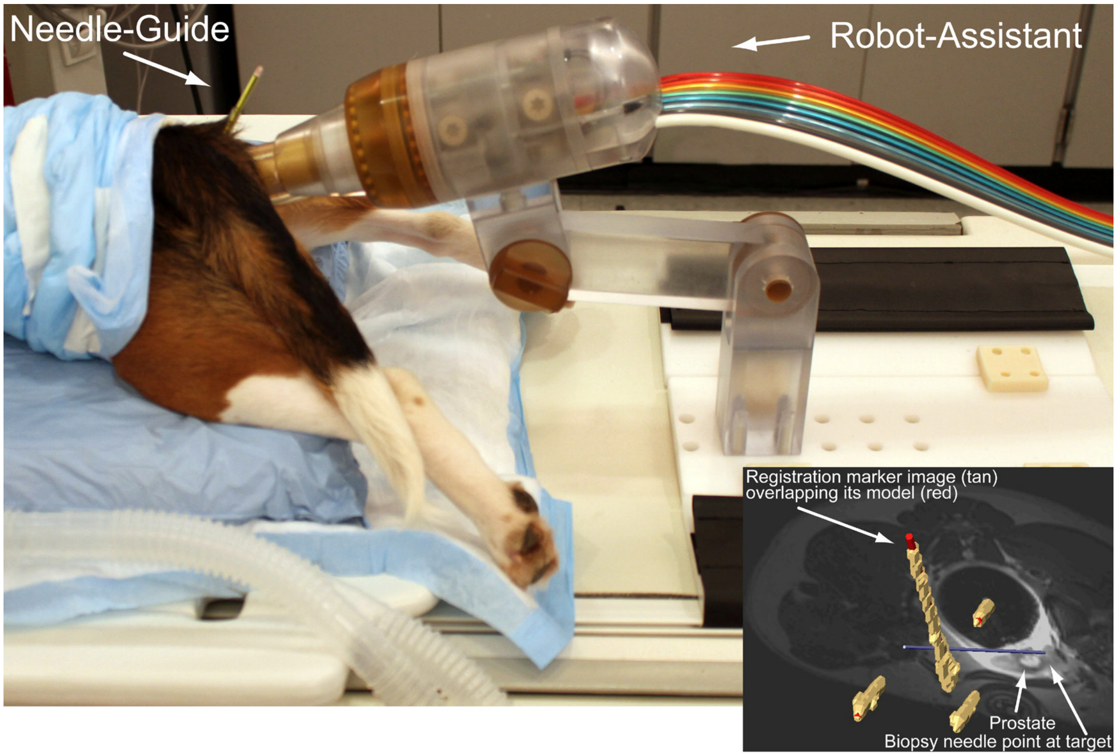

Figure 4.12: Animal test.
MRI-Safe robot placed in the dog. (Lower right) Image of the registration marker and the model of the registered needle guide

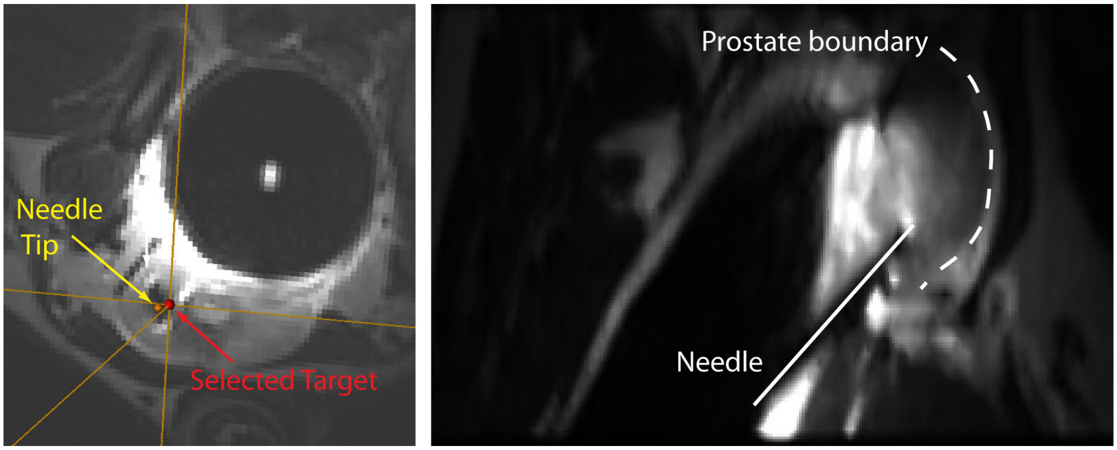

Figure 4.13: MR images from the animal experiments
a)Targeting error measurement and b) resliced image showing the needle and the prostate

Targeting error was calculated as the distance d between the image coordinate of the selected target x_1 and the image coordinate of the needle tip x_2 identified from the image acquired after each needle placement. ($d = |x_1 - x_2|$). The image coordinate of the needle tip is identified as a center of the image artifact caused by the needle tip. The accuracy and precision of targeting were then calculated as mean and SD values of the distance, respectively.

A total of 30 MRI-guided needle placements were carried out in six dogs (dog 1: six, dog 2: five, dog 3: five, dog 4: six, dog 5: four and dog 6: four needle placements) and the measured targeting accuracy was 2.58 mm (mean targeting error) and precision of 1.31 mm (SD of error). The minimum recorded placement error was 0.75 mm and the maximum recorded placement error was 5.44 mm.

4.2 MRI Guided Robot for Transperineal Biopsy

The first MRI-guided robot developed at Urology Robotics lab for brachytherapy seed placement under MR image guidance (Patriciu et al., 2007), was modified for transperineal biopsy and is currently under clinical trial for MRI-guided transperineal saturated biopsy.

Table 14 below summarizes existing research on the devices for MRI-guided transperineal biopsies to the prostate and compares the position of the robot presented in this section with respect to the prior arts.

Outside the biopsy application, a robot for transperineal access of the prostate has been used clinically in 1 patient to implant gold markers for external beam radiotherapy (van den Bosch et al., 2010) .

Table 14: Devices for MRI-guided transperineal prostate biopsy

Institution & Reference	Actuation	Features	Validations
Brigham and Women's Hospital (Dimaio et al., 2007)	Piezo motor	Open 0.5T MRI	Phantom test
Johns Hopkins (Fischer et al., 2008) & (Song et al., 2010)	Pneumatic piston	Timing belt for damping the piston servo control.	Phantom test
U of Toronto (Goldenberg et al., 2008)	Piezo motor	SNR loss with motor activation.	Phantom test
Worcesetr Polytech (Su et al., 2011)	Piezo motor	Fiber optic force sensing.	Phantom test
Presented robot	Pneumatic Step motor	MRI-Safe	FDA clearance. Clinical trial.

The scientific novelty of the research presented in this section is:

- A new MRI-Safe robot for transperineal biopsy of the prostate.
- Clinical trial of the robot.

The robot used in this project is based on the MRI-guided robot from the Urology Robotics lab reported in (Patriciu et al., 2007), with the end effector modified for biopsy. Urologist Dr. Mohamad Allaf and radiologist Dr. Katarzyna Macura were the clinical partner of this project. My personal contribution to this project was:

- Writing robot control software and image-guidance software
- Evaluating the accuracy of the robot in direct and inverse targeting experiments
- Participating in the clinical trial as a software operator.

4.2.1 Structure and Kinematics

The kinematic structure of the robot is shown in Figure 4.14. The robot consists of a needle slider above the base plate supported by 5 prismatic joint legs whose length L_i is adjusted by the pneumatic motors. This forms a Stewart platform mechanism variant, having 5 legs instead of 6. By changing the length of the legs, the orientation and the translation of the needle slider can be adjusted towards the target. Since the rotational DoF about the needle is irrelevant, 5-DoF is sufficient for positioning and orienting the needle.

The needle slider has 1-DoF that moves the slider along the needle insertion direction to adjust the position of the 'stopper' which locks the biopsy gun in place and thereby controls the insertion depth of the needle. The base coordinate system of the robot and the tool coordinate system are defined such that they coincide at zero joint angles, with z axis along the needle insertion direction.

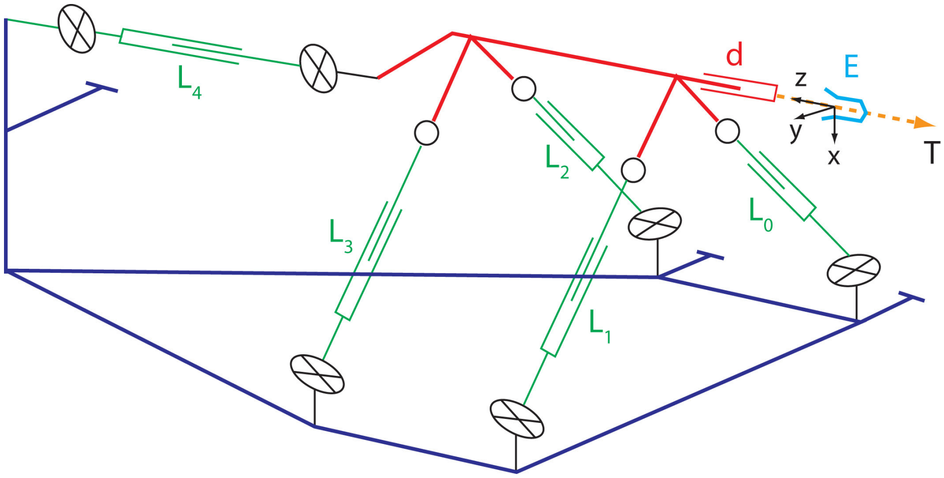

Figure 4.14: Kinematic structure of the MRI robot for transperineal biopsy
Base (blue), needle slider (red) and legs (green)

Inverse kinematics

The planned clinical application of the robot is 'saturation prostate biopsy'. This procedure involves sampling of many biopsy cores by the needle insertion through the perineum. To minimize the invasiveness of the procedure, it will be desirable to sample multiple targets through the single entry point on the perineum skin. Thus, the needle insertion direction will 'pivot' about the entry point to access target. In view of the robot, this implies that the nozzle of the robot through which the needle leaves will be placed at the entry point and maintained constant while the orientation and the insertion depth of the needle is adjusted to the target.

According to this scheme, the configuration of the robot tool coordinate system G = $\begin{bmatrix} R & \vec{\mathbf{t}} \\ 0 & 1 \end{bmatrix}$ will be determined by the selected skin entry point $\vec{\mathbf{E}}$, on which the robot will pivot the nozzle, and the target point $\vec{\mathbf{T}}$. The translation $\vec{\mathbf{t}}$ of the tool coordinate system must be the one that brings the nozzle to the skin entry point $\vec{\mathbf{E}}$ and therefore

$$\vec{\mathbf{t}} = \vec{\mathbf{E}} \tag{4.9}$$

The orientation of the tool coordinate system R must be one that aligns the needle direction $\vec{\mathbf{z}} = [0,0,-1]^{\mathrm{T}}$ to the direction of the line from the entry point to the target. By parametrizing the rotation R into XYZ Euler angles and using the fact that the direction of $\vec{\mathbf{z}}$ is invariant under rotation about z axis, we have

$$R \cdot \vec{\mathbf{z}} = R_x(\alpha) R_y(\beta) R_z(\gamma) \cdot \vec{\mathbf{z}} = \frac{\vec{\mathbf{T}} - \vec{\mathbf{E}}}{\left|\vec{\mathbf{T}} - \vec{\mathbf{E}}\right|} = \vec{\boldsymbol{l}} \tag{4.10}$$

$$R_x(\alpha) R_y(\beta) \cdot \vec{\mathbf{z}} = \begin{bmatrix} \cos\beta & 0 & \sin\beta \\ \sin\alpha\sin\beta & \cos\alpha & -\sin\alpha\cos\beta \\ -\cos\alpha\sin\beta & \sin\alpha & \cos\alpha\cos\beta \end{bmatrix} \cdot \vec{\mathbf{z}} = \begin{bmatrix} -\sin\beta \\ \sin\alpha\cos\beta \\ -\cos\alpha\cos\beta \end{bmatrix} = \begin{bmatrix} \mathrm{l_x} \\ \mathrm{l_y} \\ \mathrm{l_z} \end{bmatrix} \tag{4.11}$$

Therefore, from the specified skin entry point $\vec{\mathbf{E}}$ and target location $\vec{\mathbf{T}}$, resulting configuration of the tool coordinate system G is

$$R = R_x(\alpha) R_y(\beta), \vec{\boldsymbol{t}} = \vec{\boldsymbol{E}}, \qquad \alpha = \mathrm{asin}(-l_x)\ \ \beta = \mathrm{atan}\left(-\,l_y/l_z\right) \tag{4.12}$$

Once the configuration G = $\begin{bmatrix} R & \vec{\mathbf{t}} \\ 0 & 1 \end{bmatrix}$ is determined, the joint angles (leg length) required to achieve the configuration is determined by inverse kinematics. The inverse kinematics of the robot, which is 5-DoF Stewart platform, can be simply calculated from geometric constraints. Given the tool coordinate of the each i^{th} leg's platform end ${}^{T}\vec{\boldsymbol{q}}_i$ and robot coordinate of the each leg's base end ${}^{R}\vec{\boldsymbol{p}}_i$, the constraint on the link length is

$$\mathrm{L_i} = \left|R\,{}^{T}\vec{\boldsymbol{q}}_i + \vec{\mathbf{t}} - {}^{R}\vec{\boldsymbol{p}}_i\right| \quad \mathrm{i} = 0 \ldots 4 \tag{4.13}$$

which can be solved for given the R and $\vec{\mathbf{t}}$ to determine the length of each joint $\mathrm{L_i}$.

After the length of each leg is adjusted, the translation distance d of the slider to set the desired insertion depth is determined from the needle length and the distance from the stopper to the target by

$$\text{d = Distance from stopper to the target - Needle length} \tag{4.14}$$

Robot - Forward kinematics

While the inverse kinematic of the robot is straightforward as it is usually in the parallel robot, the forward kinematic which relates given link length to resulting configuration of the tool coordinate system, is less trivial. Typical forward kinematics of the Stewart platform is known to have up to 40 closed form solutions. As a result, instead of trying to obtain closed form solution, the forward kinematic of the robot is estimated by numerically solving the link length constraint equation.

The link length constraint equation $\mathrm{F}(\vec{\boldsymbol{x}}) = [\mathrm{L}_1^2, \mathrm{L}_2^2 \ldots \mathrm{L}_5^2]^{\mathrm{T}}$ is function of 5 parameters, $\vec{\boldsymbol{x}} = [\alpha, \beta, \mathrm{t_x}, \mathrm{t_y}, \mathrm{t_z}]^{\mathrm{T}}$. For each i^{th} leg

$$\mathrm{F_i}(\alpha, \beta, \mathrm{t_x}, \mathrm{t_y}, \mathrm{t_z}) = \mathrm{L_i^2} = \left\| \begin{bmatrix} \cos\beta & 0 & \sin\beta \\ \sin\alpha\sin\beta & \cos\alpha & -\sin\alpha\cos\beta \\ -\cos\alpha\sin\beta & \sin\alpha & \cos\alpha\cos\beta \end{bmatrix} \cdot {}^{T}\vec{\boldsymbol{q}}_i + \begin{bmatrix} \mathrm{t_x} \\ \mathrm{t_y} \\ \mathrm{t_z} \end{bmatrix} - {}^{R}\vec{\boldsymbol{p}}_i \right\|^2 \tag{4.15}$$

Given the $\mathrm{L_i}$'s, we solve the equation $\mathrm{F_i}$ numerically by Newton's method to find the solution, $\vec{\boldsymbol{x}} = [\alpha, \beta, \mathrm{t_x}, \mathrm{t_y}, \mathrm{t_z}]^{\mathrm{T}}$. Starting from the initial estimate of the solution $\vec{\boldsymbol{x}}_0 = [\alpha, \beta, \mathrm{t_x}, \mathrm{t_y}, \mathrm{t_z}]^{\mathrm{T}}$ obtained from the current joint angles, solution is updated by

$$\vec{\boldsymbol{x}}_{n+1} = \vec{\boldsymbol{x}}_n - \left[\frac{\partial \mathrm{F}}{\partial \vec{\boldsymbol{x}}_n}\right]^{-1} \mathrm{F}(\vec{\boldsymbol{x}}_n) \tag{4.16}$$

where $\left[\frac{\partial \mathrm{F}}{\partial \vec{x}_n}\right]$ is a Jacobian of the constraint equation given by

$$\left[\frac{\partial \mathrm{F}}{\partial \vec{\boldsymbol{x}}_n}\right]_i = \left[\frac{\partial \mathrm{F_i}}{\partial \alpha} \quad \frac{\partial \mathrm{F_i}}{\partial \beta} \quad \frac{\partial \mathrm{F_i}}{\partial \vec{\mathbf{t}}}\right] \tag{4.17}$$

with

$$\frac{\partial \mathrm{F_i}}{\partial \alpha} = 2\left(\vec{\mathbf{t}} - {}^{R}\vec{\boldsymbol{p}}_i\right)^{\mathrm{T}} \begin{bmatrix} 0 & 0 & 0 \\ \cos\alpha\sin\beta & -\sin\alpha & -\cos\alpha\cos\beta \\ \sin\alpha\sin\beta & \cos\alpha & -\sin\alpha\cos\beta \end{bmatrix} {}^{T}\vec{\boldsymbol{q}}_i \tag{4.18}$$

$$\frac{\partial \mathrm{F_i}}{\partial \beta} = 2\left(\vec{\mathbf{t}} - {}^{R}\vec{\boldsymbol{p}}_i\right)^{\mathrm{T}} \begin{bmatrix} -\sin\beta & 0 & \cos\beta \\ \sin\alpha\cos\beta & 0 & \sin\alpha\sin\beta \\ -\cos\alpha\cos\beta & 0 & -\cos\alpha\sin\beta \end{bmatrix} {}^{T}\vec{\boldsymbol{q}}_i \tag{4.19}$$

$$\frac{\partial \mathrm{F_i}}{\partial \vec{\mathbf{t}}} = 2\vec{\mathbf{t}} + 2\mathrm{R} \cdot {}^{T}\vec{\boldsymbol{q}}_i - 2\,{}^{R}\vec{\boldsymbol{p}}_i \tag{4.20}$$

4.2.2 Registration of the Robot to MR Image

In order to access targets selected from the MR image, the robot has to be registered to the image. That is, the orientation and translation of the robot coordinate system must be identified with respect to the coordinate system of the MR image.

Registration requires an object whose geometry can be well identified with respect to both image and robot coordinate systems. For this, a registration marker was built and mounted on the robot as shown in Figure 4.15a. The marker consists of 5 segments - two straight markers ‘Left ‘(L) and ‘Right’ (R) marker on each side, one ‘Ellipse’ (E) marker on the surface, one ‘Arc’ (A) marker on the front and one straight

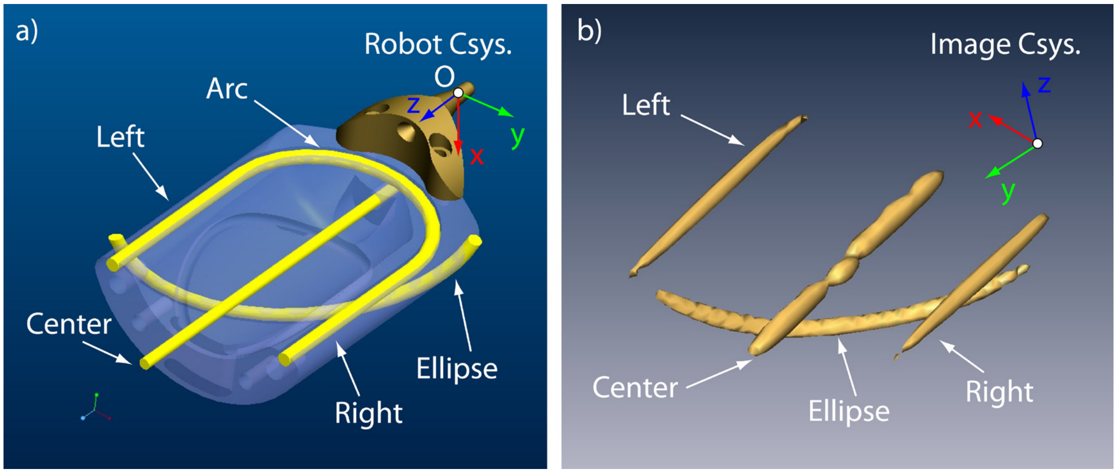

Figure 4.15: Registration marker
a) Model and b) Segmented image

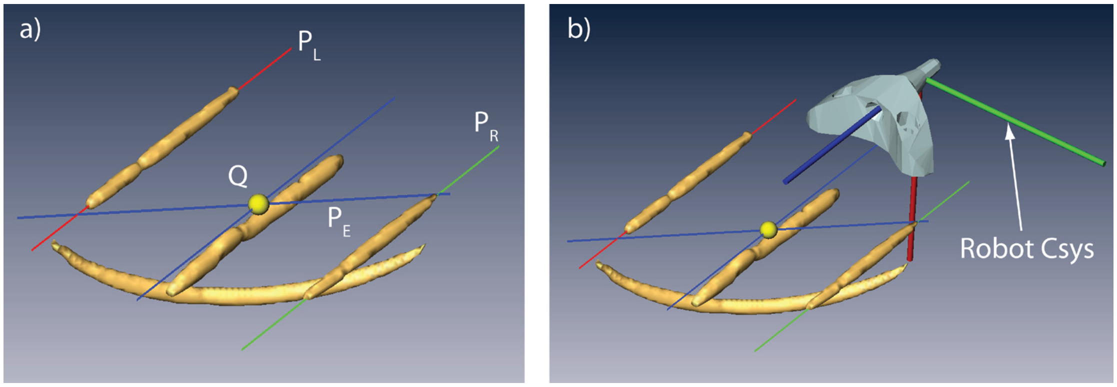

Figure 4.16: Registration Process
a) Lines fitted to the segmented image b) Model registered to the image

marker in the center (C). These markers are accurately assembled in accordance with their design so that the geometric features defined from these markers have precisely known coordinates in the robot coordinate system. Also, each segment is filled with liquid MRI contrast agent, making it highly visible in MR image as shown in Figure 4.15b.

The registration is performed using the MR image of the markers. First, each marker is segmented from the image by thresholding and image coordinate of the points on each marker are collected in sets. Both markers '***L'*** and '***R'*** are parallel to the **Z** axis and lies on the define **YZ** plane of the robot coordinate system. Hence, by fitting a line and plane **P** to the points in the marker L and R, the direction of **Z** axis and **X** axis (normal of **YZ** plane) of the robot in in image coordinate is determined. With the direction of **X** and **Z** axis determined, the orientation of the robot coordinate system in image coordinate system is fully determined.

To determine the translation of the robot coordinate system, points on the markers '***L***', '***R***' and '***E***' are projected to the plane **P** and fitted to the lines $\vec{\mathbf{P}}_{\mathrm{L}}$, $\vec{\mathbf{P}}_{\mathrm{R}}$, and $\vec{\mathbf{P}}_{\mathrm{E}}$, respectively. Then coordinate of the point **Q** - the intersection of $\vec{\mathbf{P}}_{\mathrm{E}}$ with the bisection of $\vec{\mathbf{P}}_{\mathrm{L}}$ and $\vec{\mathbf{P}}_{\mathrm{R}}$ - is identified. The coordinate of the point **Q** in robot coordinate is known to be $[15,0,72]$ in robot coordinate system. This defines the translation of the robot coordinate system.

4.2.3 Image-Guided Targeting Experiments

The accuracy of the image-guided needle targeting was evaluated through Reversed and Direct targeting experiment. In reversed targeting experiment, the robots were targeted to digital coordinate, and then its location was marked and imaged. In direct targeting experiment, the robot targeted the center of the ring targets in the mockup.

Reversed targeting experiment

The robot and the gelatin mockup was mounted rigidly on a fixture as shown in Figure 4.17a so that the relative position and the orientation between the robot and the mockup is maintained constant throughout the experiment. The robot was commanded to 8 different targets defined by the entry point and the target point (Table 15) and the trajectory of the needle to the commanded target in robot coordinate system (${}^{R}\vec{\mathrm{p}} + \lambda\,{}^{R}\vec{\mathrm{L}}$) was calculated from the kinematics.

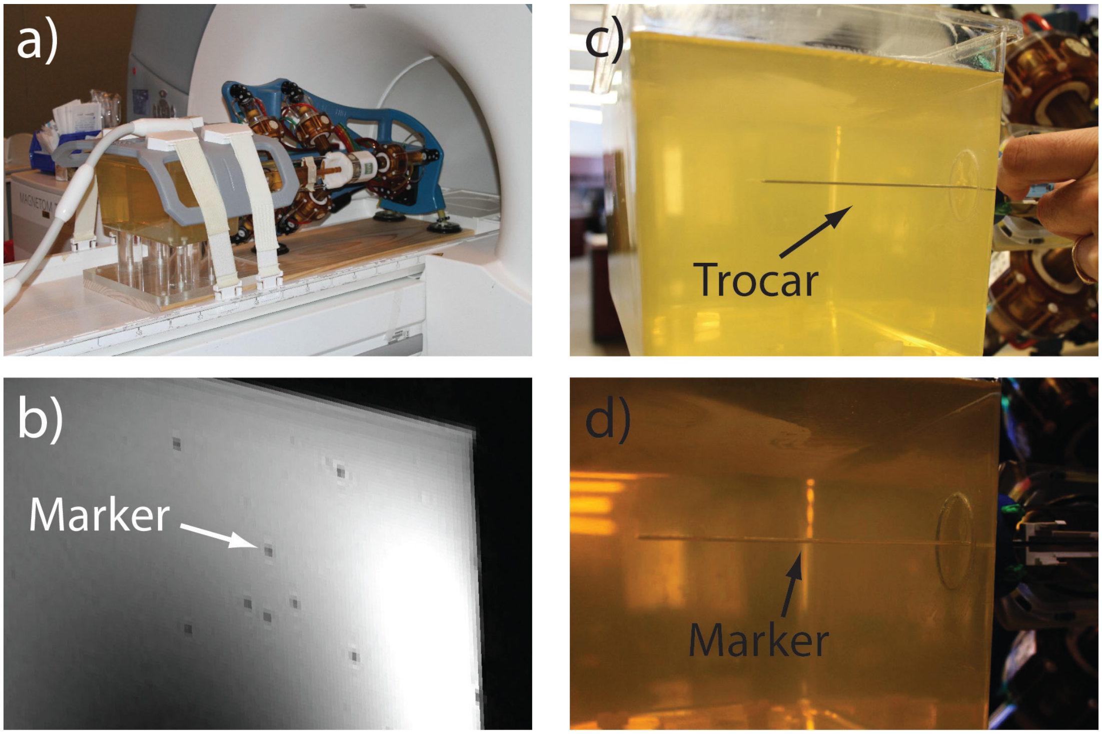

Figure 4.17: Reversed targeting experiment

At each location, 18G trocar needle was inserted through the guide. To mark the trajectory of the needle, a needle trajectory marker (124 mm long angel hair spaghetti noodle) was placed inside the gelatin through the trocar (Figure 4.17c and d). Diamond tip trocar needle was used for target 2, 3, 4 and beveled tip trocar needle was used for the rest.

After all 8 markers were placed, the robot and the mockup (now containing spaghetti noodle) fixture was transported to the MRI scanner room and imaged (Figure 4.17a). Robot was first scanned to image the registration marker and then the gelatin mockup to image the implanted trajectory markers.

From the image of the registration marker, the robot was registered to the MR image coordinate system. The commanded trajectories (${}^{R}\vec{\mathrm{p}} + \lambda\, {}^{R}\vec{\mathrm{L}}$) were transformed to image coordinate system (${}^{I}\vec{\mathrm{p}} + \lambda\, {}^{I}\vec{\mathrm{L}}$) using the registration.

MR image of the trajectory marker (Figure 4.17b) was manually segmented to reconstruct the actual trajectory of the needle. The commanded trajectory ${}^{I}\vec{\mathrm{p}} + \lambda\, {}^{I}\vec{\mathrm{L}}$ and the reconstructed trajectory markers were displayed and the distance between them were measured.

Table 15: Reverse targeting result

#	Commanded Entry (mm)			Commanded Tip (mm)			${}^{R}\vec{\boldsymbol{p}}$	${}^{R}\vec{\mathrm{L}}$
	X	Y	Z	X	Y	Z		
1	0	0	0	0	0	-122	[0, 0, 0]	[0, 0, -1]
2*	0	5	0	0	5	-122	[0, 5, 0]	[0, 0, -1]
3*	0	-5	0	0	-5	-122	[0, -5, 0]	[0, 0, -1]
4*	5	0	0	5	0	-122	[5, 0, 0]	[0, 0, -1]
5	10	10	0	20	20	-122	[10, 10, 0]	[0.0814, 0.0814, -0.9933]
6	-10	10	0	-20	20	-122	[-10, 10, 0]	[-0.0814, 0.0814, -0.9933]
7	10	-10	0	20	-20	-122	[10, -10, 0]	[0.0814, -0.0814, -0.9933]
8	-10	-10	0	-20	-20	-122	[-10, -10, 0]	[-0.0814, -0.0814, -0.9933]

* The diamond tip trocar needle was used. Bevel tip trocar needle was used otherwise

Reversed targeting results

Table 15 shows the commanded needle trajectories $\vec{\mathrm{p}} + \lambda\vec{\mathrm{L}}$ (in robot coordinate system) defined by the position of the nozzle and the inserted needle tip in robot coordinate system.

Figure 4.18 shows a trajectory markers inserted in the gelatin box. It can be seen that the trajectory of the beveled tip trocar needle is much more deflected compared to that of the diamond tip trocar. Since the biopsy needles typically have beveled tip, it can be expected that the needles will deflect during the biopsy. Therefore, the trajectory of the beveled tip needle insertion (all targets except target 2, 3, 4) was used to model the needle bending and the trajectory of the diamond tip needle insertion, which has lesser error from deflection, was used to quantify the image-guided targeting accuracy.

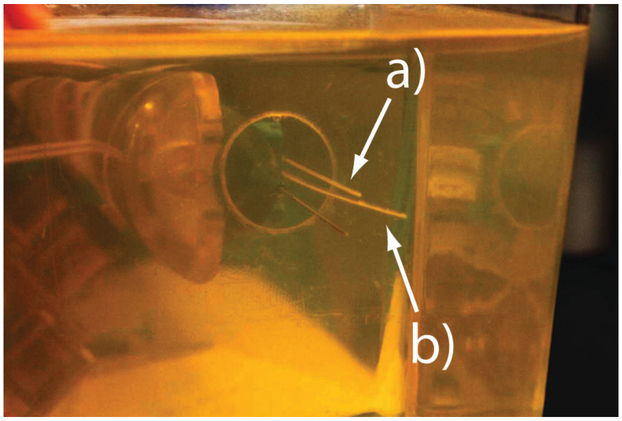

Figure 4.18: Trajectory of a) diamond tip and b) bevel tip needle

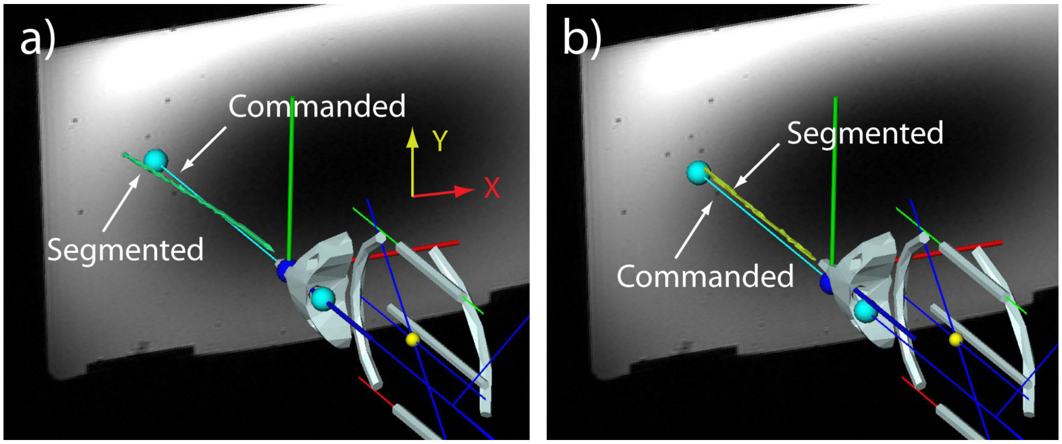

Figure 4.19: Commanded and Actual trajectory from
a) Beveled tip needle and b) Diamond tip needle.

Figure 4.19 shows the graphical representation of commanded needle trajectory and actual trajectory reconstructed from MR image for beveled needle and diamond tip needle. It can be seen that the actual trajectory needle bends toward for the beveled tip needle. The distance between the commanded and actual trajectory in two orthogonal directions to the needle (X and Y axis of the robot) was measured as shown in Figure 4.20. The distance between the actual and commanded trajectory were about 1 mm and 3 mm in robot's X and Y axis direction.

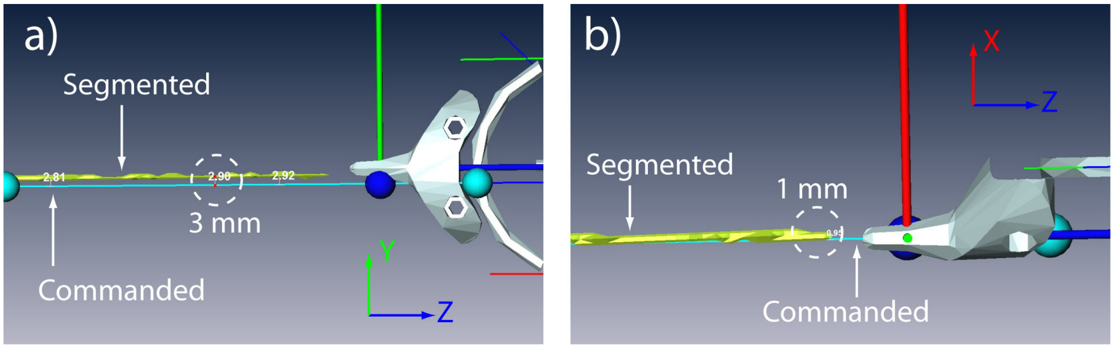

Figure 4.20: Measurement of error in direction of Y and X axis of the robot

The explanation is that the image of the trajectory was shifted from its real position due to the image artifacts. It is known that the position of a material inside the tissue can shift in the MR image due to the susceptibility error (Schenck, 1996). The magnitude of the shift is proportional to the difference of magnetic susceptibility of the material and the water and appears only in the direction of frequency encoding in the image. The frequency encoding direction in the images of the trajectory marker was in Y direction, which was also the direction with the highest error.

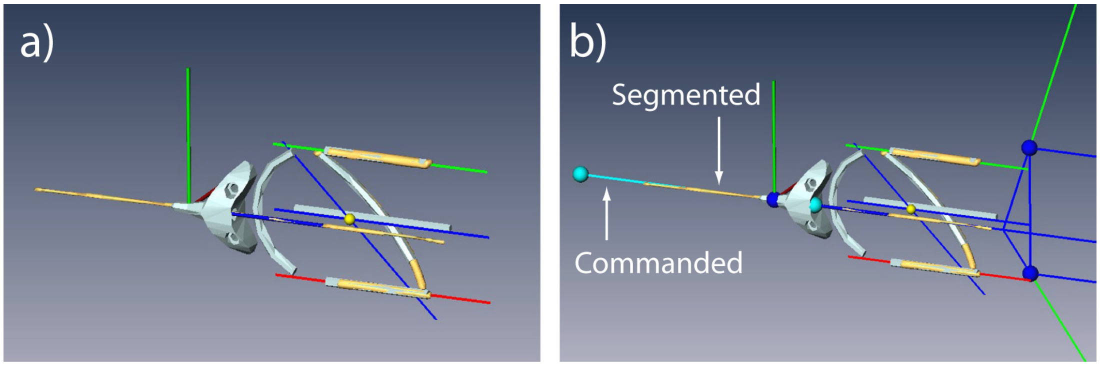

Figure 4.21: CT-guided reversed targeting

To confirm the hypothesis above, a reverse targeting experiment was repeated in CT image-guidance, to remove the possible error from the imaging artifact. The registration markers were filled with the CT contrast and the robot was imaged in CT with the biopsy needle on it. The robot was registered to the CT image and the trajectory of the needle registered to the CT image was compared with CT image of the needle, as shown in Figure 4.21.

As can be seen, the model and the actual trajectory exactly overlap on top of the other with almost no perceivable error. This rule out the possibility that the error observed in MRI-guided reverse targeting experiment was originating from the errors in dimensions, kinematics or registration algorithms, suggesting the observed error in MRI was indeed coming from the image artifact.

Direct targeting experiment

Target to be used in the test is 3 by 3 array of 9 rings filled with the liquid MRI contrast agent. This target was embedded in the gelatin box. The robot and the gelatin mockup was mounted rigidly on a fixture and installed on the MRI scanner and the robot and the targets were imaged.

The robot was registered to the image and the center of each ring was targeted using the image guidance software. At each target, 18G trocar needle was used to implant the needle trajectory marker as it was done in the reverse targeting test. Diamond tip needle was used to target ring 4, 5 and 6, beveled tip needle was used to target the rest. For the bevel tip needle, anticipated needle deflection based on the model was used for targeting.

After all 9 rings were targeted, MR image of the gelatin mockup was acquired. The actual trajectory of the needle was reconstructed from the MR image. The distance from the center of each ring to the intersection between the needle trajectory and the ring was measured.

Direct targeting results

The coordinates of 1) the center of the 9 ring targets, and 2) the intersection between the needle trajectory and the ring, were measured from the image as shown in Figure 4.22 and the distance between the center and the intersection was calculated. Table 16 and Table 17 show the result measured in image coordinate for the rings targeted using a bevel tip needle and a diamond tip needle, respectively.

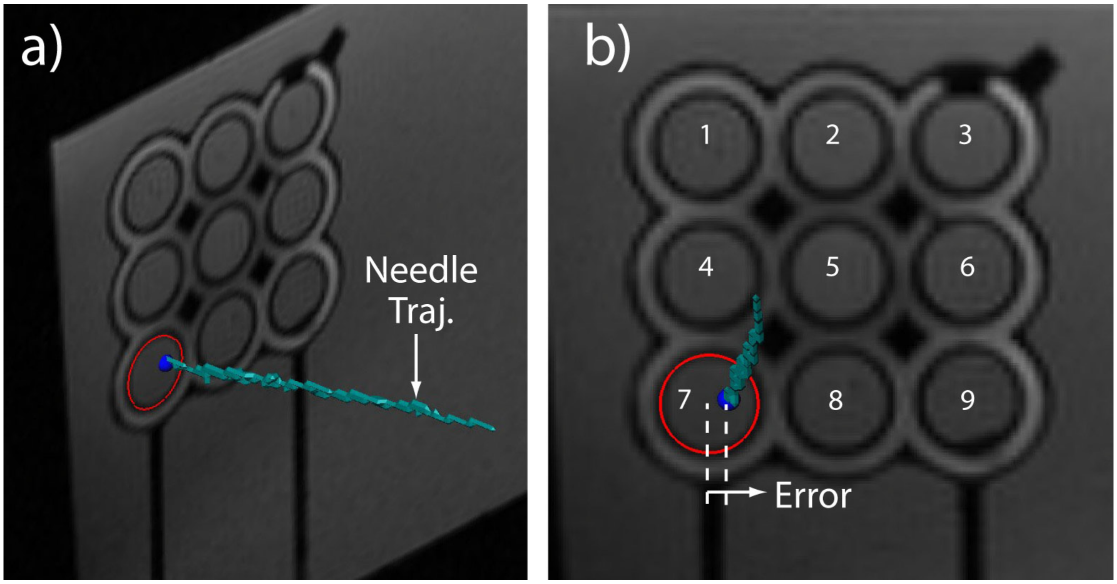

Figure 4.22: Measurement of the ring center and the intersection of the ring and trajectory

Table 16: Direct targeting using beveled tip needle

	Ring Center (mm)			Intersection (mm)			Distance (mm)			
Ring #	X	Y	Z	X	Y	Z	|ΔX|	|ΔY|	|ΔZ|	Norm
1	-84.67	123.32	-51.49	-85.77	123.82	-51.56	1.10	0.50	0.07	1.21
2	-85.17	103.42	-51.12	-84.77	104.22	-51.11	0.40	0.80	0.01	0.89
3	-85.27	83.73	-50.73	-85.97	84.43	-50.79	0.70	0.70	0.06	0.99
7	-45.34	122.97	-49.14	-46.14	119.57	-49.12	0.80	3.40	0.02	3.49
8	-45.74	102.87	-48.76	-48.34	101.07	-48.88	2.60	1.80	0.12	3.16
9	-45.84	82.87	-48.37	-50.13	80.87	-48.59	4.29	2.00	0.22	4.74
Avg.							1.65	1.53	0.08	2.41
Std.							1.51	1.10	0.08	1.61

Table 17: Direct targeting using diamond tip needle.

	Ring Center (mm)			Intersection (mm)			Distance (mm)			
Ring #	X	Y	Z	X	Y	Z	|ΔX|	|ΔY|	|ΔZ|	Norm
4	-65.01	123.24	-50.32	-66.30	123.34	-50.40	1.29	0.10	0.08	1.30
5	-65.51	103.35	-49.95	-70.80	102.24	-50.24	5.29	1.11	0.29	5.41
6	-65.70	83.45	-49.93	-71.99	83.14	-49.93	6.29	0.31	0.00	6.31
Avg.							4.29	0.51	0.12	4.34
Std.							2.65	0.53	0.15	2.67

For all 9 trajectories, as can be seen in the Figure 4.23, the actual trajectory has some offset from the calculated trajectory in +Y direction in robot coordinate system (X direction in image coordinate). Similar phenomenon was observed during the inverse targeting test. Again this is due to the susceptibility artifact in frequency encoding direction.

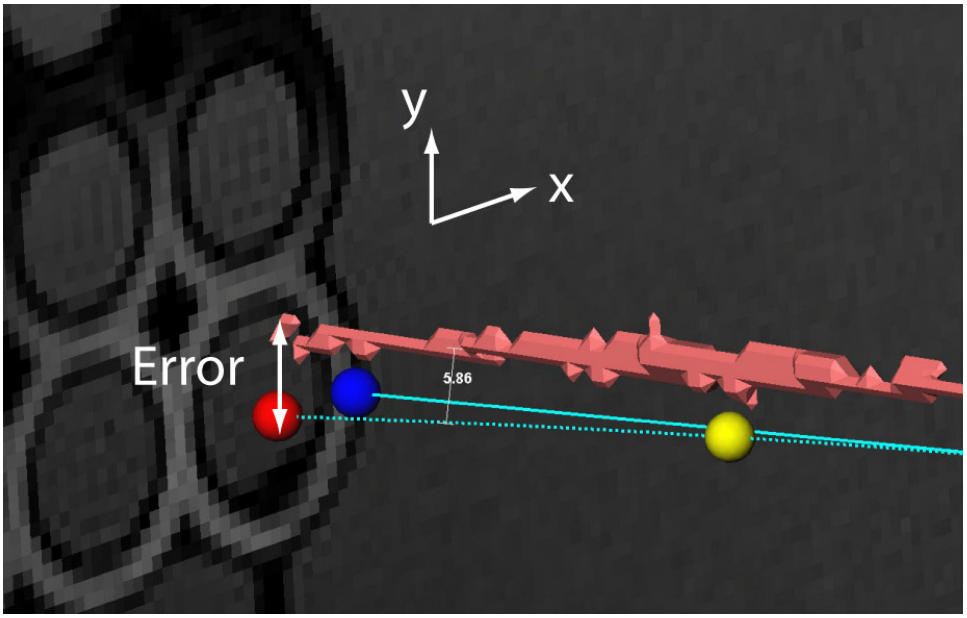

Figure 4.23: Direct Targeting Error

4.3 In-vitro Test and Clinical Trial

The FDA agreed that the robotic device is safe to use in any MR environment, is not influenced by the MR environment, and does not interfere with the functionality of the imager. Based on experimental data and scientific rationale the FDA agreed that the robotic device is MRI-Safe according to ASTM F2503 and allowed it to be labeled accordingly. This is an item that poses no known hazards in all MR environments.

The first biopsy case has been performed. Biopsy samples were acquired in the MRI scanner under direct MRI guidance assisted by the device. Figure 4.24 shows the patient in the MRI scanner and the robot placed on position next to the patient to access the perineal site for biopsy. The patient tolerated the procedure well with no complications and no subsequent adverse events.

The device represents the first FDA cleared robot for the MR environment. This has been facilitated by the MRI-Safe technology. A few passive and remote controlled devices have been developed and successfully used in the MRI for prostate biopsy. To the best of our knowledge this case represents the first-in-man robot-assisted direct MRI-guided prostate biopsy. This first experience suggests that robotic biopsy may be safe and feasible, and next cases are being scheduled.

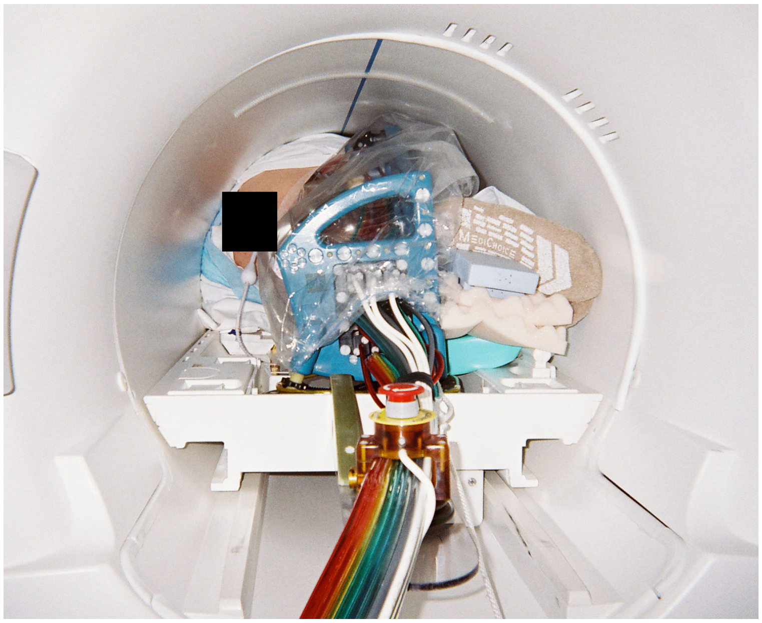
[redacted]

Figure 4.24: Patient and the MRI-Safe robot in the scanner for the first clinical trial

5 Conclusion

Image-guided robots integrate the information from medical images with computer controlled accuracy and precision of the robots to enable more precise planning and execution of the interventional procedures. This dissertation presents the development of several ultrasound and MRI-guided robots and their applications in urology.

A robotic ultrasound probe manipulator was developed for abdominal (TRUS1-Robot) and transrectal ultrasound probes (TRUS2-Robot). Both robots consist of a Remote Center of Motion (RCM) module and a probe driver that implements 3 rotational degree of freedom for TRUS1-Robot and 3 rotational + 1 translational DoF for the TRUS2-Robot. Mechanical performances of the manipulator, accuracy, precision and the stability of the RCM were verified using an optical tracker.

Several engineering problems that needed to be solved to convert the manipulators to ultrasound image-guided robots are addressed. The ultrasound image and the needle-guide were registered to the robot coordinate system through a calibration procedure using a planar calibration rig. The calibration procedure presents a novel method of formulating and optimizing the constraints of the planar rig. Scale, orientation and offset components of the calibration parameters are optimized in separate problems, and nonlinear optimization of the orientation component is solved by linearizing the constraints using matrix exponentials. The accuracy of the calibration and image-guided targeting using the calibrated probe was verified in in-vitro experiment.

With the calibrated probe, image slices can be collected with their configuration in space to generate 3D volume images. A new algorithm for filling the 3D volume from an acquired set of image slices was developed. The algorithm speeds up the filling process by partitioning the volume in octree and sorting the slices. A new algorithm for segmenting the acquired 3D volume image by combining the previous art of using non-orthogonal reslicing and probabilistic edge tracking method was developed.

Ultrasound image-guided robots are applied in several image-guided intervention procedures in urology. The robot was used in the first clinical trial of the TRUS image-guided Robot Assisted Laparoscopic Prostatectomy, verifying the feasibility of the intraoperative guidance using the robotic ultrasound. The robot was used in in-vitro experiment for TRUS-guided systematic biopsy and demonstrated improved accuracy and repeatability over that performed by human. The robot was also used for the elastography imaging of the prostate. Controlled palpation of the prostate through the robot manipulated probe and other external palpation devices were tested to improve the quality of the elastography image. An algorithm for combining the ordinary B-mode image and its position acquired during the controlled palpation to generate elastography was developed. The algorithm allows the acquisition of an elastography image without access to the RF signal data. A new method of ultrasound to CT image-fusion facilitated by using the TRUS robot as a common reference was developed. This method circumvents the use of image similarity measures, which is difficult to define in cross modality fusion.

Two different MRI-guided robots for prostate biopsy, one by transrectal and the other by transperineal, were developed. A set of experiments to verify the accuracy of the robot in itself and under image-guidance were designed and performed. A set of tests to verify MRI-safety of the robot according to ASTM standard and the interference of the robot with the scanner were designed and performed. After thorough evaluation, the transrectal robot was used in animal study and the transperineal robot is undergoing a clinical trial.

The technological innovations described in this dissertation contribute to the development of the image-guided robot hardware and software, evaluation of its performance and new applications of the robots to the image-guided interventions in urology. Several engineering challenges and required software components for ultrasound image-guided robots are addressed. Components of the work presented in this dissertation have enabled the development and clinical trial of the first FDA cleared robot for the MR environment.

6 Bibliography

ABOLMAESUMI, P., SALCUDEAN, S. E., ZHU, W. H., SIROUSPOUR, M. R. & DIMAIO, S. P. 2002. Image-guided control of a robot for medical ultrasound. *Ieee Transactions on Robotics and Automation,* 18**,** 11-23.

ABOLMAESUMI, P. & SIROUSPOUR, M. R. 2004a. An interacting multiple model probabilistic data association filter for cavity boundary extraction from ultrasound images. *IEEE Trans Med Imaging,* 23**,** 772-784.

ABOLMAESUMI, P. & SIROUSPOUR, M. R. 2004b. Segmentation of prostate contours from ultrasound images. *2004 Ieee International Conference on Acoustics, Speech, and Signal Processing, Vol Iii, Proceedings***,** 517-520.

ADEBAR, T. K., MOHARERI, O. & SALCUDEAN, S. E. 2012. Instrument-Based Calibration and Remote Control of Intraoperative Ultrasound for Robot-Assisted Surgery. *2012 4th Ieee Ras & Embs International Conference on Biomedical Robotics and Biomechatronics (Biorob)***,** 38-43.

BARRY, M. J. 2009. Screening for prostate cancer--the controversy that refuses to die. *N Engl J Med,* 360**,** 1351-4.

BASSAN, H. S., PATEL, R. V. & MOALLEM, M. 2009. A Novel Manipulator for Percutaneous Needle Insertion: Design and Experimentation. *Ieee-Asme Transactions on Mechatronics,* 14**,** 746-761.

BAUMANN, M., MOZER, P., DAANEN, V. & TROCCAZ, J. 2012. Prostate biopsy tracking with deformation estimation. *Medical Image Analysis,* 16**,** 562-76.

BAX, J., COOL, D., GARDI, L., KNIGHT, K., SMITH, D., MONTREUIL, J., SHEREBRIN, S., ROMAGNOLI, C. & FENSTER, A. 2008. Mechanically assisted 3D ultrasound guided prostate biopsy system. *Medical Physics,* 35**,** 5397-5410.

BAX, J., SMITH, D., BARTHA, L., MONTREUIL, J., SHEREBRIN, S., GARDI, L., EDIRISINGHE, C. & FENSTER, A. 2011. A compact mechatronic system for 3D ultrasound guided prostate interventions. *Medical Physics,* 38**,** 1055-1069.

BEYERSDORFF, D., WINKEL, A., HAMM, B., LENK, S., LOENING, S. A. & TAUPITZ, M. 2005. MR imaging-guided prostate biopsy with a closed MR unit at 1.5 T: initial results. *Radiology,* 234**,** 576-81.

BOCTOR, E., VISWANATHAN, A., CHOTI, M., TAYLOR, R. H., FICHTINGER, G. & HAGER, G. 2004. A novel closed form solution for ultrasound calibration. *2004 2nd Ieee International Symposium on Biomedical Imaging: Macro to Nano, Vols 1 and 2***,** 527-530.

BOCTOR, E. M., JAIN, A., CHOTI, M. A., TAYLOR, R. H. & FICHTINGER, G. 2003. A rapid calibration method for registration and 3D tracking of ultrasound images using spatial localizer. *Medical Imaging 2003: Ultrasonic Imaging and Signal Processing,* 5035**,** 521-532.

BOUGUET, J.-Y. 2001. Pyramidal implementation of the affine lucas kanade feature tracker description of the algorithm. *Intel Corporation,* 5.

BRICAULT, I., ZEMITI, N., JOUNIAUX, E., FOUARD, C., TAILLANT, E., DORANDEU, F. & CINQUIN, P. 2008. A light puncture robot for CT and MRI interventions. *Ieee Engineering in Medicine and Biology Magazine,* 27**,** 42-50.

BROWN, R. A. 1979. Stereotactic Head Frame for Use with Ct Body Scanners. *Investigative Radiology,* 14**,** 401-401.

CHINZEI, K., HATA, N., JOLESZ, F. A. & KIKINIS, R. 2000. MR compatible surgical assist robot: System integration and preliminary feasibility study. *Medical Image Computing and Computer-Assisted Intervention - Miccai 2000,* 1935**,** 921-930.

CLEARY, K., MELZER, A., WATSON, V., KRONREIF, G. & STOIANOVICI, D. 2006. Interventional robotic systems: Applications and technology state-of-the art. *Minimally Invasive Therapy & Allied Technologies,* 15**,** 101-113.

COHEN, B. & DINSTEIN, I. 2002. New maximum likelihood motion estimation schemes for noisy ultrasound images. *Pattern Recognition,* 35**,** 455-463.

COOL, D., SHEREBRIN, S., IZAWA, J., CHIN, J. & FENSTER, A. 2008. Design and evaluation of a 3D transrectal ultrasound prostate biopsy system. *Medical Physics,* 35**,** 4695-4707.

COUPE, P., HELLIER, P., AZZABOU, N. & BARILLOT, C. 2005. 3D freehand ultrasound reconstruction based on probe trajectory. *Medical Image Computing and Computer-Assisted Intervention - Miccai 2005, Pt 1,* 3749**,** 597-604.

CZERWINSKI, R. N., JONES, D. L. & O'BRIEN, W. D. 1998. Line and boundary detection in speckle images. *Ieee Transactions on Image Processing,* 7**,** 1700-1714.

CZERWINSKI, R. N., JONES, D. L. & O'BRIEN, W. D. 1999. Detection of lines and boundaries in speckle images - Application to medical ultrasound. *IEEE Trans Med Imaging,* 18**,** 126-136.

D'SOUZA, W. D., MADSEN, E. L., UNAL, O., VIGEN, K. K., FRANK, G. R. & THOMADSEN, B. R. 2001. Tissue mimicking materials for a multi-imaging modality prostate phantom. *Medical Physics,* 28**,** 688-700.

DAVENPOR.PB 1973. Rotations About Nonorthogonal Axes. *Aiaa Journal,* 11**,** 853-857.

DEGOULANGE, E., URBAIN, L., CARON, P., BOUDET, S., GARIEPY, J., MEGNIEN, J. L., PIERROT, F. & DOMBRE, E. 1998. Hippocrate: an intrinsically safe robot for medical applications. *1998 Ieee/Rsj International Conference on Intelligent Robots and Systems - Proceedings, Vols 1-3***,** 959-964.

DIMAIO, S. P., PIEPER, S., CHINZEI, K., HATA, N., HAKER, S. J., KACHER, D. F., FICHTINGER, G., TEMPANY, C. M. & KIKINS, R. 2007. Robot-assisted needle placement in open MRI: System architecture, integration and validation. *Computer Aided Surgery,* 12**,** 15-24.

ELDRIDGE, B., GRUBEN, K., LAROSE, D., FUNDA, J., GOMORY, S., KARIDIS, J., MCVICKER, G., TAYLOR, R. & ANDERSON, J. 1996. A remote center of motion robotic arm for computer assisted surgery. *Robotica,* 14**,** 103-109.

ELHAWARY, H., TSE, Z. T. H., HAMED, A., REA, M., DAVIES, B. L. & LAMPERTH, M. U. 2008. The case for MR-compatible robotics: a review of the state of the. *International Journal of Medical Robotics and Computer Assisted Surgery,* 4**,** 105-113.

ELHAWARY, H., TSE, Z. T. H., REA, M., ZIVANOVIC, A., DAVIES, B. L., BESANT, C., DESOUZA, N. M., MCROBBIE, D., YOUNG, I. & LAMPERTH, M. U. 2010. Robotic System for Transrectal Biopsy of the Prostate Real-Time Guidance Under MRI. *Ieee Engineering in Medicine and Biology Magazine,* 29**,** 78-86.

ENGELHARD, K., HOLLENBACH, H. P., KIEFER, B., WINKEL, A., GOEB, K. & ENGEHAUSEN, D. 2006. Prostate biopsy in the supine position in a standard 1.5-T scanner under real time MR-imaging control using a MR-compatible endorectal biopsy device. *Eur Radiol,* 16**,** 1237-43.

FARNEBÄCK, G. 2003. Two-frame motion estimation based on polynomial expansion. *Image Analysis.* Springer.

FICHTINGER, G., DEWEESE, T. L., PATRICIU, A., TANACS, A., MAZILU, D., ANDERSON, J. H., MASAMUNE, K., TAYLOR, R. H. & STOIANOVICI, D. 2002. System for robotically assisted prostate biopsy and therapy with intraoperative CT guidance. *Academic Radiology,* 9**,** 60-74.

FICHTINGER, G., FIENE, J. P., KENNEDY, C. W., KRONREIF, G., IORDACHITA, I., SONG, D. Y., BURDETTE, E. C. & KAZANZIDES, P. 2008. Robotic assistance for ultrasound-guided prostate brachytherapy. *Medical Image Analysis,* 12**,** 535-545.

FISCHER, G. S., IORDACHITA, I., CSOMA, C., TOKUDA, J., DIMAIO, S. P., TEMPANY, C. M., HATA, N. & FICHTINGER, G. 2008. MRI-compatible pneumatic robot for transperineal prostate needle placement. *Ieee-Asme Transactions on Mechatronics,* 13**,** 295-305.

FOROUGHI, P., RIVAZ, H., FLEMING, I. N., HAGER, G. D. & BOCTOR, E. M. 2010. Tracked Ultrasound Elastography (TrUE). *Medical Image Computing and Computer-Assisted Intervention - Miccai 2010, Pt Ii,,* 6362**,** 9-16.

FRENCH, D., MORRIS, J., KEYES, M., GOKSEL, O. & SALCUDEAN, S. 2005. Computing intraoperative dosimetry for prostate brachytherapy using TRUS and fluoroscopy. *Academic Radiology,* 12**,** 1262-1272.

FUNDA, J., GROSSMAN, D. D., KARIDIS, J. P., LAROSE, D. A. & TAYLOR, R. H. 1995. Remote center-of-motion robot for surgery. Google Patents.

GASSERT, R., BURDET, E. & CHINZEI, K. 2008a. MRI-compatible robotics. *Ieee Engineering in Medicine and Biology Magazine,* 27**,** 12-14.

GASSERT, R., CHAPUIS, D., BLEULER, H. & BURDET, E. 2008b. Sensors for applications in magnetic resonance environments. *Ieee-Asme Transactions on Mechatronics,* 13**,** 335-344.

GASSERT, R., MOSER, R., BURDET, E. & BLEULER, H. 2006. MRI/fMRI-compatible robotic system with force feedback for interaction with human motion. *Ieee-Asme Transactions on Mechatronics,* 11**,** 216-224.

GILL, I. S. & UKIMURA, O. 2007. Thermal energy-free laparoscopic nerve-sparing radical prostatectomy: one-year potency outcomes. *Urology,* 70**,** 309-14.

GOLDBERG, R., DUMITRU, M., TAYLOR, R. & STOIANOVICI, D. 2001. A Modular Robotic System for Ultrasound Image Acquisition. *In:* NIESSEN, W. & VIERGEVER, M. (eds.) *Medical Image Computing and Computer-Assisted Intervention – MICCAI 2001.* Springer Berlin Heidelberg.

GOLDENBERG, A. A., TRACHTENBERG, J., KUCHARCZYK, W., YI, Y., HAIDER, M., MA, L., WEERSINK, R. & RAOUFI, C. 2008. Robotic system for closed-bore MRI-guided prostatic interventions. *Ieee-Asme Transactions on Mechatronics,* 13**,** 374-379.

HAMBROCK, T., FUTTERER, J. J., HUISMAN, H. J., HULSBERGEN-VANDEKAA, C., VAN BASTEN, J. P., VAN OORT, I., WITJES, J. A. & BARENTSZ, J. O. 2008. Thirty-two-channel coil 3T magnetic resonance-guided biopsies of prostate tumor suspicious regions identified on multimodality 3T magnetic resonance imaging: technique and feasibility. *Invest Radiol,* 43**,** 686-94.

HAN, M., CHANG, D., KIM, C., LEE, B. J., ZUO, Y. H., KIM, H. J., PETRISOR, D., TROCK, B., PARTIN, A. W., RODRIGUEZ, R., CARTER, H. B., ALLAF, M., KIM, J. & STOIANOVICI, D. 2012. Geometric Evaluation of Systematic Transrectal Ultrasound Guided Prostate Biopsy. *Journal of Urology,* 188**,** 2404-2409.

HAN, M., KIM, C., MOZER, P., SCHAFER, F., BADAAN, S., VIGARU, B., TSENG, K., PETRISOR, D., TROCK, B. & STOIANOVICI, D. 2011. Tandem-robot Assisted Laparoscopic Radical Prostatectomy to Improve the Neurovascular Bundle Visualization: A Feasibility Study. *Urology,* 77.

HEMPEL, E., FISCHER, H., GUMB, L., HOHN, T., KRAUSE, H., VOGES, U., BREITWIESER, H., GUTMANN, B., DURKE, J., BOCK, M. & MELZER, A. 2003. An MRI-compatible surgical robot for precise radiological interventions. *Comput Aided Surg,* 8**,** 180-91.

HO, H. S. S., MOHAN, P., LIM, E. D., LI, D. L., YUEN, S. P., NG, W. S., LAU, W. K. O. & CHENG, C. W. S. 2009. Robotic ultrasound-guided prostate intervention device: system description and results from phantom studies. *International Journal of Medical Robotics and Computer Assisted Surgery,* 5**,** 51-58.

HRICAK, H., CHOYKE, P. L., EBERHARDT, S. C., LEIBEL, S. A. & SCARDINO, P. T. 2007. Imaging prostate cancer: A multidisciplinary perspective. *Radiology,* 243**,** 28-53.

HSU, P. W., PRAGER, R. W., GEE, A. H. & TREECE, G. M. 2008. Real-time freehand 3D ultrasound calibration. *Ultrasound Med Biol,* 34**,** 239-51.

HUNG, A. J., ABREU, A. L., SHOJI, S., GOH, A. C., BERGER, A. K., DESAI, M. M., ARON, M., GILL, I. S. & UKIMURA, O. 2012. Robotic transrectal ultrasonography during robot-assisted radical prostatectomy. *Eur Urol,* 62**,** 341-8.

HUNGR, N., BAUMANN, M., LONG, J. A. & TROCCAZ, J. 2012. A 3-D Ultrasound Robotic Prostate Brachytherapy System With Prostate Motion Tracking. *Ieee Transactions on Robotics,* 28**,** 1382-1397.

JAIN, A., DEGUET, A., IORDACHITA, I., CHINTALAPANI, G., VIKAL, S., BLEVINS, J., LE, Y., ARMOUR, E., BURDETTE, C., SONG, D. & FICHTINGER, G. 2012. Intra-operative 3D guidance and edema detection in prostate brachytherapy using a non-isocentric C-arm. *Medical Image Analysis,* 16**,** 731-743.

JAIN, A., DEGUET, A., LORDACHITA, I., CHINTALAPANI, G., BLEVINS, J., LE, Y., ARMOUR, E., BURDETTE, C., SONG, D. & FICHTINGER, G. 2007. Intra-operative 3D guidance in prostate brachytherapy using a non-isocentric C-arm. *Medical Image Computing and Computer-Assisted Intervention- MICCAI 2007, Pt 2, Proceedings,* 4792**,** 9-17.

JAIN, A. K., MUSTAFA, T., ZHOU, Y., BURDETTE, C., CHIRIKJIAN, G. S. & FICHTINGER, G. 2005. FTRAC - A robust fluoroscope tracking fiducial. *Medical Physics,* 32**,** 3185-3198.

KALLEL, F. & OPHIR, J. 1997. A least-squares strain estimator for elastography. *Ultrasonic Imaging,* 19**,** 195-208.

KARAMALIS, A., WEIN, W., KUTTER, O. & NAVAB, N. Year. Fast hybrid freehand ultrasound volume reconstruction. *In*, 2009. 726114-726114-8.

KAYE, D. R., STOIANOVICI, D. & HAN, M. 2014. Robotic ultrasound and needle guidance for prostate cancer management: review of the contemporary literature. *Curr Opin Urol,* 24**,** 75-80.

KELLOFF, G. J., CHOYKE, P. & COFFEY, D. S. 2009. Challenges in clinical prostate cancer: role of imaging. *AJR Am J Roentgenol,* 192**,** 1455-70.

KIM, C., CHANG, D., PETRISOR, D., CHIRIKJIAN, G., HAN, M. & STOIANOVICI, D. 2013. Ultrasound Probe and Needle-Guide Calibration for Robotic Ultrasound Scanning and Needle Targeting. *Ieee Transactions on Biomedical Engineering,* 60**,** 1728-1734.

KRIEGER, A., IORDACHITA, I. I., GUION, P., SINGH, A. K., KAUSHAL, A., MENARD, C., PINTO, P. A., CAMPHAUSEN, K., FICHTINGER, G. & WHITCOMB, L. L. 2011. An MRI-Compatible Robotic System With Hybrid Tracking for MRI-Guided Prostate Intervention. *Ieee Transactions on Biomedical Engineering,* 58**,** 3049-3060.

KRIEGER, A., SONG, S. E., CHO, N. B., IORDACHITA, I. I., GUION, P., FICHTINGER, G. & WHITCOMB, L. L. 2013. Development and Evaluation of an Actuated MRI-Compatible Robotic System for MRI-Guided Prostate Intervention. *Ieee-Asme Transactions on Mechatronics,* 18**,** 273-284.

KRIEGER, A., SUSIL, R. C., MENARD, C., COLEMAN, J. A., FICHTINGER, G., ATALAR, E. & WHITCOMB, L. L. 2005. Design of a novel MRI compatible manipulator for image guided prostate interventions. *Ieee Transactions on Biomedical Engineering,* 52**,** 306-313.

KUO, C. H., DAI, J. S. & DASGUPTA, P. 2012. Kinematic design considerations for minimally invasive surgical robots: an overview. *International Journal of Medical Robotics and Computer Assisted Surgery,* 8**,** 127-145.

LERNER, R. M., HUANG, S. R. & PARKER, K. J. 1990. "Sonoelasticity" images derived from ultrasound signals in mechanically vibrated tissues. *Ultrasound Med Biol,* 16**,** 231-9.

LEROY, A., MOZER, P., PAYAN, Y. & TROCCAZ, J. 2004. Rigid registration of freehand 3D ultrasound and CT-scan kidney images. *Medical Image Computing and Computer-Assisted Intervention - Miccai 2004, Pt 1, Proceedings,* 3216**,** 837-844.

MACURA, K. J. & STOIANOVICI, D. 2008. Advancements in magnetic resonance-guided robotic interventions in the prostate. *Top Magn Reson Imaging,* 19**,** 297-304.

MELZER, A., GUTMANN, B., REMMELE, T., WOLF, R., LUKOSCHECK, A., BOCK, M., BARDENHEUER, H. & FISCHER, H. 2008. INNOMOTION for percutaneous image-guided interventions. *Ieee Engineering in Medicine and Biology Magazine,* 27**,** 66-73.

MERCIER, L., LANGO, T., LINDSETH, F. & COLLINS, D. L. 2005. A review of calibration techniques for freehand 3-D ultrasound systems. *Ultrasound Med Biol,* 31**,** 449-71.

MOHARERI, O., RAMEZANI, M., ADEBAR, T. K., ABOLMAESUMI, P. & SALCUDEAN, S. E. 2013. Automatic Localization of the da Vinci Surgical Instrument Tips in 3-D Transrectal Ultrasound. *Ieee Transactions on Biomedical Engineering,* 60**,** 2663-2672.

MOTKOSKI, J. W., YANG, F. W., LWU, S. H. H. & SUTHERLAND, G. R. 2013. Toward Robot-Assisted Neurosurgical Lasers. *Ieee Transactions on Biomedical Engineering,* 60**,** 892-898.

MOZER, P., BAUMANN, M., CHEVREAU, G., MOREAU-GAUDRY, A., BART, S., RENARD-PENNA, R., COMPERAT, E., CONORT, P., BITKER, M. O., CHARTIER-KASTLER, E., RICHARD, F. & TROCCAZ, J. 2009. Mapping of transrectal ultrasonographic prostate biopsies: quality control and learning curve assessment by image processing. *J Ultrasound Med,* 28**,** 455-60.

MURRAY, R. M., LI, Z. & SASTRY, S. S. 1994. *A Mathematical Introduction to Robotic Manipulation*, CRC Press.

NIGHTINGALE, K., SOO, M. S., NIGHTINGALE, R. & TRAHEY, G. 2002. Acoustic radiation force impulse imaging: in vivo demonstration of clinical feasibility. *Ultrasound Med Biol,* 28**,** 227-35.

NOBLE, J. A. & BOUKERROUI, D. 2006. Ultrasound image segmentation: a survey. *IEEE Trans Med Imaging,* 25**,** 987-1010.

OPHIR, J., CESPEDES, I., PONNEKANTI, H., YAZDI, Y. & LI, X. 1991. Elastography: a quantitative method for imaging the elasticity of biological tissues. *Ultrason Imaging,* 13**,** 111-34.

PAN, B., WU, D. F. & WANG, Z. Y. 2012. Internal displacement and strain measurement using digital volume correlation: a least-squares framework. *Measurement Science & Technology,* 23.

PASTICIER, G., RIETBERGEN, J. B., GUILLONNEAU, B., FROMONT, G., MENON, M. & VALLANCIEN, G. 2001. Robotically assisted laparoscopic radical prostatectomy: feasibility study in men. *Eur Urol,* 40**,** 70-4.

PATHAK, S. D., CHALANA, V., HAYNOR, D. R. & KIM, Y. 2000. Edge-guided boundary delineation in prostate ultrasound images. *IEEE Trans Med Imaging,* 19**,** 1211-1219.

PATRICIU, A., PETRISOR, D., MUNTENER, M., MAZILU, D., SCHAR, M. & STOIANOVICI, D. 2007. Automatic brachytherapy seed placement under MRI guidance. *Ieee Transactions on Biomedical Engineering,* 54**,** 1499-1506.

PATRICIU, A., SOLOMON, S., KAVOUSSI, L. & STOIANOVICI, D. 2001. Robotic Kidney and Spine Percutaneous Procedures Using a New Laser-Based CT Registration Method. *In:* NIESSEN, W. & VIERGEVER, M. (eds.) *Medical Image Computing and Computer-Assisted Intervention – MICCAI 2001.* Springer Berlin Heidelberg.

PENNEY, G. P., BLACKALL, J. M., HAMADY, M. S., SABHARWAL, T., ADAM, A. & HAWKES, D. J. 2004. Registration of freehand 3D ultrasound and magnetic resonance liver images. *Medical Image Analysis,* 8**,** 81-91.

PICCIGALLO, M., SCARFOGLIERO, U., QUAGLIA, C., PETRONI, G., VALDASTRI, P., MENCIASSI, A. & DARIO, P. 2010. Design of a Novel Bimanual Robotic System for Single-Port Laparoscopy. *Ieee-Asme Transactions on Mechatronics,* 15**,** 871-878.

PRAGER, R. W., ROHLING, R. N., GEE, A. H. & BERMAN, L. 1998. Rapid calibration for 3-D freehand ultrasound. *Ultrasound Med Biol,* 24**,** 855-69.

PRIESTER, A. M., NATARAJAN, S. & CULJAT, M. O. 2013. Robotic Ultrasound Systems in Medicine. *Ieee Transactions on Ultrasonics Ferroelectrics and Frequency Control,* 60**,** 507-523.

REVELL, J., MIRMEHDI, M. & MCNALLY, D. 2005. Computer vision elastography: Speckle adaptive motion estimation for elastography using ultrasound sequences. *IEEE Transactions on Medical Imaging,* 24**,** 755-766.

ROCHE, A., PENNEC, X., MALANDAIN, G. & AYACHE, N. 2001. Rigid registration of 3-D ultrasound with MR images: A new approach combining intensity and gradient information. *Ieee Transactions on Medical Imaging,* 20**,** 1038-1049.

ROUSSEAU, F., HELLIER, P. & BARILLOT, C. 2005. Confhusius: a robust and fully automatic calibration method for 3D freehand ultrasound. *Med Image Anal,* 9**,** 25-38.

SCHAEFERS, G. 2008. Testing MR safety and compatibility: an overview of the methods and current standards. *IEEE Eng Med Biol Mag,* 27**,** 23-7.

SCHENCK, J. F. 1996. The role of magnetic susceptibility in magnetic resonance imaging: MRI magnetic compatibility of the first and second kinds. *Med Phys,* 23**,** 815-50.

SCHOUTEN, M. G., ANSEMS, J., RENEMA, W. K., BOSBOOM, D., SCHEENEN, T. W. & FUTTERER, J. J. 2010a. The accuracy and safety aspects of a novel robotic needle guide manipulator to perform transrectal prostate biopsies. *Medical Physics,* 37**,** 4744-50.

SCHOUTEN, M. G., ANSEMS, J., RENEMA, W. K., BOSBOOM, D., SCHEENEN, T. W. & FUTTERER, J. J. 2010b. The accuracy and safety aspects of a novel robotic needle guide manipulator to perform transrectal prostate biopsies. *Med Phys,* 37**,** 4744-50.

SIEGEL, R., NAISHADHAM, D. & JEMAL, A. 2013. Cancer statistics, 2013. *CA Cancer J Clin,* 63**,** 11-30.

SKARECKY, D. W. 2013. Robotic-assisted radical prostatectomy after the first decade: surgical evolution or new paradigm. *ISRN Urol,* 2013**,** 157379.

SOLBERG, O. V., LINDSETH, F., TORP, H., BLAKE, R. E. & NAGELHUS HERNES, T. A. 2007. Freehand 3D ultrasound reconstruction algorithms--a review. *Ultrasound Med Biol,* 33**,** 991-1009.

SONG, S. E., CHO, N. B., FISCHER, G., HATA, N., TEMPANY, C., FICHTINGER, G. & IORDACHITA, I. 2010. Development of a Pneumatic Robot for MRI-guided Transperineal Prostate Biopsy and Brachytherapy: New Approaches. *2010 Ieee International Conference on Robotics and Automation (Icra)***,** 2580-2585.

SRIMATHVEERAVALLI, G., KIM, C., PETRISOR, D., EZELL, P., COLEMAN, J., HRICAK, H., SOLOMON, S. B. & STOIANOVICI, D. 2013. MRI-Safe Robot for Targeted Transrectal Prostate Biopsy: Animal Experiments. *BJU Int*.

STEGGERDA, M., SCHNEIDER, C., VAN HERK, M., ZIJP, L., MOONEN, L. & VAN DER POEL, H. 2005. The applicability of simultaneous TRUS-CT imaging for the evaluation of prostate seed implants. *Medical Physics,* 32**,** 2262-2270.

STOIANOVICI, D. 2005. Multi-imager compatible actuation principles in surgical robotics. *International Journal of Medical Robotics and Computer Assisted Surgery,* 1**,** 86-100.

STOIANOVICI, D., KIM, C., SCHAFER, F., HUANG, C. M., ZUO, Y. H., PETRISOR, D. & HAN, M. 2013a. Endocavity Ultrasound Probe Manipulators. *Ieee-Asme Transactions on Mechatronics,* 18**,** 914-921.

STOIANOVICI, D., KIM, C., SRIMATHVEERAVALLI, G., SEBRECHT, P., PETRISOR, D., COLEMAN, J., SOLOMON, S. B. & HRICAK, H. 2013b. MRI-Safe Robot for Endorectal Prostate Biopsy. *Mechatronics, IEEE/ASME Transactions on,* PP**,** 1-11.

STOIANOVICI, D., PATRICIU, A., PETRISOR, D., MAZILU, D. & KAVOUSSI, L. 2007. A new type of motor: Pneumatic step motor. *Ieee-Asme Transactions on Mechatronics,* 12**,** 98-106.

STOIANOVICI, D., WHITCOMB, L. L., MAZILU, D., TAYLOR, R. H. & KAVOUSSI, L. R. 2006. *Remote center of motion robotic system and method*. U.S patent application C03512. Apr. 4.

SU, H., ZERVAS, M., COLE, G. A., FURLONG, C. & FISCHER, G. S. 2011. Real-time MRI-Guided Needle Placement Robot with Integrated Fiber Optic Force Sensing. *2011 Ieee International Conference on Robotics and Automation (Icra)***,** 1583-1588.

SUSIL, R. C., ANDERSON, J. H. & TAYLOR, R. H. 1999. A single image registration method for CT guided interventions. *Medical Image Computing and Computer-Assisted Intervention, Miccai'99, Proceedings,* 1679**,** 798-808.

SUTHERLAND, G. R., LATOUR, I. & GREER, A. D. 2008. Integrating an image-guided robot with intraoperative MRI: a review of the design and construction of neuroArm. *IEEE Eng Med Biol Mag,* 27**,** 59-65.

SUTHERLAND, G. R., MCBETH, P. B. & LOUW, D. F. 2003. NeuroArm: an MR compatible robot for microsurgery. *Cars 2003: Computer Assisted Radiology and Surgery, Proceedings,* 1256**,** 504-508.

TAYLOR, R. H. & STOIANOVICI, D. 2003. Medical robotics in computer-integrated surgery. *Ieee Transactions on Robotics and Automation,* 19**,** 765-781.

TURGAY, E., SALCUDEAN, S. & ROHLING, R. 2006. Identifying the mechanical properties of tissue by ultrasound strain imaging. *Ultrasound in Medicine and Biology,* 32**,** 221-235.

VAN DEN BOSCH, M. R., MOMAN, M. R., VAN VULPEN, M., BATTERMANN, J. J., DUIVEMAN, E., VAN SCHELVEN, L. J., DE LEEUW, H., LAGENDIJK, J. J. & MOERLAND, M. A. 2010. MRI-guided robotic system for transperineal prostate interventions: proof of principle. *Phys Med Biol,* 55**,** N133-40.

VON BERG, J., KRUECKER, J., SCHULZ, H., MEETZ, K. & SABCZYNSKI, J. 2004. A hybrid method for registration of interventional CT and ultrasound images. *Cars 2004: Computer Assisted Radiology and Surgery, Proceedings,* 1268**,** 492-497

1417.

WALSH, P. C., LEPOR, H. & EGGLESTON, J. C. 1983. Radical prostatectomy with preservation of sexual function: anatomical and pathological considerations. *Prostate,* 4**,** 473-85.

WANG, Y. Q., CARDINAL, H. N., DOWNEY, D. B. & FENSTER, A. 2003. Semiautomatic three-dimensional segmentation of the prostate using two-dimensional ultrasound images. *Medical Physics,* 30**,** 887-897.

WEIN, W., PACHE, F., ROPER, B. & NAVAB, N. 2006. Backward-warping ultrasound reconstruction for improving diagnostic value and registration. *Medical Image Computing and Computer-Assisted Intervention - Miccai 2006, Pt 2,* 4191**,** 750-757.

WEIN, W., ROPER, B. & NAVAB, N. 2007. Integrating diagnostic beta-mode ultrasonography into CT-based radiation treatment planning. *Ieee Transactions on Medical Imaging,* 26**,** 866-879.

WEIN, W. G., BRUNKE, S., KHAMENE, A., CALLSTROM, M. R. & NAVAB, N. 2008. Automatic CT-ultrasound registration for diagnostic imaging and image-guided intervention. *Medical Image Analysis,* 12**,** 577-585.

YAKAR, D., SCHOUTEN, M. G., BOSBOOM, D. G., BARENTSZ, J. O., SCHEENEN, T. W. & FUTTERER, J. J. 2011. Feasibility of a pneumatically actuated MR-compatible robot for transrectal prostate biopsy guidance. *Radiology,* 260**,** 241-7.

YU, Y., PODDER, T. K., ZHANG, Y. D., NG, W. S., MISIC, V., SHERMAN, J., FULLER, D., RUBENS, D. J., STRANG, J. G., BRASACCHIO, R. A. & MESSING, E. M. 2007. Robotic system for prostate brachytherapy. *Computer Aided Surgery,* 12**,** 366-375.

ZAKARIA, T., QIN, Z. & MAURICE, R. L. 2010. Optical-Flow-Based B-Mode Elastography: Application in the Hypertensive Rat Carotid. *IEEE Transactions on Medical Imaging,* 29**,** 570-578.

ZEMITI, N., BRICAULT, I., FOUARD, C., SANCHEZ, B. & CINQUIN, P. 2008. LPR: A CT and MR-compatible puncture robot to enhance accuracy and safety of image-guided interventions. *Ieee-Asme Transactions on Mechatronics,* 13**,** 306-315.

A. Appendices

A.1 Solution to Paden-Kahan Subproblem 1

Problem

: Given the unit axis of rotation $\vec{\boldsymbol{\omega}}$ and two unit vector $\vec{\mathbf{x}}$ and $\vec{\mathbf{y}}$, find a rotation angle θ that rotates $\vec{\mathbf{x}}$ to $\vec{\mathbf{y}}$

$$e^{\widehat{\omega}\theta}\vec{\mathbf{x}} = \vec{\mathbf{y}} \tag{A.1}$$

Solution

: Using Rodrigues formula $e^{\widehat{\omega}\theta} = \cos\theta\, I + \sin\theta\, \widehat{\boldsymbol{\omega}} + (1 - \cos\theta)\vec{\boldsymbol{\omega}}\,\vec{\boldsymbol{\omega}}^T$ we have

$$\vec{\mathbf{y}} = \cos\theta\,\vec{\mathbf{x}} + \sin\theta\,(\vec{\boldsymbol{\omega}} \times \vec{\mathbf{x}}) + (1 - \cos\theta)(\vec{\boldsymbol{\omega}} \cdot \vec{\mathbf{x}})\vec{\boldsymbol{\omega}} \tag{A.2}$$

Multiplying both side of the equation A.2 by $\vec{\boldsymbol{\omega}}^{\boldsymbol{T}}$, we have

$$(\vec{\boldsymbol{\omega}} \cdot \vec{\mathbf{y}}) = (\vec{\boldsymbol{\omega}} \cdot \vec{\mathbf{x}}) \tag{A.3}$$

which defines the necessary condition between $\vec{\mathbf{x}}$ and $\vec{\mathbf{y}}$ for the solution to exist.

Multiplying both side of the equation A.2 by $\vec{\mathbf{x}}^{\boldsymbol{T}}$, we have

$$\vec{\mathbf{x}} \cdot \vec{\mathbf{y}} = \cos\theta + (1 - \cos\theta)(\vec{\boldsymbol{\omega}} \cdot \vec{\mathbf{x}})^2 \tag{A.4}$$

leading to solution

$$\cos\theta = \frac{\vec{\mathbf{x}} \cdot \vec{\mathbf{y}} - (\vec{\boldsymbol{\omega}} \cdot \vec{\mathbf{x}})^2}{1 - (\vec{\boldsymbol{\omega}} \cdot \vec{\mathbf{x}})^2} \tag{A.5}$$

A.2 Solution to Paden-Kahan Subproblem 2

Problem

: Let $\overrightarrow{\boldsymbol{\omega}}_{\mathbf{1}}$ and $\overrightarrow{\boldsymbol{\omega}}_{\mathbf{2}}$ be two unit axis of rotation. Find two rotation angles θ_1 and θ_2 that brings unit vector $\vec{\mathbf{x}}$ to $\vec{\mathbf{y}}$ by rotation about $\overrightarrow{\boldsymbol{\omega}}_{\mathbf{2}}$ by θ_2 followed by rotation about $\overrightarrow{\boldsymbol{\omega}}_{\mathbf{1}}$ by θ_1.

$$e^{\widehat{\omega_1}\theta_1}e^{\widehat{\omega_2}\theta_2}\vec{\mathbf{x}} = \vec{\mathbf{y}} \tag{A.6}$$

Solution

: Let's denote the intermediate point of the rotation as $\vec{\boldsymbol{c}}$ which satisfies

$$\vec{\mathbf{c}} = e^{\widehat{\omega_2}\theta_2}\vec{\mathbf{x}} = e^{-\widehat{\omega_1}\theta_1}\vec{\mathbf{y}} \tag{A.7}$$

This is two Paden-Kahan subproblem 1 involving unknown vector $\vec{\mathbf{c}}$**.** From the necessary condition in A.2

$$\overrightarrow{\boldsymbol{\omega}}_{\mathbf{2}} \cdot \vec{\mathbf{c}} = \overrightarrow{\boldsymbol{\omega}}_{\mathbf{2}} \cdot \vec{\mathbf{x}} \ \text{ and } \ \overrightarrow{\boldsymbol{\omega}}_{\mathbf{1}} \cdot \vec{\mathbf{c}} = \overrightarrow{\boldsymbol{\omega}}_{\mathbf{1}} \cdot \vec{\mathbf{y}} \tag{A.8}$$

Since $\overrightarrow{\boldsymbol{\omega}_{\mathbf{1}}}$, $\overrightarrow{\boldsymbol{\omega}_{\mathbf{2}}}$ and $\overrightarrow{\boldsymbol{\omega}_{\mathbf{1}}} \times \overrightarrow{\boldsymbol{\omega}_{\mathbf{2}}}$ forms independent basis, $\vec{\mathbf{c}}$ can be expressed as

$$\vec{\mathbf{c}} = \alpha\overrightarrow{\boldsymbol{\omega}}_{\mathbf{1}} + \beta\overrightarrow{\boldsymbol{\omega}}_{\mathbf{2}} + \gamma(\overrightarrow{\boldsymbol{\omega}}_{\mathbf{1}} \times \overrightarrow{\boldsymbol{\omega}}_{\mathbf{2}}) \tag{A.9}$$

Using equation A.8 and 9, we can solve

$$\overrightarrow{\boldsymbol{\omega}}_{\mathbf{1}} \cdot \vec{\mathbf{c}} = \alpha + \beta(\overrightarrow{\boldsymbol{\omega}}_{\mathbf{1}} \cdot \overrightarrow{\boldsymbol{\omega}}_{\mathbf{2}}) = \overrightarrow{\boldsymbol{\omega}}_{\mathbf{1}} \cdot \vec{\mathbf{y}} \tag{A.10}$$

$$\overrightarrow{\boldsymbol{\omega}}_{\mathbf{2}} \cdot \vec{\mathbf{c}} = \alpha(\overrightarrow{\boldsymbol{\omega}}_{\mathbf{1}} \cdot \overrightarrow{\boldsymbol{\omega}}_{\mathbf{2}}) + \beta = \overrightarrow{\boldsymbol{\omega}}_{\mathbf{2}} \cdot \vec{\mathbf{x}} \tag{A.11}$$

This determines α, β

$$\alpha = \frac{(\overrightarrow{\boldsymbol{\omega}}_{\mathbf{1}} \cdot \overrightarrow{\boldsymbol{\omega}}_{\mathbf{2}})(\overrightarrow{\boldsymbol{\omega}}_{\mathbf{1}} \cdot \vec{\mathbf{x}}) - (\overrightarrow{\boldsymbol{\omega}}_{\mathbf{2}} \cdot \vec{\mathbf{y}})}{(\overrightarrow{\boldsymbol{\omega}}_{\mathbf{1}} \cdot \overrightarrow{\boldsymbol{\omega}}_{\mathbf{2}})^2 - 1} \tag{A.12}$$

$$\beta = \frac{(\vec{\boldsymbol{\omega}}_1 \cdot \vec{\boldsymbol{\omega}}_2)(\vec{\boldsymbol{\omega}}_1 \cdot \vec{\mathbf{y}}) - (\vec{\boldsymbol{\omega}}_2 \cdot \vec{\mathbf{x}})}{(\vec{\boldsymbol{\omega}}_1 \cdot \vec{\boldsymbol{\omega}}_2)^2 - 1} \tag{A.13}$$

Since the rotation cannot change the magnitude of the vector and $\vec{\mathbf{x}}$, $\vec{\mathbf{y}}$ are unit vectors

$$|\vec{\mathbf{x}}|^2 = |\vec{\mathbf{c}}|^2 = \alpha^2 + \beta^2 + \gamma^2 |\vec{\boldsymbol{\omega}}_1 \times \vec{\boldsymbol{\omega}}_2|^2 + 2\alpha\beta(\vec{\boldsymbol{\omega}}_1 \cdot \vec{\boldsymbol{\omega}}_2) = 1 \tag{A.14}$$

leading to

$$\gamma^2 = \frac{1 - \alpha^2 - \beta^2 - 2\alpha\beta(\vec{\boldsymbol{\omega}}_1 \cdot \vec{\boldsymbol{\omega}}_2)}{|\vec{\boldsymbol{\omega}}_1 \times \vec{\boldsymbol{\omega}}_2|^2} \tag{A.15}$$

With α, β and γ known, $\vec{\mathbf{c}}$ can be calculated and two subproblem 1 in A.7 can be solved for θ_1 and θ_2.

Curriculum Vita

NAME	DATE OF BIRTH
Chunwoo Kim	May 04. 1982, South Korea

EDUCATION/TRAINING

INSTITUTION AND LOCATION	DEGREE	YEAR(s)	FIELD OF STUDY
Seoul National University, South Korea	B.S.	2008	Mechanical Engineering Physics minor
Johns Hopkins University, U.S.A	M.S.E	2010	Mechanical Engineering

Positions and Employment

2001 - 2003	Undergraduate Student, Mechanical Aerospace Engineering Department, Seoul National University, Seoul, Korea
2004 - 2006	Technical Staff, Park Systems Inc. (Atomic Force Microscope manufacturing company), Suwon, Korea
2007 - 2008	Undergraduate researcher, Biorobotics Lab (Prof. Jung Kim), Korean Advanced Institute of Science and Technology
2008 - present	Ph.D. student, Urology Robotics Lab (Prof. Dan Stoianovici) , Urology / Mechanical Engineering, Johns Hopkins University, Baltimore, MD

Honors

2008	Fulbright Graduate Study Award (USD 25,000), Foreign Fulbright Student Program, Institute of International Education
2009	Fulbright Graduate Study Award (USD 25,000), Foreign Fulbright Student Program, Institute of International Education
2011	George M.L. Sommerman Engineering Graduate Teaching Assistant Award, Whiting School of Engineering, Johns Hopkins University
2011	Prostate Cancer Training Award (USD 99,816), Prostate Cancer Research Program, Department of Defense Congressionally Directed Medical Research Programs

Selected Conference Papers

1. Han M, **Kim C**, Mozer P, Badaan S, Vigaru B, Schaefer F, Petrisor D, Trock B, Stoianovici D: Tandem Robot Assisted Laparoscopic Radical Prostatectomy: Clinical Feasibility Study for Neurovascular Bundle Visualization. Engineering and Urology Society, 24th Annual Meeting. 2009; pp. 25, **BEST PAPER AWARD**.
2. Huang CM, **Kim C**, Petrisor D, Lee D, Han M, Stoianovici D: Partial Volume Artifact on Prostate Ultrasound Imaging. Engineering and Urology Society, 25th Annual Meeting. 2010; pp. 32, **Outstanding Paper Award**.

3. Stoianovici D, Petrisor D, Chunwoo K, Coleman J, Solomon S, Hricak H: MRI Guided Prostate Biopsy Robot Development. Engineering and Urology Society, 25th Annual Meeting. 2010; pp. 39, **Outstanding Paper Award**.
4. **Kim C**, Schafer F, Chang DY, Petrisor D, Han M, Stoianovici D: Robot for Ultrasound-Guided Prostate Imaging and Intervention. 2011 Ieee/Rsj International Conference on Intelligent Robots and Systems. 2011; pp.943-948.
6. **Kim C**, Srimathveeravalli G, Sebrecht P, Petrisor D, Ezell P, Coleman J, Solomon S, Hricak H, Stoianovici D: Robot-Assisted Direct MRI-Targeted Transrectal Prostate Biopsy. Engineering and Urology Society, 27th Annual Meeting. 2012; pp. 50. **Outstanding Paper Award**.

Journal Papers

1. Han M, **Kim C**, Mozer P, Schafer F, Badaan S, Vigaru B, Tseng K, Petrisor D, Trock B, Stoianovici D: Tandem-robot Assisted Laparoscopic Radical Prostatectomy to Improve the Neurovascular Bundle Visualization: A Feasibility Study. Urology. Feb 2011; Vol.77(2) pp.502-506.
2. Badaan S, Petrisor D, **Kim C**, Mozer P, Mazilu D, Gruionu L, Patriciu A, Cleary K, Stoianovici D: Does needle rotation improve lesion targeting? Int J Med Robot. Jun 2011; Vol.7(2) pp.138-147.
3. Han M, Chang D, **Kim C**, Lee BJ, Zuo Y, Kim HJ, Petrisor D, Trock B, Partin AW, Rodriguez R, Carter HB, Allaf M, Kim J, Stoianovici D: Geometric evaluation of systematic transrectal ultrasound guided prostate biopsy. J Urol. Dec 2012; Vol.188(6) pp.2404-2409.
4. Han M, **Kim C**, Chen H, Kim H-J, Petrisor D, Stoianovici D: Intraoperative ultrasound-based navigation assessment and neurovascular bundles localization in robot-assisted laparoscopic prostatectomy. Urology. Aug 2012; pp. submitted.
5. **Kim C**, Chang D, Petrisor D, Chirikjian G, Han M, Stoianovici D: Ultrasound probe and needle-guide calibration for robotic ultrasound scanning and needle targeting. IEEE Transactions on Biomedical Engineering. Jun 2013; Vol.60(6) pp.1728-1734.
6. Stoianovici D, **Kim C**, Schäfer F, Huang C-M, Zuo Y, Petrisor D, Han M: Endocavity Ultrasound Probe Manipulators. IEEE/ASME TRANSACTIONS ON MECHATRONICS. June 2013; Vol.18(3) pp.914-921.
7. Stoianovici D, **Kim C**, Srimathveeravalli G, Sebrecht P, Petrisor D, Coleman J, Solomon SB, Hricak H: MRI-Safe Robot for Endorectal Prostate Biopsy. Mechatronics, IEEE/ASME Transactions on. 2013; Vol.PP(99) pp.1-11.
8. Srimathveeravalli G, **Kim C**, Petrisor D, Ezell P, Coleman J, Hricak H, Solomon SB, Stoianovici D: MRI-Safe Robot for Targeted Transrectal Prostate Biopsy: Animal Experiments. BJU Int. Oct 10 2013.

Patents

1. Stoianovici D, Han M, Petrisor D, **Kim C**: Cohesive Robot-Ultrasound Probe for Prostate Biopsy. USA Patent ROI (C11934) March 5, 2012.
2. Stoianovici D, Petrisor D, **Kim C**, Sebrecht P: MRI-Safe Robot for Transrectal Prostate Biopsy. USA Patent ROI (C12100), 2012.
3. Stoianovici D, Petrisor D, Schäfer F, **Kim C**, Han M: Remote Center of Motion Robot for Medical Image Scanning and Image-Guided Targeting. USA Patent Application PCT/US2011/060362 (C11305) May 18, 2012.